RICE UNIVERSITY

Topological metals driven by strong correlations in heavy fermion systems

By

Sarah Elaine Grefe

A THESIS SUBMITTED
IN PARTIAL FULFILLMENT OF THE
REQUIREMENTS FOR THE DEGREE

Doctor of Philosophy

APPROVED, THESIS COMMITTEE

Qimiao Si
Qimiao Si (Aug 9, 2020 14:36 CDT)

Qimiao Si

Harry C. and Olga K. Weiss Professor of
Physics & Astronomy

Matthew S. Foster
Matthew S. Foster (Aug 9, 2020 21:52 CDT)

Matthew Foster

Associate Professor of Physics and
Astronomy

Gustavo Scuseria
Gustavo Scuseria (Aug 9, 2020 14:33 CDT)

Gustavo Scuseria

Robert A. Welch Professor of Chemistry,
Professor of Physics & Astronomy and
Materials Science & NanoEngineering

HOUSTON, TEXAS

August 2020

RICE UNIVERSITY

Topological metals driven by strong correlations in heavy fermion systems

by

Sarah E. Grefe

A Thesis Submitted
in Partial Fulfillment of the
Requirements for the Degree

Doctor of Philosophy

Approved, Thesis Committee:

Qimiao Si, *Chair*
Harry C. and Olga K. Weiss Professor of
Physics & Astronomy

Matthew Foster
Associate Professor of Physics and
Astronomy

Gustavo Scuseria
Robert A. Welch Professor of Chemistry,
Professor of Physics & Astronomy and
Materials Science & NanoEngineering

Houston, Texas

August, 2020

ABSTRACT

Topological metals driven by strong correlations in heavy fermion systems

by

Sarah E. Grefe

Heavy fermion metals are intermetallic systems of certain rare-earth or actinide elements, whose partially-filled f electrons interact with each other strongly and form localized magnetic moments. The latter are coupled to weakly correlated conduction electrons by their spin, a process known as the Kondo coupling. These strongly correlated systems can be readily tuned nonthermally to produce quantum phase transitions, and often exotic phases emerge in the vicinity of quantum critical points (QCPs). An outstanding question is what happens when the strong correlations interplay with a large spin-orbit coupling.

In parallel, topological metals are a fascinating class of states, in which topologically protected and dissipationless transport makes them attractive for new electronic devices. In theoretical models of non-interacting electrons, such phases are favored by certain types of couplings, as well as by the particular set of symmetries for the geometric space that electrons move through (i.e. space group of a crystal lattice). Along with efforts to understand the required conditions for a topological phase, there has been an extensive search for weakly correlated materials platforms. What happens to topological metals in strongly correlated settings remains an outstanding open problem.

In this thesis, the heavy fermion systems are proposed to explore topological metal-

lic phases driven by strong correlations. I theoretically demonstrated the existence of topological metallic phases by studying several types of Kondo lattice models. Importantly, the large Coulomb energy scale in these systems has several consequences for how topological metals behave.

In the first part of this thesis, I study the change in anomalous Hall conductivity (AHC) across a QCP in frustrated Kondo lattices. The frustration in the interactions between magnetic moments leads to time-reversal symmetry breaking (TRSB) chiral spin liquid phases, creating a highly singular Berry curvature field that influences the conduction electrons and their transport through the Kondo coupling. The QCP divides the Kondo screened phase with a large Fermi surface, from the Kondo destruction phase with a generically reconstructed Fermi surface. By studying this scenario on both the square lattice and kagomé lattice, I discovered that if the magnetic unit cell has an odd number of sites, the Fermi surface undergoes radical reconstruction in volume, resulting in a sharp jump of the AHC. The implications for the metallic pyrochlore heavy fermion iridate $Pr_2Ir_2O_7$ are explored.

The second part of this thesis advances a correlation-driven topological metal, the Weyl-Kondo semimetal (WKSM). My theoretical work proceeded contemporaneously with experiments in a heavy fermion metal $Ce_3Bi_4Pd_3$. I focused on a three-dimensional nonsymmorphic and noncentrosymmetric Kondo lattice. I show that the ground state is topologically trivial in the absence of the Kondo coupling, but is driven to be a topologically nontrivial Weyl semimetal by the Kondo effect. In the ensuing WKSM phase, a new "Kondo-pinning" effect fixes the Weyl nodes to the Fermi energy. Several distinguishing strong correlation effects are also shown for the WKSM. I then study the topological phases produced when a TRSB Zeeman field is introduced. The Weyl-Kondo nodes move and annihilate, leading to multiple phases. I study and discuss the relevance of my theoretical findings to $Ce_3Bi_4Pd_3$, and propose experimental signatures which take advantage of the Kondo pinning mechanism.

Contents

Chapter 1

Introduction

1.1 Heavy fermion systems

The strongly correlated systems classified as heavy fermion materials have several salient, unique characteristics due to the hallmark presence of rare earth or actinide elements. These elements have partially filled f orbitals, with a Coulomb repulsion between them so large that they form local magnetic moments (acting as a lattice of magnetic impurities), and have narrow atomic-like energy bands. There are also other orbitals or elements that provide free carriers (*i.e.* itinerant or conduction electrons), with dispersive energy bands.

Despite only these simple constituents, the behavior observed in experiments and theoretical models can give rise to a variety of exotic strongly correlated phases, due to two important interactions in heavy fermion metals. First, the local moment electrons and the itinerant electrons interact through their spin degree of freedom, called the *Kondo coupling*. The *Kondo effect* is produced by the quantum fluctuations of conduction electrons and f electron levels near the Fermi surface tunneling back and forth between degenerate spin states. The strength of the Kondo coupling (J_K) increases the probability for the two electron species to form a Kondo singlet state, $|\uparrow\downarrow\rangle = \frac{1}{2}(|\uparrow\rangle_f|\downarrow\rangle_c - |\downarrow\rangle_f|\uparrow\rangle_c)$. Second, there is an effective magnetic interaction between localized moments that is mediated by the free electrons, called the Ruderman-Kittel-Kasuya-Yosida (RKKY) interaction, where the coupling magnitude is denoted I. In the vast majority of heavy fermion materials, the RKKY interaction is energetically favorable toward antiferromagnetism (rather than ferromagnetism).

Although there are clearly several physical mechanisms to consider in heavy fermion

systems, the *relevant* physical mechanisms that this thesis considers occur under the Kondo temperature (T_K) in the strongly correlated regime, leaving the the RKKY and Kondo interactions to explore.

Consider the phases of a generic heavy fermion system near $T = 0$, as the ratio $\delta = \frac{J_K}{I}$ is tuned (Fig. 1.1). When δ is large, the Kondo effect dominates the magnetic ordering. This causes the lattice of local moments to both remain magnetically disordered, and to pair up with free electrons in Kondo singlets. A characteristic tunneling rate τ sets the Kondo temperature T_K by finding the T for which $\frac{\hbar}{\tau} \sim k_B T$. At high temperature or field $T \gg T_K$, the moment scatters more strongly due to the unscreened magnetic moment spin inducing spin-flip scattering. Equivalently, $k_B T_K$ also sets the energy scale below which a Kondo resonance forms, and the system can be described as a Landau Fermi liquid [1, 2, 3, 4]. The f fermions and the free electrons thus hybridize and form coherent, long-lived quasiparticles near the Fermi surface, effectively adding the f electrons to the Luttinger count, changing the enclosed volume of the Fermi surface. The quasiparticles have partially itinerant character, to act as current carriers, and partially localized behavior, to *renormalize* the effective carrier mass to 10^2 to 10^3 times the bare electron mass. This is the namesake 'heavy Fermi liquid' phase, the prototypical phase of heavy fermion materials. Heavy fermion metals act like a 'bad metal', captured mostly with Landau Fermi liquid theory, with normal metal properties yet drastically renormalized parameters (details in Sec. 1.1.2).

When δ is small, the antiferromagnetic coupling is stronger than the Kondo coupling, so the itinerant electrons are freed from the localized ones, while the moments form an ordered antiferromagnetic phase (left side of Fig. 1.1): a magnetic metal. The non-Fermi liquid phase of conventional heavy fermion metals of Fig. 1.1 will be discussed in Sec. 1.1.1.

Quantum phase transitions can be accessed in heavy fermion systems if one tunes parameters that I, J_K are dependent on. Since the magnitude of RKKY interactions

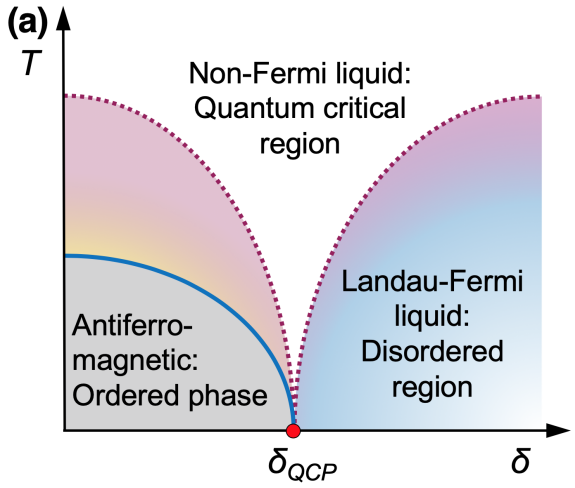

Figure 1.1 : Quantum phase diagram of heavy fermion metals. Labels of phases are written as (top) heavy fermion phase: (bottom) generic quantum phase diagram. The vertical axis tunes temperature T and thus the amount of thermal fluctuations. The horizontal axis tunes a non-thermal control parameter δ, which corresponds to the ratio of the Kondo to RKKY interactions. The red point labeled $\delta_{\rm QCP}$ marks a quantum critical point where the ordered antiferromagnetic phase and the disordered heavy Landau-Fermi liquid phases meet at $T = 0$, producing the quantum critical non-Fermi liquid regime at nonzero temperatures.

versus Kondo coupling can depend on the lattice spacing or the density of magnetic impurities, one can vary non-thermal control parameters such as pressure, doping, and magnetic field [5, 3]. A quantum critical point has been implicated in several heavy fermion metals [5, 3].

1.1.1 Quantum criticality and non-Fermi liquid phases

Quantum critical points are nonanalytic points in the ground state energy of a system as a function of control parameters, and indicate where the energy of the ground state approaches a level crossing with an excited state [6]. The non-thermal control parameter chosen essentially increases or decreases the amount of quantum fluctuations in the system, which can induce changes in order. At $T = 0$, δ passes through a quantum critical point (QCP) that separates two ground states, where $\delta_c = 1$ denotes the ratio

where neither state is dominant. Put another way, the phase transition at δ_c for some $(T > 0)$ has been suppressed to $T = 0$. Generically, the quantum critical state is in a many-body superposition of ordered and disordered states, that is, the order parameter fluctuations span the entire material. The quantum critical state is dominated by quantum fluctuations between phases that compete, leading to behavior that is impossible to classify as either phase. One example of a quantum critical phase is the one-dimensional Luttinger liquid, which shows some Fermi liquid type behavior with respect to DC conductivity, linear-in-T specific heat, finite spin susceptibility, etc. However, there are power-law type singularities in the momentum distribution function and density of states that distinguish it from a Fermi liquid, not to mention the separation of spin dynamics from charge dynamics [7].

Non-Fermi liquids are defined by what they are not, that is, they have behavior that fundamentally deviates from both the heavy Landau Fermi liquid phase and the metallic antiferromagnetic ordered phase. For example, the resistivity of a Fermi liquid has a predominantly T^2 behavior, but this exponent might be $2 + \varepsilon$ in the quantum critical region. The non-Fermi liquid phase occupies a fan-shaped region of the $T > 0$ phase diagram that originates from the $T = 0$ QCP, and the quantum fluctuations driving this phase's properties arise from the QCP. For heavy fermion compounds that do not need much tuning for the antiferromagnetic critical point at $T = 0$, there are a few common properties, such as a specific heat near the QCP that diverges as $\frac{C_v}{T} \sim \log \frac{T_0}{T}$, quasilinear resistivity $\rho \sim T^{1+\varepsilon}$, and spin susceptibility that deviates from the Curie type as $\chi \sim 1/(\chi_0 + cT^a)$ where $a < 1$ [8]. This behavior should be contrasted with that of the more conventional heavy Fermi liquid.

1.1.2 Heavy Fermi liquid signatures

A theoretical conjecture [9, 10, 11] predicted that in the strong coupling limit, that the Kondo coupling is an attractive fixed point, which was later confirmed by numerical renormalization group [12]. Wilson recognized that this meant a ground state made

of Kondo singlets (such as the heavy fermion metal phase) matched the universality class of the Landau Fermi liquid. Landau's Fermi liquid theory recognized that states far from the Fermi surface can be projected out, if one took into account the effect of their interactions. This led to the postulated quasiparticles, which are low-lying states very close to the Fermi surface which act like an ideal (noninteracting) electron gas through the effective interactions. This relied on the notion that the states of the noninteracting theory can be adiabatically connected to that of the interacting one, provided the interactions do not break symmetry or undergo a phase transition. In this system, the Kondo screening manifests Kondo resonances, which then hybridize with conduction electrons, forming the quasiparticle Landau Fermi liquid [13, 14, 1, 3, 2]. Corresponding quasiparticle peaks in the single-electron spectral function have been observed in heavy fermion materials [1, 2].

The Fermi liquid picture is internally consistent, and provides a conceptual basis in which to understand heavy fermion systems [15, 7]. Inside the Fermi liquid regime, the properties of the metal have the same qualitative form as an electron gas, but in terms of the quasiparticle density of states and Landau parameters [14] *.

An illustrative example within the Fermi liquid regime is this simple version of the Kondo lattice model:

$$H = \sum_{\boldsymbol{k}\sigma} \varepsilon_{\boldsymbol{k}} c^{\dagger}_{\boldsymbol{k}\sigma} c_{\boldsymbol{k}\sigma} + J_K \sum_i \boldsymbol{S}_i \cdot \boldsymbol{s}_i \tag{1.1}$$

$$= H_0 + H_1, \tag{1.2}$$

where a local moment spin $\boldsymbol{S}_i = \frac{1}{2}\sum_{\alpha\beta} f^{\dagger}_{i\alpha}\sigma_{\alpha\beta} f_{i\beta}$, couples to a conduction electron spin $\mathbf{s}_i = \frac{1}{2}\sum_{\alpha\beta} c^{\dagger}_{i\alpha}\boldsymbol{\sigma}_{\alpha\beta} c_{i\beta}$; the Pauli matrix vector is $\boldsymbol{\sigma} = \hat{1}\sigma^1 + \hat{2}\sigma^2 + \hat{3}\sigma^3$. H_0

*This behavior in the Kondo lattice depends mainly on two low-energy scale conditions. (1) The temperature fluctuations must be small enough for the local moment spins to be adequately screened, which is to say, $k_B T < k_B T_K$. (2) Any magnetic ordering affecting the local moments' ability to form Kondo singlets must be adequately small, so we neglect moment-moment exchange coupling for now [3].

alone describes a noninteracting Fermi gas, with $\epsilon_{\boldsymbol{k}} = \frac{k^2}{2m_e}$, fixed particle number and elementary particle-hole excitations. The quasiparticle lifetime is defined close to the Fermi surface as $\tau \sim (\varepsilon - \varepsilon_F)^{-2}$, and clearly becomes infinite at the Fermi surface, and is thus long-lived.

Several measurable quantities are then renormalized in terms of the quasiparticle parameters. For instance, the specific heat is

$$C(T) = \gamma T = \frac{2\pi^2 N(\varepsilon_F) k_B^2}{3} T \to m^* \frac{k_F k_B^2}{3} T,$$

essentially linear in temperature, with a finite density of states at the Fermi energy $N(\varepsilon_F)$, and an enhancement coefficient $\gamma \propto m^*$. The effective mass is enhanced as

$$\frac{m^*}{m_e} = 1 + \frac{F_1^s}{3} \tag{1.3}$$

where $F_i^{a,s}$ are antisymmetric/symmetric phenomenological Laundau parameters. The ratio of $\frac{m*}{m}$ also indicates how strongly interacting the fermions of the system are, and with quasiparticle masses in heavy fermion metals up to orders of magnitude greater than the bare masses, they are safely said to be strongly correlated systems [1, 15, 7]. The magnetic susceptibility is similarly enhanced by the effective mass, but is independent of temperature:

$$\chi = 2N(\epsilon_F)\mu_B^2 \to \frac{1}{1 + F_0^a} \frac{\mu_B^2 k_F m^*}{\pi^2}.$$

Anomalous Hall effect

The anomalous Hall effect (AHE) is a transverse current that arises in response to a voltage (electric field) being applied to a system with broken time reversal symmetry. In the normal Hall effect (NHE), a magnetic field is applied perpendicular to the electric field, and the Lorentz force produces the transverse current. It is then not surprising that AHE is observed mainly in ferromagnetic materials, but also in paramagnetic materials in a magnetic field, and in exotic paramagnetic states that can create tiny, effective magnetic fields.

It turns out that Hall effect measurements provide valuable results in low temperatures and high field strengths relevant to heavy fermion materials, which may be inaccessible to other methods. The Hall coefficient is expressed as $R_H = -1/(nec)$, where e, c are the electron charge and speed of light, and n is the electron density. Since the density ultimately determines the occupation of electrons per site per spin (i.e. the filling factor), R_H can be used to infer information about the evolution of the Fermi surface. For instance, in experiments on $YbRh_2Si_2$, experimentalists analyzed the Hall coefficient across a QCP and found a jump in R_H that is interpreted as reconstruction of the Fermi surface [16, 17]. The measured Hall signal contains contributions from all the symmetry-allowed Hall effects in the material, though in standard heavy fermion systems, the normal Hall effect (NHE) tends to dominate, while the AHE is usually very small at low temperatures [18]. However, the AHE can be separated out and can yield valuable information about the system, depending on which mechanism is producing the AHE. In heavy fermion systems, the mechanisms are resonant skew scattering [19, 20], and the intrinsic mechanism [21].

Resonant skew scattering is an extrinsic, disorder-driven process by which the free electron carriers asymmetrically scatter off virtual bound states of the localized magnetic moments. Typically, above the coherence temperature $T > T_{\text{coh}}$, the local moments fluctuate strongly, scattering more carriers and producing a larger resistivity as T_{coh} is approached. Under the coherence temperature $T < T_{\text{coh}}$, the f electrons become constituents of coherent band formation, reducing the scattering dramatically [18]. This forms a broad peak centered around the coherence temperature. As the Fermi liquid is fully formed at lower temperature, the Hall coefficient $R_H(T)$ decreases to a background normal Hall coefficient R_0 at $T = 0$. The skew-scattered AHE has a strong temperature dependence in heavy fermion systems. This is because the skew-scattering AHE conductivity is first order in the Bloch state transport lifetime τ, which is in turn influenced by thermal processes at finite temperature [22].

The intrinsic, Berry phase contribution to the AHE is the predominant quantity

of interest in Ch. 2, because probing this quantity yields information about the systems' topological properties [23, 24]. The Berry curvature is an intrinsic property of the Fermi surface [25], but is usually cast in terms of bulk interband terms that only depend on the Bloch band structure, and so are more amenable to calculation. Deferring discussion of the Berry curvature and topology concepts until Sec. 1.2.1, a finite intrinsic AHE conductivity σ_{xy}^{AH} physically manifests from nontrivial topology in time-reversal symmetry broken systems. In heavy fermion systems, the spontaneous magnetization in ferromagnetically ordered local moments could drive the AHE, but antiferromagnetism is far more common. However, much more of the heavy fermion quantum phase diagram is paramagnetic or disordered. In this case, the magnetization is replaced by an effective magnetic flux localized around plaquettes of the unit cell. This phenomena occurs in frustrated spin systems, in the presence of non collinear spin textures or quantum spin liquid states, or can arise from spin orbit interaction or orbital magnetic effects [22]. In Ch. 2, frustrated Kondo lattices in 2D are shown to produce a finite AHE that can jump dramatically at a Kondo destruction QCP, or smoothly crossover, depending on the lattice (plaquette geometry).

1.1.3 Models

Periodic Anderson model

The periodic Anderson model (PAM) treats the constituents of the heavy fermion system as fermionic degrees of freedom (rather than spin degrees of freedom). It is a theory of how moments form, using two ideas: first, that a strong Coulomb repulsion could block electron transport (as in Mott insulators) and second, that one could reinterpret the virtual bound state resonances resulting from the magnetic ion's electron interactions as a tunneling process between delocalized and localized species.

The PAM Hamiltonian is

$$\mathcal{H} = \mathcal{H}_c + \mathcal{H}_{cd} + \mathcal{H}_d, \tag{1.4}$$

where the conduction electrons are typically a simple nearest-neighbor hopping

$$\mathcal{H}_c = t \sum_{\langle ij \rangle, \sigma} \left(c^\dagger_{i\sigma} c_{j\sigma} + \text{H.c.} \right) - \mu \sum_{i,\sigma} n^c_{i\sigma}, \tag{1.5}$$

but is not limited to nearest-neighbor hopping terms; similarly, there is the hybridization,

$$\mathcal{H}_{cd} = V \sum_{i,\sigma} \left(d^\dagger_{i\sigma} c_{i\sigma} + \text{H.c.} \right), \tag{1.6}$$

and the atomic-like localized energy levels with Coulomb repulsion,

$$\mathcal{H}_d = E_d \sum_{i,\sigma} d^\dagger_{i\sigma} d_{i\sigma} + U \sum_i n^d_{i\uparrow} n^d_{i\downarrow}, \tag{1.7}$$

where the operator d represents the physical $4f$ fermions.

To illustrate the physics and a typical means of solving the model, consider the strongly correlated mixed-valence regime. Here, coherent quantum charge fluctuations occur between a restricted set of valence configurations, *i.e.* $\text{Ce}^{3+}(4f^1) \leftrightarrow \text{Ce}^{4+}(4f^0)$, or infinite-$U$ Anderson model $f^0 + e^- \leftrightarrow f^1$. In both cases, one can view the intermediate state as a bosonic exchange, in preparation for the auxiliary boson treatment. At each site, transform $d^\dagger_{j\sigma} = f^\dagger_{j\sigma} b_j$. By introducing the conserved charge Q, the auxiliary bosons b_j keep track of the deviations of the valence electrons from their maximum charge density, $n_f + n_b = Q$. A simplification can be made by mean field approximation, where the boson is averaged over the unit cell $\langle b_j \rangle \to r$, and the consequence follows that the Kondo resonance width narrows around the Fermi energy $b_j V \to \tilde{V} = rV$, $r < 1$. The charge Q constraint also renormalizes the localized f electron level by including a Lagrange multiplier term as well: $E_f \to \tilde{E}_f = E_f + \ell$.

The free parameters that keep track of the valence fluctuations and chemical potential are determined by solving the set of saddle point equations $\langle \frac{\delta \mathcal{H}}{\delta r} \rangle = 0$, $\langle \frac{\delta \mathcal{H}}{\delta \ell} \rangle = 0$ in terms of the free parameters, r, ℓ. At the saddle point, the physical f-electrons neatly split into a one-body Hamiltonian of quasiparticles representing the coherent part of the wavefunction, and the incoherent part is represented by r^2 [1].

Luckily for the work that is needed in Chapters 3-5, this system of equations can be solved by numerical methods (See Appendix B6).

Kondo lattice model

Heavy fermion systems with stoichiometrically integral values of f electrons are described by the Kondo Lattice model. Many heavy fermion metals have been identified as Kondo lattices, and often have the most pronounced deviation from normal metal behavior. The Kondo lattice model connects the microscopic properties of a lattice dense with local moments, through Kondo singlet formation, screening and scattering processes, and combines them with the RKKY moment-moment interaction, leading to a picture of the emergent macroscopic properties of heavy fermion metals.

The three-dimensional Kondo Lattice Hamiltonian is [3]

$$H_{KL} = \sum_{ij} t_{ij} c^{\dagger}_{i\sigma} c_{j\sigma} + \sum_{ij} I_{ij} \boldsymbol{S}_i \cdot \boldsymbol{S}_j + \sum_{i} J_K \boldsymbol{S}_i \cdot \boldsymbol{s}_{c,i}, \tag{1.8}$$

where the first term describes a single conduction band with hopping matrix t_{ij}, the second term describes the RKKY interaction I_{ij} between local moment spins $\boldsymbol{S}_i, \boldsymbol{S}_j$, and the third term the Kondo coupling J_K between a local moment and conduction electron $\boldsymbol{s}_{c,i}$.

The Kondo effect refers to the physics that follows from adding two ingredients: one (or more) magnetic ions, and a band of conduction electrons, due to their spins interacting. In H_{KL} this is mathematically expressed through the J_K term, showing how the magnetic moment of f electrons at site i, with spin $\boldsymbol{S}_i$, couples to the conduction electron spin $\mathbf{s}_i$ of conduction electrons. Kondo singlet structure constrains the coupling constant $J_K > 0$. The broad consequences of the Kondo effect can be divided into high and low energy regimes, separated by a characteristic energy scale called the Kondo temperature T_K, which is different depending on whether it is a lattice or single impurity model. At temperatures or magnetic fields $\frac{T}{T_K} \gg 1$, $\frac{H}{T_K} \gg 1$, the local moment(s) act as an incoherent inelastic scattering center for conduction

electrons, and when both $\frac{T}{T_K} \ll 1$, $\frac{H}{T_K} \ll 1$, the Kondo coupling dominates, entangling the moment and electron in a singlet ground state, whose low energy excitations are heavy Landau quasiparticles [1, 3, 2]. At low temperatures, the moments are strong elastic scattering centers, rendered spinless by conduction electron screening. In lattice systems, the onset of screening and how it relates to low temperature Fermi liquid or zero-temperature non-Fermi liquid behaviors is a more subtle matter. The Kondo interaction is named after the physicist Jun Kondo, who originally used this coupling exchange term in a single impurity model to perturbatively calculate the scattering rate and resistivity of rare-earth metals (cf. Section 1.1.2) [26, 27].

The moment-moment coupling seen in the Kondo lattice is of the Ruderman-Kittel-Kasuya-Yosida (RKKY) type, an indirect coupling mediated by hyperfine interactions with intervening conduction electrons, effectively acting as a typical magnetic exchange interaction. Two local moment spins $\mathbf{S}_i$, $\mathbf{S}_j$ at sites i and j, contribute coupling terms in the Kondo lattice Hamiltonian

$$H_{RKKY} = \sum_{ij} I_{ij} \mathbf{S}_i, \mathbf{S}_j$$

Where I_{ij} is a matrix element proportional to the inter-moment distance, hyperfine splitting, and effective conduction electron mass [28, 29, 30]. In the Kondo lattice, the RKKY term tends to order the localized moments, and in most real systems this exchange is antiferromagnetic, leading to magnetically ordered phases in the overall phase diagram.

1.1.4 Global phase diagram

The heavy fermion system clearly has varied and rich behavior, even if one analyzes them with rudimentary models. A key concept of quantum phase transitions and quantum criticality is that the zero temperature ground states and their QCPs are the real drivers of the finite temperature behavior. The global phase diagram was introduced to describe the quantum phases of antiferromagnetic Kondo lattice

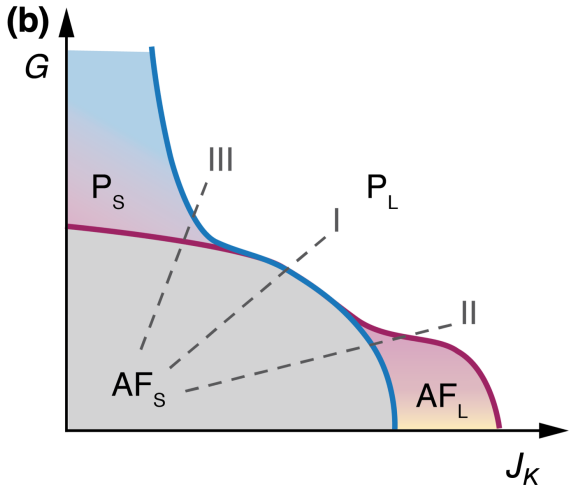

Figure 1.2 : Heavy fermion global phase diagram. [31, 32, 33, 34, 35, 36] The parameter G controls the amount of geometric frustration of local moments, while J_K modifies the magnitude of the Kondo coupling. AF labels phases with antiferromagnetic ordering of local moments, and P labels paramagnetic phases. Subscript L denotes large Fermi surface phases, and subscript S denotes small Fermi surface phases. The dashed lines, labelled "I", "II" and "III", illustrate three trajectories of quantum phase transitions. Near the borders of the AF phase boundaries, large magnetic fluctuations may lead to emergent exotic phases in heavy fermion systems.

systems, and subsequent works analyzed each phase transition type through three trajectories [31, 32, 37, 38]. Each phase is labeled according to local moment magnetic state (P=paramagnetic, AF=antiferromagnetic), and the size of the Fermi surface determines the subscript (S=small, L=large). The global phase diagram is shown in Fig. 1.2. This diagram assumes that $T = 0$, the RKKY exchange I is overall small compared to the bare conduction electron bandwidth D; the axes are shown in units of D.

Along the horizontal axis, J_K tunes the strength of the Kondo coupling. Since J_K generically favors Kondo singlets and causes the f fermions to participate in the electronic properties, this parameter can be thought of as tuning through Fermi surface reconstruction/destruction transitions. The vertical axis is controlled by the frustration parameter G, which tunes the amount of instability towards antiferromagnetic

ordering of the local moments. This instability essentially increases the quantum fluctuations of the local moments, but can physically manifest in a few forms. For instance, the RKKY could have competing components, such as antiferromagnetic interactions between both nearest-neighbor (n.n.) and next nearest-neighbor (n.n.n.) sites, forming the frustration parameter as $G = I_{nnn}/I_{nn}$, or one can situate the magnetic moments on a frustrated or low-dimensional lattice. Each of these serves to destabilize the Néel state, and encourage the system towards restoring spin rotational symmetry in paramagnetic phases, which can either break or preserve translational symmetry in spin Peierls or spin liquid phases, respectively.

The dashed lines mark three types of trajectories through phase space that quantum phase transitions might take. This depends on whether the blue (S-L critical Kondo breakdown, Fermi surface transition) or red (AF to P) phase boundary is encountered first. In all cases, the endpoint phases are the heavy Fermi liquid P_L phase, and the metallic antiferromagnet AF_S, and the line represents the tuning of some nonthermal parameter δ. The trajectories can be understood in the following way:

- *Trajectory I, critical Kondo destruction:*

  A direct AF_S to P_L second order phase transition. This phase transition for finite temperature is shown in Fig. 1.1, where δ_c can be labeled as a local QCP. This QPT has been evidenced in experiments as well. For instance, experimentalists measured a Fermi surface jump in the normal Hall effect across the QCP in $YbRh_2Si_2$ [16, 17]; another group observed coincident Kondo breakdown and AF order destruction in $CeRhIn_5$ based on de Haas-van Alphen measurements of the Fermi surfaces [39, 34, 35].

- *Trajectory II, Kondo destruction in AF order:*

  Here, the Kondo breakdown energy scale is separated from, and lies inside the magnetically ordered phase. The QCP between the AF_L and P_L phases is a Hertz-Moriya-Millis type QCP [40, 41, 42], since the heavy quasiparticles of

the P_L phase can form spin density wave type order in the AF_L phase [31]. Experimentally, this transition type was studied in $Ce_3Pd_{20}Si_6$ [33, 43].

- *Trajectory III, Kondo destruction outside of order:*
  The magnetically ordered phase is now separate from the Kondo breakdown scale, and the Kondo breakdown $S-L$ transition occurs within the paramagnetic states. From the AF_S phase, the P_S phase can be a spin liquid or spin Peierls state, where P_S can be a non Fermi liquid. This disordered phase of the moments persist across the P_S to P_L transition, eventually becoming a heavy Fermi liquid. In experiments, the frustrated and distorted kagomé Kondo lattice CePdAl [44, 36] was found to have such a type of QCP.

1.1.5 Spin-orbit coupling

Spin-orbit coupling (SOC) is an interaction between the spin and orbital degrees of freedom. Usually, SOC is considered a source of energy splitting of an orbital multiplet into energy level sets (along with crystal field effects), and if a well-separated two-level set is most energetically favorable, then a pseudospin-$\frac{1}{2}$ fermion can represent the resultant state. This treatment is used frequently as a first step to modeling the heavy transition metals: partially-filled $4d$ and $5d$ electron systems, such as the strontium ruthenates, pyrochlore iridates, and perovskites, which have a Hubbard energy on the scale of the conduction electron bandwidth, $U/D \sim 1$, and a SOC that is as relevant as the crystal field and kinetic terms [45]. In heavy fermion systems, further or more direct treatment of the spin orbit coupling has been typically neglected in models, since it is the large Coulomb interaction ($U/D > 1$, on the scale of Mott insulators) that is the largest and most relevant energy scale, aiding in splitting the f multiplet into the two-state system amenable to models, and leading to magnetism and other strongly correlated effects.

There have been some recent developments that have brought SOC back into direct consideration in heavy fermion systems. In the past, the orbital structure was mainly

acknowledged in works on multiorbital Kondo effects, orbital anisotropy, or orbitally-selective Kondo effects.With the explosion of new heavy fermion superconductors that have been discovered in the last couple decades, the SOC has been shown to play an important role in the *noncentrosymmetric* (i.e. lacking inversion symmetry) variety of heavy fermion superconductors (such as $CePt_3Si$)[46, 47], as it lifts spin degeneracy [48], and enhances the mixing of even and odd parity states, which are both needed for the superconducting pairing [49].

It is my view that the importance of SOC in heavy fermion systems has been under-appreciated, because it can alter the symmetry of the system, which we will see later has important consequences for band structures and topology. A simple observation supports this statement. In $4f$ materials, the size of the SOC is lesser than the Coulomb energy, yet very substantial, somewhere between that of the $4d$ and $5d$ electron systems. Phenomena in those systems driven by SOC should be relevant in heavy fermion systems as well. The predominant effect that SOC facilitates is *band inversion*, that is, a reordering of energy bands, a mixing of quantum numbers into pseudospin degrees of freedom, and a change in symmetry of the bands that may allow crossing at a point, instead of opening a gap [50, 51]. Band inversion is a crucial ingredient in realizing many varieties of topological phases, such as nontrivially configuring parity eigenvalues in and making surface states gapless in topological insulators; or producing the gaplessness in topological semimetals, whether the gapless manifold is a point, line, loop, or sphere [52, 53, 54, 55]. Earlier works have analyzed topological Kondo insulator states that effectively treat the f electron's SOC through an odd-parity form factor in the Kondo hybridization [56, 57, 58, 59, 60]. The precise consideration of the SOC in a realistic treatment and context is warranted, to distinguish whether the form of SOC makes a difference to topological phases. Intuitively, any type of band inversion mechanism should fulfill the same role toward topological phases, since its utility in topological systems is how it affects the Hamiltonian symmetry. For heavy fermion systems, it may be that there are a wide variety

of mechanisms that can play this role, so it is important to study the SOC more generally [61, 17].

1.2 Topological metals

This thesis work has an overall goal to explore the metallic topological phases driven by strong correlations in heavy fermion systems. Since metallic Kondo systems yield an abundance of information from transport and thermodynamic signatures, it is reasonable to think topological metallic states should yield rich insights. The transport carriers can tell us about the local moments, via their participation in the Fermi surface via the Kondo effect. For topological phases, may provide insight into the Berry phase effects as well as eventually studying the internal quantum degrees of freedom that Kondo singlet entanglement can make macroscopic. It also intuitively means that experiments on topological Kondo metal candidates could be performed in rapid dialogue with theory, in ways that are perhaps a barrier for other strongly correlated topological platforms.

The thesis deals with two types of topological metals: time-reversal symmetry broken (TRSB) metals with a finite Fermi surface in frustrated two dimensional Kondo lattices, and Weyl semimetal phases in both TRS preserved and TRSB versions of a Fu-Kane-Mele [62] Anderson lattice model in the strongly correlated (Kondo) regime. The next half of the introduction gives an overview of the concepts in topology that are relevant to subsequent chapters, and relates these phenomena back to heavy fermion systems.

1.2.1 Topology, Berry curvature, and invariants

The physical quantity that lies at the heart of an electronic topological phase's "topologicalness" is the Berry phase. The Berry phase is the condensed matter manifestation of the geometric phase acquired when a wave system explores the landscape of its parameter space as a result of a cyclic adiabatic process. In condensed matter

systems, a particle in state n acquires a Berry phase γ_n as the Hamiltonian parameters are varied around a closed manifold $\mathcal{S}$ without eigenstate transitions away from n (*i.e.*, adiabaticity is preserved). The Berry phase allows us to calculate related topological invariants in topological metallic systems, as the nontriviality of the electronic wavefunction is reflected in transport measurements.

A related quantity is the Berry curvature $\mathbf{\Omega}$, which plays a part in the semiclassical equation of motion of Bloch electrons, $\hbar\mathbf{v} = \nabla_{\mathbf{k}}\varepsilon_{\mathbf{k}} - \boldsymbol{\mathcal{E}} \times \mathbf{\Omega}$, with $\varepsilon_{\mathbf{k}}$ the one electron energy dispersion, and $\boldsymbol{\mathcal{E}}$ the applied electric field (it is assumed here no magnetic field is applied). This is why the Berry curvature is sometimes referred to as a fictitious magnetic field, because it plays an analogous role in momentum space to the magnetic field in the Lorentz force equation in real space. The Berry curvature of a band indexed by n is defined as

$$\mathbf{\Omega}_n(\mathbf{k}) = \nabla_{\mathbf{k}} \times \mathcal{A}_n(\mathbf{k}) \tag{1.9}$$

$$= (\Omega_n^{yz}(\mathbf{k}), \Omega_n^{zx}(\mathbf{k}), \Omega_n^{xy}(\mathbf{k}))\,, \tag{1.10}$$

$$\Omega_n^{ab}(\mathbf{k}) = \sum_{n \neq n'} \mathrm{Im} \frac{\langle n\mathbf{k}|\partial_{k_a} H_{\mathbf{k}}|n'\mathbf{k}\rangle \langle n'\mathbf{k}|\partial_{k_b} H_{\mathbf{k}}|n\mathbf{k}\rangle}{(\mathcal{E}_n - \mathcal{E}_{n'})^2}. \tag{1.11}$$

In the one electron band theory of a time reversal symmetry broken system, the intrinsic Hall conductivity σ_{ab} is related to the Chern number C_n, a topological invariant, as

$$\sigma_{ab} = \frac{e^2}{2\pi\hbar} \sum_n \int_{BZ} d^3\mathbf{k} f(\varepsilon_{\mathbf{k}}) \Omega_n^{ab}(\mathbf{k}) \tag{1.12}$$

$$= \begin{cases} \frac{e^2}{2\pi\hbar}\epsilon^{abc} K_c, & \text{band } n \text{ partly occupied} \\ \frac{e^2}{2\pi\hbar} C_n \mathbf{G}_n^C, & \text{band } n \text{ fully occupied} \end{cases}, \tag{1.13}$$

where n indexes all bands, $f(\varepsilon_{\mathbf{k}})$ is the Fermi occupation function, K_c is a non-quantized number for topological metals with a finite Fermi surface, ϵ^{abc} is the Levi-Civita tensor, and for completely occupied bands C_n gives the quantized Chern number on lattice planes indexed by the primitive reciprocal lattice vector $\mathbf{G}_n^C$ [25]. If

the highest occupied bands are partially occupied and form Fermi surfaces $\mathcal{S}_\alpha$, this expression can be expanded via integration by parts to become an integral over the Fermi surfaces. If for simplicity one assumes there is a single surface, and that bands below the Fermi level intersecting the Brillouin zone boundary do not contribute, we have

$$\boldsymbol{K} = \frac{1}{2\pi}\int_{\mathcal{S}} \Omega_{\mu\nu}(\boldsymbol{s})\mathbf{k}_F(\boldsymbol{s})ds^\mu \wedge ds^\nu, \tag{1.14}$$

$$\tag{1.15}$$

where $\boldsymbol{s} = \{s^1, s^2\},\ \boldsymbol{s} \in \mathcal{S}$ is a parameterization on the Fermi surface. In this sense, the Berry curvature is considered to be a Fermi surface property [25].

On the other hand, in Weyl semimetals, one uses a *local* integral in the Brillouin zone as a topological invariant. This is given by the Berry flux Φ_n through a surface manifold ($\mathcal{S}$) enclosing a single Weyl node (band touching point) as

$$\Phi(\mathcal{S}) = \frac{1}{2\pi}\int_{\partial\mathcal{S}} d\boldsymbol{S}\cdot\boldsymbol{\Omega}(\mathbf{k}) \tag{1.16}$$

$$= \frac{1}{4\pi}\int \frac{d^3k}{(2\pi)^3}\nabla_{\mathbf{k}}\cdot\boldsymbol{\Omega}(\mathbf{k}), \tag{1.17}$$

At a Weyl node degeneracy, one can see the denominator of Eq. 1.11 is zero, causing a singularity in the Berry curvature field in the momentum space [Eq. (1.10)]. In this way, the Weyl nodes and anti-nodes can be distinguished by the sign of this invariant, and the Berry flux density is $\nabla\cdot\boldsymbol{\Omega} = \pm 4\pi\delta^3(\mathbf{k})$, so that the Berry flux is

$$\Phi(\mathcal{S}) = \pm\frac{1}{4\pi}\int \frac{d^3k}{(2\pi)^3}4\pi\delta^3(\mathbf{k}) = \pm 1.$$

This tells us that the Berry flux is a quantized number that counts the number and sign of Berry charges (monopoles) in a given system. This is the reason for the "monopole" terminology: the Berry flux acts like the total charge of the Weyl point, and their associated Berry curvature (magnetic) field has a monopole or anti-monopole configuration. When the Weyl (anti-)nodes are pinned to the immediate vicinity of the Fermi energy, as happens in our Weyl-Kondo semimetal solution, the

monopoles and associated Berry curvature singularities appear very close to the Fermi surface. In other words, the Fermi surface comprises tiny Fermi pockets that surround the Weyl (anti-)nodes, and states on the Fermi surface have a very large Berry curvature.

1.2.2 Frustrated magnetism and chiral spin liquids

This section addresses Ch. 2, which models chiral spin liquids on the Heisenberg spins of two-dimensional frustrated Kondo lattice models. It is best to know what each component of such a model means, and how it normally acts on its own before combining concepts together.

"Frustration" is a quantity or quality of a magnetic system that prevents it from realizing a magnetically ordered state. Such a broad definition encompasses most any thing that can destabilize the Néel state and restore spin rotational symmetry. Usually in highly frustrated systems, more exotic disordered paramagnetic states can be much more energetically favorable at low temperatures, such as in spin Peierls or spin liquid phases. Magnetic states that arise from frustration can also suppress the Néel temperature to $T_N = 0$, which is valuable for understanding quantum critical properties [63].

There are three mechanisms of frustration that are relevant in this thesis:

1. *Reduced dimensionality.*

   A physical spin has all spatial directions at its disposal, but in dimensions $d \leq 2$ experiences highly anisotropic (and therefore strong) interactions and fluctuations along the spatially available directions. This form of frustration in low-dimensional systems was formally proven by Mermin and Wagner, yielding the following theorem [64, 65]:

   Theorem 1.1

   In the quantum, isotropic Heisenberg model in $d \leq 2$ with short range interactions and for arbitrary spin s, there is no spontaneously broken spin symmetry

for $T > 0$.

To illustrate the physical mechanism of the Mermin-Wagner theorem, one can estimate the fluctuations of the order parameter [66]. By presuming an antiferromagnetically ordered ground state, the sublattice magnetization M can be written as the sum of static and fluctuating parts:

$$M = S - \Delta S = S - \frac{1}{N}\sum_{\mathbf{k}} \langle a^{\dagger}_{\mathbf{k}} a_{\mathbf{k}} \rangle \tag{1.18}$$

At low T, the sublattice magnetization fluctuations are approximately

$$\Delta S \sim \int k^{d-1} \frac{dk}{k}, \tag{1.19}$$

which clearly diverge for $d = 1$, indicating that the presumption of order was incorrect; but most of all that fluctuations are very strong in low dimensions. This means that low dimensional systems experience frustration through strong thermal and quantum fluctuations that preserve continuous symmetries [67].

2. *Frustrated magnetic interaction.*

   While introducing the global phase diagram in Sec. 1.1.4, I used the example of the next-nearest neighbor RKKY interaction I_{nnn} being tuned relative to the nearest neighbor RKKY interaction I_{nn}. This would destabilize nearest-neighbor Néel correlations for suitable lattices [63]. An example of anisotropy-induced frustration is the $J_1 - J_2$-model on the square lattice, where $J_1(J_2)$ is the (next-)nearest neighbor interaction with $J_1 = 2J_2$. In Ch. 2, this model becomes the basis for the RKKY part of a Kondo lattice model. There we take advantage of the large N limit to characterize the quantum chiral spin liquid phases [64].

3. *Geometric frustration.*

   In this frustration type, the spins are arranged on a structure that itself destabilizes the Néel state. This generically occurs on lattices with an odd number of

spins in the magnetic unit cell (non-bipartite lattices), or arrangements where spins point in a non-collinear configuration; any configuration where there are spins unable to satisfy the conditions of Néel order [63]. Examples of geometrically frustrated lattices are the triangular lattice, the pyrochlore lattice, and the kagomé lattice, the last of which is used for the second frustrated Kondo lattice model in Ch. 2.

Once frustration destroys antiferromagnetism, there are a few phases which can take its place. Most are some type of valence bond state, that is, there is some configuration of spin pairs in a rotationally invariant singlet state across the material [68, 69, 70, 71, 72]. Another possibility are spin liquid phases, which are more likely to occur in systems with small spin quantum numbers, since this enables comparatively larger quantum fluctuations [63]. It is also possible for valence bond states to compete with spin liquid phases [73].

However, because we are motivated by discovering links between AHE, frustration, and quantum criticality, we are interested in frustrated quantum antiferromagnetic states that spontaneously break time reversal symmetry: chiral spin liquids [74]. A mean field theory treatment of the Heisenberg model by Refs. [75, 76], the valence bond operator is written in terms of fermions as

$$\boldsymbol{S}(\mathbf{x}) \cdot \boldsymbol{S}(\mathbf{y}) = \frac{1}{2} c^\dagger_\alpha(\mathbf{x}) c_\beta(\mathbf{x}) c^\dagger_\beta(\mathbf{y}) c^\dagger_\alpha(\mathbf{y}) - \frac{1}{4} n^c(\mathbf{x}) n^c(\mathbf{y}), \tag{1.20}$$

where the second term contributes an arbitrary energy shift that can be absorbed into the chemical potential. The Hamiltonian becomes

$$\mathcal{H} = \frac{I}{2} \sum_{\mathbf{x},j} c^\dagger_\alpha(\mathbf{x}) c_\beta(\mathbf{x}) c^\dagger_\beta(\mathbf{x} + \hat{e}_j) c^\dagger_\alpha(\mathbf{x} + \hat{e}_j), \tag{1.21}$$

where $\hat{e}_j$ are unit vectors along the x_j valence bond directions, subject to the constraint $c^\dagger_\alpha(\mathbf{x}) c_\beta(\mathbf{x}) = 1$. Once the problem is recast into a Lagrangian formalism, a Hubbard-Stratonovich transformation simplifies the spin-spin terms by introducing complex link variable fields χ_j[77]. These fields are parametrized similar to a

Peierls term, as $\chi_j(\mathbf{x},t) = \rho_j(\mathbf{x},t)\exp(i\mathcal{A}_j(\mathbf{x},t))$. Next, a saddle point approximation is used, since the solutions determine the action extremizing configurations of the $\rho_j(\mathbf{x},t)$, $\mathcal{A}_j(\mathbf{x},t)$ parameters. The valence bond crystal phases break translation and/or rotation invariance so they are not considered here. Instead, assuming the bond amplitude is uniform in time and space $\rho_j(\mathbf{x}) = \rho$, note that the circulation of the phases is equivalent to the flux around a plaquette, where a plaquette is the shortest possible closed loop formed from adjacent lattice bonds: $\sum_{\text{plaq.}} \mathcal{A}_j(\mathbf{x},t) = \mathcal{B}$. For time reversal symmetry to be broken, $\mathcal{B}$ must a constant value besides 0 and π, mod 2π [77]. States that satisfy this condition are chiral.

1.2.3 Topological semimetals

We now turn our focus on three dimensional topological semimetals (TSMs). This phase of matter is characterized by a low-dimensional Fermi surface that encloses zero Luttinger volume, and some topological invariant that uniquely characterizes it. In other words, TSMs are a category of non-trivial phases that are gapless in the bulk spectrum. This TSM category encompasses Dirac, quadratic, Weyl semimetals (with point nodes), and semimetals with line, loop, and sheet node geometries [52, 78, 55]. Topological materials all possess bulk-boundary correspondence, which is the guaranteed presence of nontrivial surface states that correspond uniquely to the nodal geometry (or nontrivial insulator gap), usually involving a surface projection of a bulk degeneracy [77], and can serve as another diagnostic of the TSM type. The topological invariants are usually some quantized number (modulo 2π) of an area integral over highly singular Berry curvature or contour integral over Berry phase that winds nontrivially (c.f. Section 1.2.1).

Crucially, this zoo of TSMs only manifest in these particular patterns of nodal geometry - in particular locations of the Brilluoin zone - because of generically predictable crystal group symmetry properties, and a few other Hamiltonian ingredients. However, since this thesis is focused on Weyl semimetal phases, that is the example

we will use. Crystal lattices naturally possess lattice points, inversion centers, rotational axes and mirror planes, where from some point $\mathbf{r}$, the associated symmetry operation $\mathcal{S}$ maps the Hamiltonian $H(\mathbf{r}) \to H'(\mathbf{r}')$ and $\mathbf{r}'$ makes use of those special points/lines/etc. as reference:

$$H'(\mathbf{r}') = \mathcal{S}^{-1} H(\mathbf{r}) \mathcal{S}. \tag{1.22}$$

Consequentially, the eigenenergies will be degenerate at the inversion centers, and along rotational axes and mirror planes. In particular, nonsymmorphic symmetries are a reliable starting choice for a crystal lattice system, because they permit low-dimensional manifolds of energy degeneracy that can always be found on the Brillouin zone boundary (BZB)[†]. Nonsymmorphic operations leave lines and loops of degeneracy, creating a nodal line or loop semimetal (the degeneracy depends on the other lattice symmetries). The nonsymmorphic space groups are generated when an n-fold mirror or rotation operation is compounded with a fractional translation vector (i.e. non-Bravais lattice vectors) that takes n-many translations to traverse the unit cell, usually along a translation vector in the mirror plane or along the rotation axis [55, 79]. Because the fractional translation vector repeats n-times in the unit cell, this often encompasses n-fold sites within unit cell, or from the opposite perspective, the unit cell has been expanded to incorporate n sites, where it is often said, e.g. as for $n = 2$, that the unit cell has been "doubled". In momentum space, every n-fold expansion of the unit cell corresponds to an n-fold reduction of the Brillouin zone, or "Brillouin zone folding." Since symmetry begets degeneracy, nonsymmorphic symmetries beget degeneracy affixed to the Brillouin zone boundary.

As an illustrative example of how a nonsymmorphic symmetry works, consider the Shastry-Sutherland lattice (SSL) in Fig. 1.3. Like all nonsymmorphic space groups have multiple (four) sites per unit cell. The SSL has wallpaper group $p4g$, which has fourfold rotation symmetry and the intersection of perpendicular glide axes at each

[†]Of all 230 space groups, 157 are nonsymmorphic.

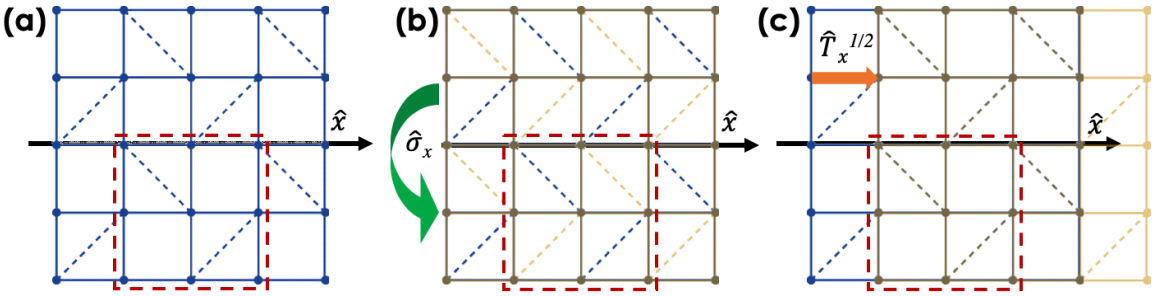

Figure 1.3 : (a) The Shastry-Sutherland lattice, with four-site unit cell indicated with the dotted line. (b) shows the first mirror (σ_x) operation of this lattice's nonsymmorphic glide symmetry $G = \{\hat{\sigma_x}|\hat{t}_x^{1/2}\}$, followed by (c) a half unit cell translation, $\hat{t}_x^{1/2}$.

site, plus twofold rotations and perpendicular reflection axes at the center of each square. The example nonsymmorphic glide symmetry to consider is $G = \{\hat{\sigma_x}|\hat{t}_x^{1/2}\}$, for the glide line shown on the $\hat{x}$ axis in Fig. 1.3. The mirror $\hat{\sigma_x}$ (Fig. 1.3(b)) reflects the lattice across the $\hat{x}$ axis, then a translation by half a Bravais lattice vector, $\hat{t}_x^{1/2}$ aligns the bonds again (Fig. 1.3(c)). In k space, the four site unit cell causes a folding of the BZ, causing degeneracy at the boundary.

However, the degeneracies created by nonsymmorphic symmetries are robust, so a nonsymmorphic crystal with SOC is a natural starting point to search for topological semimetals. If spin, orbital, flavor, and so on are included, a semimetal line can be multiply degenerate. It just so happens that the degeneracy at these lines are protected by the lattice translation symmetry, such that SOC cannot open a gap [55, 80]. However, we know SOC facilitates band inversion, which is a first step toward topological materials. Other mechanisms that can produce band inversion (but which perhaps do not have the same beneficial translation properties) are lattice strain and scalar relativistic effects [81, 82, 83]. For a minimal model, the coincidence of a nonsymmorphic symmetry plus SOC may produce a Dirac semimetal degeneracy at a BZB, like the one that appears for the diamond lattice at the X point [62, 84].

A Dirac semimetal has two pairs of twofold-degenerate bands, which are fourfold

degenerate only at the Dirac point, and importantly, the bands disperse linearly in all directions from the Dirac point. Their multiplicity can be reduced (toward a Weyl semimetal) by breaking inversion symmetry or time reversal symmetry [55, 85, 86, 87], with the option of preserving the composite PT-symmetry [88], or breaking both symmetries [89]. Generally, breaking TRS causes the Dirac hourglass to split into a pair; breaking ISB causes two pairs to split off. The nodal points remaining are Weyl nodes, constituting the Weyl semimetal (WSM) topological phase. The associated topological invariant is the Berry monopole charge, as explained in Sec. 1.2.1 and shown in Eq. 1.18.

A particularly important property of nonsymmorphic semimetals, is that some nonsymmorphic space groups can enforce a semimetal phase at a particular band filling, based on group symmetry arguments [90]. In principle, this means that if one had a nonsymmorphic system, plus a band inversion mechanism, plus a broken time-reversal or inversion symmetry, there is guaranteed to be a nodal gapless band touching somewhere in the spectrum (modulo some filling factor), on a set of BZB momenta. Until recently, these types of degeneracies have only been used in non-interacting electron systems. A central ingredient of this thesis is to explore its role – including its cooperation with correlation effects – in strongly correlated electron systems.

1.3 Heavy fermion systems as a topological metals platform

There are a few compelling reasons why the heavy fermion systems should be considered to find topology, and why the topologists should consider looking into the heavy fermion systems. First, it has recently been estimated that around 27% of the $\sim$25,000 materials in the ICSD database host non-trivial topological phases [91, 92]. This means that even in Kondo and heavy fermion systems, there ought to be examples of topological phases, especially nodal semimetals. There is some supporting evidence for this assertion. The SOC is an energetically relevant scale in heavy fermion

materials, so its band inversion effects (including topological phases) should be both easily discovered and considered theoretically in heavy fermion systems.

Second, there are also several compelling questions that can be asked once strong correlations driven topology is considered. Heavy fermion systems link the volume enclosed by the Fermi surface to the size of the NHE. Can the Berry curvature singularity on the Fermi surface be the quantity related to the AHE signal in heavy fermion systems? Since the f electron magnetism derives from the dominant energy scale in the system, how would the strong correlations possibly alter the band structure in the vicinity of nodes? Since the Kondo reconstruction transition changes the effective system filling, how will this affect the nonsymmorphic enforcement of degenerate quasiparticle states?

Chapter 2

Anomalous Hall effect and quantum criticality in geometrically frustrated heavy fermion metals

2.1 Introduction

Heavy-fermion metals are prototypical systems to study quantum criticality [93, 94]. The simplest model to describe these systems is a Kondo lattice, which comprises a lattice of local moments and a band of conduction electrons. The local moments are coupled to each other by the Ruderman-Kittel-Kasuya-Yosida (RKKY) interactions, and are simultaneously connected to a band of conduction electrons through an antiferromagnetic (AF) Kondo exchange interaction (J_K). In recent years, it has been realized that the effect of geometrical frustration is a potentially fruitful but little explored frontier. From a theoretical perspective, geometrical frustration enhances G, the degree of quantum fluctuations in the magnetism of the local-moment component, and a $J_K - G$ phase diagram at zero temperature has been advanced [32, 38]. Figure (2.1a) illustrates the proposed global phase diagram [32]. From a materials perspective, there is a growing effort in studying frustrated Kondo-lattice compounds [95, 96, 97, 98, 99, 17].

The pyrochlore heavy-fermion system $Pr_2Ir_2O_7$ is one such example. Both the measured magnetic susceptibility and specific heat [99] suggest the presence of Kondo coupling between the Ir d-electrons and the local f-moments of Pr. No magnetic order is found down to very low temperatures, suggesting that the f-moments of Pr develop a quantum spin liquid (QSL) ground state [99]. In addition, experiments found a sizeable zero-field anomalous Hall effect (AHE) for magnetic field applied along the [111] direction [100, 101], revealing a spontaneous time-reversal-symmetry-breaking

(TRSB) state.

This system is of considerable theoretical interest [102, 103, 104, 105, 106, 107, 108]. With a few exceptions [109], the role of the Kondo effect has not been discussed in this context, and neither has its relationship with the observed quantum criticality. Yet, the recent observation of a large entropy and a divergent Grüneissen ratio [110] clearly point to the importance of the Kondo coupling and the role of a proximate heavy-fermion quantum critical point (QCP). In the case of AF heavy-fermions systems, the normal Hall effect has been successfully used to probe the evolution of the Fermi surface across the QCP and thereby the nature of quantum criticality [17]. Given that the AHE is also intrinsically a Fermi surface property (other than contributions from fully occupied bands) [25], we are motivated to address whether it can serve as a diagnostic tool about the QCP in the present setting. In addition to elucidating the AHE, studying this issue promises to bring about the much-needed new understanding of quantum phases and their transitions in geometrically-frustrated heavy-fermion metals [17]. Given the complexity of the three-dimensional pyrochlore lattice, we will gain insights from related but simpler models.

In this Chapter, we study both the frustrated $J_1 - J_2$ quantum Heisenberg model on a square lattice as well as the J_1 only model on the Kagomé lattice with a Kondo coupling to conduction electrons. For the square lattice, we consider the regime of strong frustration where a chiral spin liquid (CSL) phase [74] becomes energetically competitive in the large-N limit. The Kagomé lattice, representing a layer perpendicular to the [111] direction of the pyrochlore lattice, is a two-dimensional network of corner-sharing triangles [Fig. (2.1d)]with a strong geometrical frustration. A CSL phase is found in a spin-$\frac{1}{2}$ model on the Kagomé lattice [111, 112]. Using the large-N limit [113], we will also study the CSL physics on this lattice. We develop the method to calculate the AHE in both a Kondo-destroyed (P_S) and a Kondo-screened (P_L) paramagnetic phase. We show that each phase may have a sizable AHE. Moreover, across a QCP, the AHE jumps when the Fermi surface suddenly reconstructs.

2.1.1 Recent experiments on $Pr_2Ir_2O_7$

There are several exciting recent experimental developments on $Pr_2Ir_2O_7$ and its close chemical cousins. In Ref. [114], authors mapped out the predicted quadratic band touching using angle-resolved photoemission spectroscopy (ARPES). This is supported by first-principles calculations, which together is evidence that $Pr_2Ir_2O_7$ is in a Luttinger semimetal phase, where the long-range Coulomb screening at the node likely plays a role in observed non-Fermi liquid behavior, predicted in Refs. [105, 106]. The point node is a fourfold degenerate of Γ_8 non-Kramers doublets protected by time-reversal symmetry and the fourfold-rotational symmetry within the O_h point group at Γ. The authors also remark that the quadratic node is more or less exactly at the Fermi energy, but no explanation is offered. In Ref. [115], authors used electron doping via subsitution of Pr to Nd and hole doping to tune the one-electron bandwidth and band filling, yet found that in the paramagnetic phase, the quadratic band touching is robust in the paramagnetic pyrochlore iridates.

However, in Chapters **??**, a time-reversal symmetric Weyl-Kondo semimetal model is put forth where the Weyl-Kondo nodes can be "Kondo pinned" to the Fermi energy via nonsymmorphic symmetry and strong correlations, albeit the nodes are at the zone boundary [116, 117]. Coincidentally the Weyl-Kondo semimetal is implemented on the diamond lattice, which has the same space group (no.227, $Fd\bar{3}m$) as the pyrochlore lattice. Future work should determine whether the Kondo-pinning concept could be extended to other symmetries or the zone center.

Additionally, several other important recent contributions have shed light on various aspects of $Pr_2Ir_2O_7$. From characterizing the low-frequency electrodynamic response of $Pr_2Ir_2O_7$ thin films with THz spectroscopy, the authors of Ref. [118] find that the finite temperature dc resistivity minimum can be attributed to competition between plasma frequency and scattering rates. In Ref. [119], doping the system close to the metal-insulator transition ($Nd_{0.5}Pr_{0.5}Ir_2O_7$) demonstrated that for an applied magnetic field H$\|$ [001], the magnetotransport showed a Hall signature of the

semimetal phase as the magnetic moments transitioned from the magnetically ordered insulating all-in-all-out state to 2-in-2-out state, and later Hall experiments gathered more evidence of a Weyl semimetal phase [120].

Finally, a very recent study tuned $Y_{1-x}Pr_xIr_2O_7$ magnetically via substitution of nonmagnetic yttruim to magnetic praseodymium; this tunes the $f-d$ interaction dictating the Kondo effect, which screens the local Pr^{3+} moments from ordering except for $x \geq 0.8$ [121].

2.2 Frustrated Kondo-lattice models

We study the following Hamiltonian:

$$H = H_f + H_{d,0} + H_K. \tag{2.1}$$

Here H_f describes a Heisenberg model. For the square lattice case, H_f includes both J_1 and J_2 couplings between the nearest neighbors (nn, $\langle\rangle$) and next-nearest neighbors (nnn,$\langle\langle\rangle\rangle$). We focus on the maximally frustrated case of $J_2/J_1 = 1/2$. For the Kagomé case, the lattice is geometrically frustrated and it suffices for H_f to only contain the nn term. For both models with H_f alone, CSL states appear in the large-N limit [74, 75].

The local moments are coupled to a band of conduction electrons, described by $H_{d,0} = -\sum_{ij,\alpha}(t_{ij}d^\dagger_{i\alpha}d_{j\alpha} + h.c.)$, through an AF Kondo interaction J_K, specified by $H_K = J_K \sum_i \boldsymbol{s}_i \cdot \boldsymbol{S}_i$. Here, $\boldsymbol{s}_i = \sum_{\alpha,\beta} \frac{1}{2} d^\dagger_{i\alpha}\boldsymbol{\sigma}_{\alpha\beta}d_{i\beta}$ is the spin of the conduction electrons, with $\boldsymbol{\sigma}$ describing the Pauli matrices. We take $t_{\langle ij\rangle} = t = 1$ as the energy unit.

We use the Schwinger fermion representation for the f-moments $\boldsymbol{S}_i = \sum_{\alpha,\beta} \frac{1}{2} f^\dagger_{i\alpha}\boldsymbol{\sigma}_{\alpha\beta}f_{i\beta}$, with the constraint $\sum_\alpha f^\dagger_{i\alpha}f_{i\alpha} = 1$, so that $H_f = \sum_{\alpha,\beta,ij} \frac{J_{ij}}{2} f^\dagger_{i\alpha}f_{i\beta}f^\dagger_{j\beta}f_{j\alpha} - \frac{J_{ij}}{4}n_{i\alpha}n_{j\beta}$. In a large-$N$ approach [75], the spin index $\alpha = 1, 2, \ldots, N$, and the constraint is enforced by a Lagrangian multiplier λ_i. Both the Heisenberg term and the Kondo term are decoupled by a Hubbard-Stratonovich (HS) transformation. The large-N

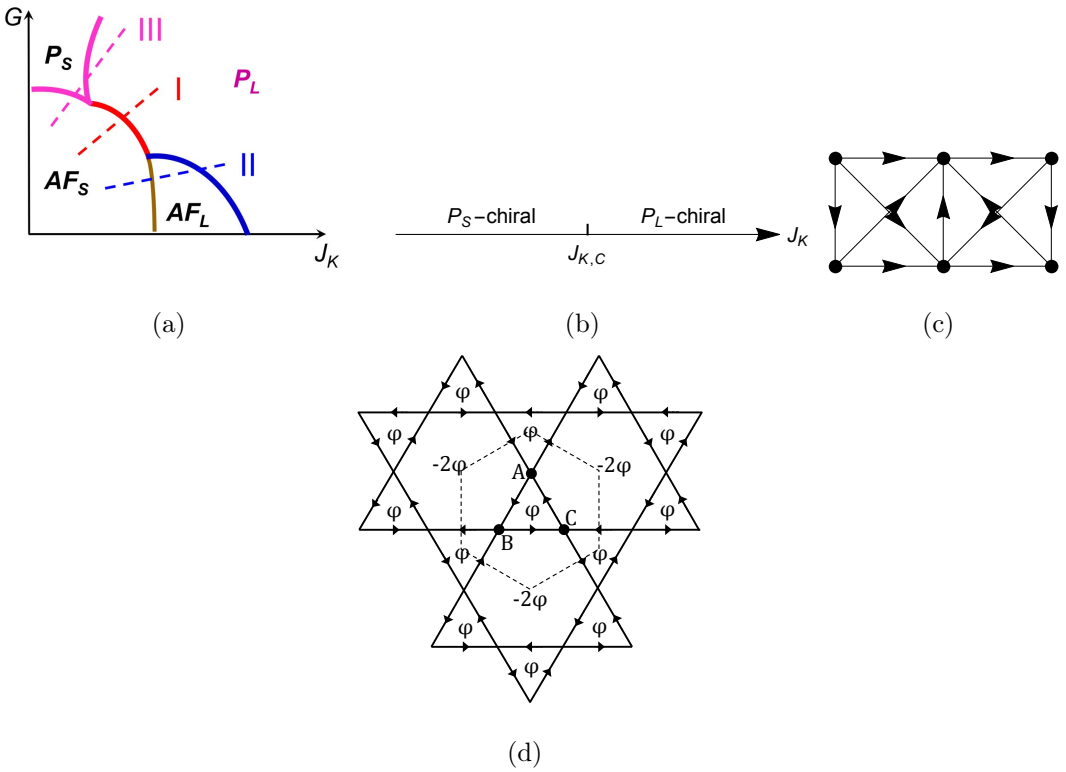

Figure 2.1 : (a) The global phase diagram of Kondo lattice systems [32]; (b) In highly frustrated regime (large, fixed G), J_K tunes through a Kondo-destruction QCP (at $J_{K,c}$) from a Kondo-destroyed chiral spin liquid ($P_{S,chiral}$) to a Kondo-screened phase ($P_{L,chiral}$). The χ fields of the square lattice are shown in the π-flux state (without the diagonal bonds) and the CSL state (c), and in the CSL state on the Kagomé lattice (d): the arrows denote the sign of gauge field A_{ij}, and ϕ is the flux through a triangle.

limit leads to

$$H_{eff} = H_{QSL} + H_{d,0} + H_{K,eff} + E_c, \tag{2.2}$$

with

$$H_{QSL} = -\sum_{ij,\alpha} \frac{J_{ij}}{2}(\chi_{ji} f^\dagger_{i\alpha} f_{j\alpha} + h.c.) - \sum_{i,\alpha} \lambda_i (f^\dagger_{i\alpha} f_{i\alpha} - 1/2),$$

$$H_{K,eff} = -\sum_{i,\alpha} \frac{J_K}{2}(\pi_i d^\dagger_{i\alpha} f_{i\alpha} + h.c.),$$

and

$$E_c = \sum_{ij} NJ_{ij}|\chi_{ij}|^2/2 + \sum_i NJ_K|\pi_i|^2/4.$$

The HS fields are defined as $\chi_{ij} = \sum_\alpha \langle f^\dagger_{i\alpha} f_{j\alpha}\rangle$ and $\pi_i = \sum_\alpha \langle f^\dagger_{i\alpha} d_{i\alpha}\rangle$. Both can be decomposed into amplitudes and phases: $\chi_{ij} = \rho_{ij}e^{iA_{ij}}$, $\pi_i = \rho_{K,i}e^{iA_{K,i}}$. The Kondo parameter π_i can be taken to be real, with its phase absorbed into the field λ_i, i.e. $\pi_i \to \rho_{K,i}$.

By minimizing the total energy of H_{eff} in Eq. (2.2), we obtain the phase diagrams containing the chiral states, in which J_K tunes the system from the P_S to P_L phases (see Appendix 7). Across a second-order Kondo-destroyed $P_{S,chiral}$ to $P_{L,chiral}$ quantum phase transition, Fig. (2.1b), we consider a power-law form for the Kondo hybridization amplitude:

$$\rho_K(J_K) = \rho_r\Big(\frac{J_K - J_{K,c}}{J_K}\Big)^{1/2} \quad , \tag{2.3}$$

for $J_K > J_{K,c}$ and $\rho_K = 0$, for $J_K < J_{K,c}$. We take $J_{K,c}$ as the value where the $P_{L,chiral}$ state becomes energetically competitive and ρ_r to be the saturation value of ρ_K; both values are adopted from the self-consistent calculation for a given set of (n_d, J_1) (see Appx. 7).

2.3 Mechanism of the Anomalous Hall effect

2.3.1 The Kondo destroyed P_S phase

In the Kondo-destroyed P_S phase, the static hybridization amplitude vanishes, $\langle\rho_{K,i}\rangle = 0$. However, we show that there are TRSB terms in the effective interactions among the conduction electrons, which are mediated by the spinons via Kondo couplings. Such terms yield a zero-field AHE.

We will single out the TRSB terms. The TRSB order parameter of the CSL is the spin chirality,

$$\hat{E}_{ijk} = \boldsymbol{S}_i \cdot (\boldsymbol{S}_j \times \boldsymbol{S}_k) \quad , \tag{2.4}$$

where the indices $\{i, j, k\}$ mark the three sites of an elementary triangle of the lattice. In the CSL state, $E_{ijk} = \langle \hat{E}_{ijk} \rangle = 2i(P_{ijk} - P_{ikj})$, where $P_{ijk} = \chi_{ij}\chi_{jk}\chi_{ki}$. On symmetry grounds, we expect E_{ijk} to be coupled to the composite chiral operator of the conduction electrons, $\boldsymbol{s}_i \cdot (\boldsymbol{s}_j \times \boldsymbol{s}_k)$. With this guidance, we obtain the coupling from integrating out the f-fermions and expanding in powers of J_K; this can be represented by triangular diagrams (Appendix 7), similar to what is used in deriving a chiral current. We find

$$\begin{aligned} H_{\text{chiral}} &= \sum \frac{J_K^3}{3!} \underbrace{(\boldsymbol{s}_i \cdot \boldsymbol{S}_i)(\boldsymbol{s}_j \cdot \boldsymbol{S}_j)(\boldsymbol{s}_k \cdot \boldsymbol{S}_k)}_{\triangle\text{-loop contraction}} \\ &= \frac{J_K^3}{2 \times 3!} E_{ijk} \boldsymbol{s}_i \cdot (\boldsymbol{s}_j \times \boldsymbol{s}_k) \quad . \end{aligned} \tag{2.5}$$

In the Kagomé case, the hexagons can also possess non-trivial fluxes. We can, however, restrict to the lowest order in J_K in the effective TRSB coupling for the conduction electrons, which corresponds to considering only the fluxes of the triangles.

The chiral interactions appearing in H_{chiral} have a six-fermion form. We can decouple it by introducing a novel HS transformation that involves triangular diagrams, as described in Appendix 7. We end up with an effective bilinear theory:

$$H_d = H_{d,0} + H_{d,1} \tag{2.6}$$

with

$$H_{d,1} = \textstyle\sum_{ij} (g\phi_j^* \phi_i d_i^\dagger d_j + \phi_i^* G_{\phi,ij}^{-1} \phi_j + h.c.) \quad . \tag{2.7}$$

Hence, the ϕ-fields are constrained by the condition that, if they are integrated out, we obtain the same chiral interaction terms at $\mathcal{O}(g^3)$ by computing the same triangle diagrams. We then replace $\phi_j^* \phi_i$ by its expectation value $G_{\phi,ij}$ and arrive at

$$H_{d,1} \to \sum_{ij} (g G_{\phi,ij} d_i^\dagger d_j + h.c.). \tag{2.8}$$

It turns out that $G_{\phi,ij} = e^{-iA_{ij}}$, and g can be identified as $g = J_K(|E_{ijk}|/2)^{1/3}$. Because the bosonic Gaussian integral has a minus sign relative to its fermionic counterpart, $G_{\phi,ij}$ carries the opposite flux pattern in order to produce the same H_{chiral}

when we integrate out the ϕ-fields. Physically, the flux (or chirality) pattern has the opposite sign to that of the CSL state, so that the antiferromagnetic Kondo coupling will lower the ground state energy. This effective Hamiltonian is adequate for qualitatively describing the AHE physics of our original Hamiltonian. Other non-chiral effective interactions would only renormalize the Fermi liquid parameters of the d-electrons for the P_S phase. We can then use the Streda formula [122, 22] to compute the AHE coefficient σ_{xy}: The involved quantities are the current operator of the conduction electrons $v_a(\mathbf{k}) = \partial_a H_d(\mathbf{k})$, the Berry curvature $\mathcal{F}_n^{xy}(\mathbf{k})$, and the Fermi function $f(\epsilon_n(\mathbf{k}))$ (see Appendix 7).

2.3.2 The Kondo screened P_L phase

In the P_L phase, the Kondo order parameter $\rho_{K,i}$ acquires a non-zero expectation value $\rho_K = \langle \rho_{K,i} \rangle$. There should still be an incoherent piece of the slave boson fields: $\rho_{K,i} = \rho_K + \pi_i'$. Moreover, we focus on the case where the chiral order survives in the P_L phase. By considering the same triangular diagrams now mediated by the incoherent part π_i', the fluctuations of the Kondo order parameter still mediate chiral interactions similarly as in the P_S phase, but with a reduced weight. However, there is no spectral sum rule for the π_i's to readily obtain this reduced weight. In Appendix 7, we use a slave rotor approach for the periodic Anderson model to determine this factor. The effective Hamiltonian of the d-electrons becomes

$$H_d = H_{d,0} + [1 - (4J_K/U)\rho_K^2] H_{d,1} \quad , \tag{2.9}$$

where U is the onsite Hubbard repulsion. We fix $U = 2W$, *i.e.* twice the d-electron's bandwidth throughout the calculations. Keeping only the ρ_K part of H_K leads to the following effective Hamiltonian:

$$H_{P_L} = \Psi^\dagger \begin{pmatrix} H_{\mathrm{CSL}} & -J_K \rho_K \mathcal{I} \\ -J_K \rho_K \mathcal{I} & H_d \end{pmatrix} \Psi \quad , \tag{2.10}$$

where $\mathcal{I}$ is an identity matrix, and $\Psi^\dagger = (f^\dagger, d^\dagger)$. We have dropped the spin index, as there are no longer the spin-flip terms. The Hamiltonian H_{P_L} is smoothly connected

with H_d at the QCP. We then compute σ_{xy} from the Streda formula Eq. A-22, noting that the current operators remains the same, i.e. $v_a(\mathbf{k}) = \partial_a H_d(\mathbf{k})$.

2.4 Anomalous Hall effect and its evolution across the Kondo-destruction quantum critical point

For the square lattice, we focus on the π-flux and the CSL states. For the π-flux phase, $H_{QSL} = H_{\pi-flux}$ is given by $A_{\mathbf{r}_i,\mathbf{r}_i+\hat{x}} = \pi/2$, $A_{\mathbf{r}_i,\mathbf{r}_i+\hat{y}} = -(-1)^{x_i}\pi/2$, $\rho_{\mathbf{r}_i,\mathbf{r}_i+\hat{x}+\hat{y}} = 0$, where $\mathbf{r}_i = (x_i, y_i)$, $\hat{x}$ ($\hat{y}$) is the unit vector along the $x(y)$-axis. For the CSL Hamiltonian, $H_{QSL} = H_{CSL}$ is derived from $H_{\pi-flux}$ with $\rho_{\mathbf{r}_i,\mathbf{r}_i+\hat{x}+\hat{y}} \neq 0$, $A_{\mathbf{r}_i,\mathbf{r}_i+\hat{x}+\hat{y}} = A_{\mathbf{r}_i+\hat{y},\mathbf{r}_i+\hat{x}} = (-1)^{x_i}\pi/2$, as illustrated in Fig. (2.1c).

In the Kagomé lattice, any state with triangle flux $\phi \neq 0, \pi$ breaks TRS. Here, we choose $\phi = -\frac{\pi}{2}$ such that the hexagon flux of $-2\phi = \pi$ preserves TRS. The $(-\frac{\pi}{2}, \pi)$ spinon flux state has three well-separated bands; the middle flat band is exactly at the Fermi energy, and the Chern numbers are $C_{lower} = -1$, $C_{middle} = 0$, $C_{upper} = +1$ [22]. The phase structure of the corresponding χ_{ij} fields is plotted in Fig. (2.1d).

The zero-field anomalous Hall conductivity σ_{xy} of the $J_1 - J_2 - J_K$ model is shown in Fig. (2.2(a)) for a representative parameters $n_d = 0.5$, $J_1 = t$ and that of the Kagomé lattice model in Fig (2.2(b)) for $J = t$, $n_d = 3/8$. Across the QCP, σ_{xy} is found continuous in the former, but jumps in the latter.

In order to understand the different behaviors, we show the Fermi surfaces (dashed lines) and the difference of band-summed Berry curvature $\Delta\Omega(\mathbf{k})$ (color map) between the P_S phase and the P_L phase right across the QCP in Fig. (2.3(a)) for the square lattice and (2.3(b)) for the Kagomé lattice (the actual $\Omega(\mathbf{k})$ is shown in Appendix 7). Here $\Delta\Omega(\mathbf{k}) = \Omega_{P_S}(\mathbf{k}) - \Omega_{P_L}(\mathbf{k})$ and $\Omega(\mathbf{k}) = \sum_n \mathcal{F}_n^{xy}(\mathbf{k}) f(\epsilon_n(\mathbf{k}))$. We find the Fermi surfaces remain continuous for the square lattice model. Both Fermi surfaces of the P_S and P_L phases are the black dashed line. However, for the Kagomé case, the Fermi surfaces show a jump. The Fermi surface of the P_S phase is the black dashed circle in the middle of the BZ which overlaps with the red, singular part of $\Delta\Omega(\mathbf{k})$. Those

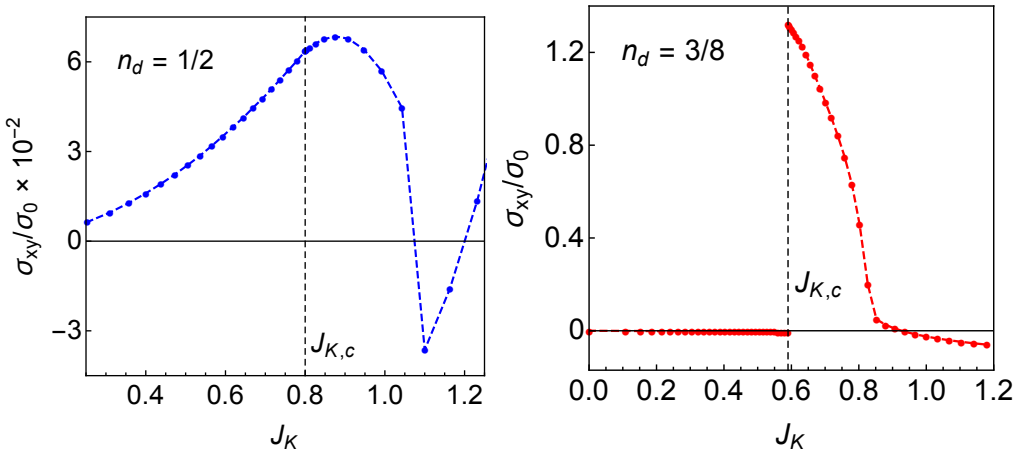

(a) (b)

Figure 2.2 : Zero field anomalous Hall conductance (σ_{xy}), normalized by the quantum conductance $\sigma_0 = e^2/h$, for $J_1 = t = 1,\ J_2/J_1 = 1/2,\ n_d = 0.5$ on a square lattice (a) and for $J = t,\ n_d = 3/8$ on a Kagomé lattice (b).

of the P_L phase are the blue dashed-line pockets at the edge of the BZ. These results reflect the number of sites per unit cell as well as the gapped/gapless nature of the spinon spectrum. However, $\Delta\Omega(\mathbf{k})$ is singular and concentrates near Fermi surfaces in both cases. This is because the onset of Kondo hybridization, which acts as a topological mass term in the large-N theory, generally reconstructs the wavefunctions in a singular fashion regardless of whether the Fermi surfaces jump or not.

To reconcile the notions of the singular wavefunction (or Berry curvature) with the continuous AHE, we note that σ_{xy} is intrinsically a Fermi surface property [25] (apart from the contributions of fully occupied bands). We can analytically show the following by computing the diagonal Berry's connection in the $\rho_K \to 0$ limit (see Appx. 7). When the Fermi surface is continuous, σ_{xy} must be continuous; here, the projected wavefunctions of the d-electron are continuous, and so are the Berry connections. By contrast, when the Fermi surface jumps, the projected wavefunctions completely reconstruct due to the existence of two non-commuting topological "masses": the Kondo screening and a non-zero jump of the spinon Lagrangian multiplier λ.

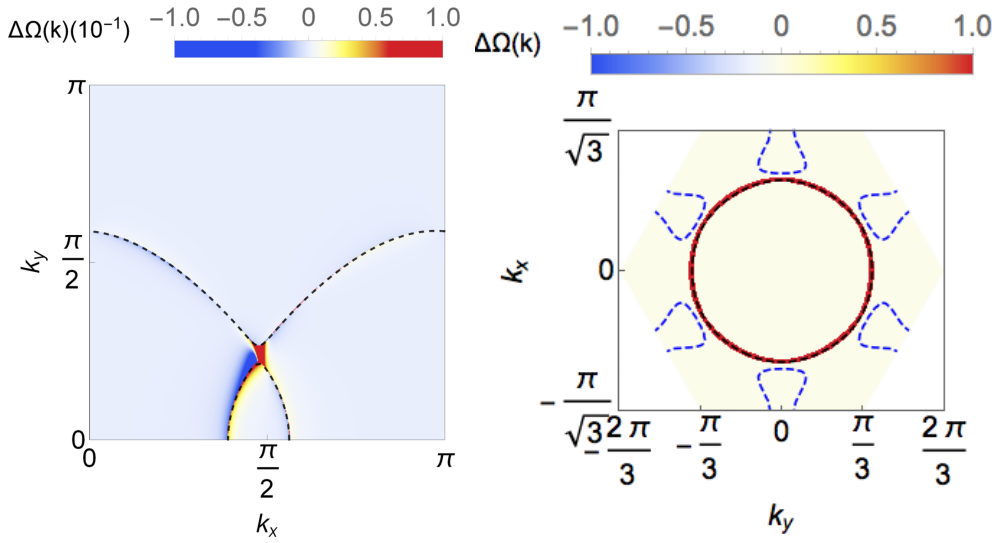

(a) (b)

Figure 2.3 : Fermi surfaces (dashed curves) and the difference in the band-summed Berry curvature distribution $\Delta\Omega(\mathbf{k})$ between the P_S phase and the P_L phase (color map) of the square lattice model (a) and the Kagomé lattice model (b).

2.5 Discussion

Energetic considerations show that the Kondo coupling favors gapless states (see Appendix. 7). For the pyrochlore lattice, the CSL state in the large-N limit is gapless [123], and is thus expected to have a similar sequence of quantum phase transitions involving the chiral state. The gapless nature raises the prospect of a sudden reconstruction of the Fermi surface across a Kondo-destruction QCP in the pyrochlore case and, by extension, a jump in the zero-field AHE, especially for a magnetic field along the [111] direction.

We expect the jump of the zero field AHE, σ_{xy}, to be robust against weak disorder. The AHE effect considered here is intrinsic, i.e. determined by the quasi-particle band structure. Scattering from weak non-magnetic impurities only yields a small (linear in disorder) correction [124]. Moreover, the Fermi-surface jump across a Kondo-destruction QCP has been evidenced to be robust against weak disorder [94, 17].

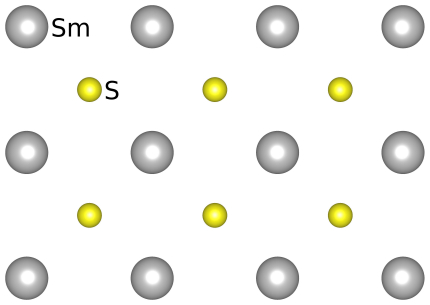

Figure 2.4 : Lattice plane of g-SmS.

Thus, our results can be tested in $Pr_2Ir_2O_7$, once a control parameter is identified to tune across the implicated zero-field QCP [110].

We note that the anomalous Hall conductance from the mechanism advanced here is quite large. Experiments in $Pr_2Ir_2O_7$ [101] find a large sheet σ_{xy} reaching about 0.7% of $\sigma_0 \equiv e^2/h$, a value which readily arise in our mechanism (Fig. 2.2(a)).

We have emphasized the role of the Kondo effect and its critical destruction. Future work should incorporate *ab initio* features, not only on the directional dependence in the pyrochlore lattice but also the effect of the *ab initio* electronic band structure and the non-Kramers nature of the ground-state crystal-field level of the Pr ions [125, 109]. However, we have derived our conclusions in geometrically frustrated Kondo systems and demonstrated the robustness of our results by connecting them with the evolution of the Fermi surfaces. Thus, we expect our results to remain qualitatively valid in the more realistic settings. For $Pr_2Ir_2O_7$, this is so given the substantial evidence for the role of the Kondo coupling such as the large entropy observed in the pertinent low-temperature regime [110]. It may also be instructive to explore related effects in other f-electron systems with geometrical frustration, such as UCu_5 under ambient conditions[126] and when suitably tuned through a QCP.

We close by proposing an engineered Kondo-insulator interface as a model material for the frustrated Kondo lattice Hamiltonian. The motivation for the proposed

setting comes from recent advances in the molecular beam epitaxy (MBE) of Kondo systems [127, 128]. As a promising candidate material we suggest the golden phase of SmS (g-SmS). In bulk samples this phase is stable under pressures between about 0.65 GPa [129] and 2 GPa [130]. As MBE thin-film the phase might be stabilized by lattice mismatch with an appropriate substrate. g-SmS crystallizes in a face-centered-cubic (fcc) structure of rock-salt (NaCl) type. A lattice plane is shown in Fig. (2.4). g-SmS shows characteristics of a Kondo insulating state in transport [131, 130], thermodynamics [132], and point contact spectroscopy [131]. From thermal expansion and heat capacity measurements the energy gap was estimated to be 90 K on the low-pressure side of the g-SmS phase [132]. At temperatures low compared to this scale, the proposed lattice plane could then serve as a setting to realize the frustrated $J_1 - J_2$ Kondo lattice and study the anomalous Hall effect.

Chapter 3

Weyl-Kondo semimetals in heavy fermion systems

3.1 Introduction

Strongly correlated electrons represent a vibrant field that continues to expand its horizon. In heavy fermion systems, strong correlations make their ground states highly tunable and give rise to a rich phase diagram that features antiferromagnetic order, Kondo-screened and other paramagnetic phases, and beyond-Landau quantum phase transitions [93, 5]. In the simplest cases, these systems can be considered in terms of the local moments originating from the f-electrons that Kondo couple to the spins of the conduction electrons. The interaction generates the Kondo spin-singlet ground state; the ensuing entanglement with the conduction electrons converts the local moments into quasiparticles that can hybridize with the conduction electrons. This leads to a metal with a large, strongly renormalized effective carrier mass, which is the hallmark of the heavy fermion system classification. The resulting state could be a heavy fermion metal or a Kondo insulator depending on whether the chemical potential lies within or falls between the hybridized bands [133, 17, 57]. Electronically intermediate between the two cases are heavy fermion semimetals [134, 135, 136, 137, 138, 139, 140, 141]. Several of these have a broken inversion symmetry, including $CeRu_4Sn_6$ [134, 135] and $Ce_3Bi_4Pd_3$ [137].

Semimetal systems are being theoretically studied in the noninteracting limit with spin-orbit coupling, which plays an essential role in obtaining topological phases of electronic matter [142, 143, 144, 145]. The Weyl semimetal in three dimensions (3D) was recently evidenced experimentally [146, 147, 148]. It possesses bulk excitations in the form of chiral fermions, with massless relativistic dispersions near pairs of

nodal points in the momentum space, as well as surface states in the form of Fermi arcs [86, 149, 150, 151]. Because both the bulk and surface states are gapless, one can expect that the Weyl semimetals are particularly susceptible to the influence of electron correlations. Moreover, strong correlations in non-perturbative regimes typically mix different degrees of freedom in generating low-energy physics; thus, in any strongly correlated Weyl semimetal, the low-energy electronic excitations are expected to involve degrees of freedoms such as spin moments, which may be harnessed for such purposes as information storage and retrieval.

In this chapter, we advance the discovery of a Weyl-Kondo semimetal state in a concrete microscopic model on a 3D noncentrosymmetric lattice. The focus of this chapter is to present the qualitative features of the Weyl-Kondo semimetal solution. Our work also illustrates a new approach towards constructing electronic topological states driven by strong correlations. Because this mechanism may have general relevance beyond the present context, we reserve a detailed exposition of the mechanism in the next chapter. This model contains the strongly correlated $4f$ electrons and a band of conduction *spd* electrons, respectively. It is realistic in that it captures the inversion-symmetry breaking and spin-orbital coupling in a tunable way. In the regime where the electron-electron repulsion is much larger than the width of the conduction-electron band, the interaction-induced renormalization factor can be very large. In addition, because the inversion-symmetry breaking term, spin-orbit coupling and other electronic couplings are renormalized in very different ways, it is *a priori* unclear whether any Weyl state can be realized in a robust way. Our work advances an affirmative answer in this well-defined microscopic model. Moreover, we demonstrate the key signatures of the Weyl-Kondo semimetal phase, which turn out to be realized in several new heavy fermion compounds.

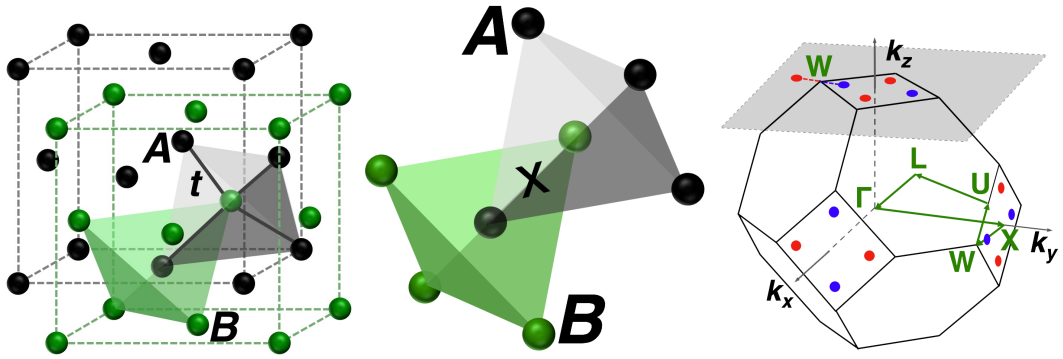

(a) (b) (c)

Figure 3.1 : **The 3D noncentrosymmetric lattice and associated Brillouin zone. (a),** Diamond lattice with hopping t and onsite energy $\pm m$ differentiating A, B sublattices. The solid lines connect nearest neighbors; **(b),** Interlocking tetrahedral sublattice cells illustrating how the distinction between the A and B sublattices (Zincblende structure) invalidates the inversion center lying on the point marked "X"; **(c),** The Brillouin zone (BZ) of the diamond lattice, with Weyl nodes shown in blue/red, and high symmetry contour used for Fig. 3.2 in green.

3.2 The periodic Anderson model in three dimensions

The Hamiltonian for the periodic Anderson model to be studied is

$$\mathcal{H} = \mathcal{H}_d + \mathcal{H}_{cd} + \mathcal{H}_c. \tag{3.1}$$

For a proof-of-concept demonstration, we consider a cubic system in which the breaking of inversion symmetry can be readily incorporated. This is a diamond lattice, which comprises two interpenetrating face-centered cubic lattices A and B (Fig. 3.1(a)). We have chosen this lattice because it is nonsymmorphic and, in the case of non-interacting electrons, band touching is enforced by its space group symmetry. The model contains d and c electrons, corresponding to the physical $4f$ and *spd* electrons, respectively. The first term, $\mathcal{H}_d$, describes the d electrons with an energy level E_d and a Coulomb repulsion U. The strongly correlated d-electrons are specified by

$$\mathcal{H}_d = E_d \sum_{i,\sigma} d^\dagger_{i\sigma} d_{i\sigma} + U \sum_i n^d_{i\uparrow} n^d_{i\downarrow}. \tag{3.2}$$

The coupling between the two species of electrons is described by a bare hybridization of strength V. The hybridization term is as follows:

$$\mathcal{H}_{cd} = V \sum_{i,\sigma} \left(d^{\dagger}_{i\sigma} c_{i\sigma} + \text{H.c.} \right). \tag{3.3}$$

In the above two equations, the site labeling i means $i = (\boldsymbol{r}, a)$, where $\boldsymbol{r}$ runs over the Bravais lattice of unit cells and a runs over the two sites, $a = A,\ B$, in the unit cell.

The conduction-electron Hamiltonian H_c realizes a modified Fu-Kane-Mele model [62]. Each unit cell has four species of conduction electrons, denoted by sublattices A and B and physical spins $\uparrow$ and $\downarrow$: $\Psi^T_{\mathbf{k}} = \begin{pmatrix} c_{\mathbf{k}\uparrow,A} & c_{\mathbf{k}\uparrow,B} & c_{\mathbf{k}\downarrow,A} & c_{\mathbf{k}\downarrow,B} \end{pmatrix}$. Its Hamiltonian is

$$\begin{aligned} \mathcal{H}_c = & \, t \sum_{\langle ij \rangle, \sigma} \left(c^{\dagger}_{i\sigma} c_{j\sigma} + \text{H.c.} \right) \\ & - \mu \sum_{i,\sigma} n^{c}_{i\sigma} \\ & + i\lambda \sum_{\langle\langle ij \rangle\rangle} \left[c^{\dagger}_{i\sigma} \left(\boldsymbol{\sigma} \cdot \mathbf{e}_{ij} \right) c_{j\sigma} - \text{H.c.} \right] \\ & + m \sum_{i,\sigma} (-1)^{i} c^{\dagger}_{i\sigma} c_{i\sigma}. \end{aligned} \tag{3.4}$$

There is a nearest-neighbor hopping t (chosen as our energy unit), and a Dresselhaus-type spin-orbit coupling of strength λ. The broken inversion symmetry, Fig. 3.1(b), is captured by an onsite potential m that staggers between the A and B sublattices [87, 145]. The band basis is arrived at by applying a canonical transformation on H_c written in the sublattice and spin basis. It corresponds to a pseudospin basis [87], defined by the eigenstates $|\pm D\rangle$.

The conduction electron Hamiltonian can be expressed as $H_c = \sum_{\mathbf{k}} \Psi^{\dagger}_{\mathbf{k}}\ h_{\mathbf{k}}\ \Psi_{\mathbf{k}}$, and

$$h_{\mathbf{k}} = \quad \sigma_0 \left(u_1(\mathbf{k}) \tau_x + u_2(\mathbf{k}) \tau_y + m \tau_z \right) + \lambda \left(\mathbf{D}(\mathbf{k}) \cdot \boldsymbol{\sigma} \right) \tau_z. \tag{3.5}$$

Here, $\boldsymbol{\sigma} = (\sigma_x, \sigma_y, \sigma_z)$ and $\boldsymbol{\tau} = (\tau_x, \tau_y, \tau_z)$ are the Pauli matrices acting on the spin and sublattice spaces, respectively, and σ_0 is the identity matrix. In the first term,

$u_1(\mathbf{k})$ and $u_2(\mathbf{k})$ are determined by the conduction electron hopping, $t_{\langle ij\rangle} = t$ between nearest-neighbor sites ($\langle ij\rangle$). The second term specifies a Dresselhaus-type spin-orbit coupling between the second-nearest-neighbor sites ($\langle\langle ij\rangle\rangle$), which is of strength λ and involves vector $\mathbf{D}(\mathbf{k}) = \Big(D_x(\mathbf{k}), D_y(\mathbf{k}), D_z(\mathbf{k})\Big)$. Specifically,

$$u_1(\mathbf{k}) = t\left(1 + \sum_{n=1}^{3} \cos(\mathbf{k}\cdot\mathbf{a}_n)\right), \tag{3.6}$$

$$u_2(\mathbf{k}) = t\sum_{n=1}^{3} \sin(\mathbf{k}\cdot\mathbf{a}_n), \tag{3.7}$$

$$\begin{aligned} D_x(\mathbf{k}) = {} & \sin(\mathbf{k}\cdot\mathbf{a}_2) - \sin(\mathbf{k}\cdot\mathbf{a}_3) - \sin(\mathbf{k}\cdot(\mathbf{a}_2 - \mathbf{a}_1)) \\ & + \sin(\mathbf{k}\cdot(\mathbf{a}_3 - \mathbf{a}_1)), \end{aligned} \tag{3.8}$$

and $D_x,\ D_y$ are obtained by permuting the fcc primitive lattice vectors $\mathbf{a}_n$. The canonical (unitary) transformation, $\breve{\Psi}_{\mathbf{k}} = S_\sigma^\dagger \Psi_{\mathbf{k}}$, leads to

$$H_c = \sum_{\mathbf{k}} \breve{\Psi}_{\mathbf{k}}^\dagger \begin{pmatrix} h_{\mathbf{k}+} & 0 \\ 0 & h_{\mathbf{k}-} \end{pmatrix} \breve{\Psi}_{\mathbf{k}}, \tag{3.9}$$

$$h_{\mathbf{k}\pm} = u_1(\mathbf{k})\tau_x + u_2(\mathbf{k})\tau_y + (m \pm \lambda D(\mathbf{k}))\tau_z. \tag{3.10}$$

We have used a pseudospin basis [87], defined by the eigenstates $|\pm D\rangle$ with eigenvalues

$$\frac{\mathbf{D}\cdot\boldsymbol{\sigma}}{D}|\pm D\rangle = \pm|\pm D\rangle \tag{3.11}$$

where $D(\mathbf{k})$ is written out

$$D(\mathbf{k}) \equiv |\boldsymbol{D}(\mathbf{k})| = \sqrt{D_x(\mathbf{k})^2 + D_y(\mathbf{k})^2 + D_z(\mathbf{k})^2}. \tag{3.12}$$

The eigenenergies of the $|\pm D\rangle$ sectors are simply obtained to be

$$\varepsilon_{\pm D}^{\tau} = \tau\sqrt{u_1(\mathbf{k})^2 + u_2(\mathbf{k})^2 + (m \pm \lambda D(\mathbf{k}))^2} \tag{3.13}$$

where $\tau = (+,-)$. We use this transformation on the full Anderson model in the strong coupling limit, at the saddle point level where the Lagrange multiplier ℓ_i, which enforces the local constraint $b_i^\dagger b_i + \sum_\sigma f_{i\sigma}^\dagger f_{i\sigma} = 1$, takes a uniform value, ℓ.

This corresponds to $\breve{\Xi}_{\mathbf{k}} = S_\sigma^\dagger \Xi_{\mathbf{k}}$. Anticipating the separability of the $|\pm D\rangle$ sectors by specifying $\breve{\Psi}_{\mathbf{k}}^T = \left(\breve{\psi}_{\mathbf{k}+}^T, \breve{\psi}_{\mathbf{k}-}^T\right)$, $\breve{\Xi}_{\mathbf{k}}^T = \left(\breve{\xi}_{\mathbf{k}+}^T, \breve{\xi}_{\mathbf{k}-}^T\right)$, where $\breve{\psi}_{\mathbf{k}\pm}^T = \left(\breve{\psi}_{\mathbf{k}\pm,A}, \breve{\psi}_{\mathbf{k}\pm,B}\right)$ and $\breve{\xi}_{\mathbf{k}\pm}^T = \left(\breve{\xi}_{\mathbf{k}\pm,A}, \breve{\xi}_{\mathbf{k}\pm,B}\right)$, we obtain the strong coupling Hamiltonian

$$H^s = \sum_{\mathbf{k},a=\pm} \begin{pmatrix} \breve{\psi}_{\mathbf{k}a}^\dagger & \breve{\xi}_{\mathbf{k}a}^\dagger \end{pmatrix} \begin{pmatrix} h_{\mathbf{k}a} - \mu \mathbb{1}_2 & rV\mathbb{1}_2 \\ rV\mathbb{1}_2 & (E_d + \ell)\mathbb{1}_2 \end{pmatrix} \begin{pmatrix} \breve{\psi}_{\mathbf{k}a} \\ \breve{\xi}_{\mathbf{k}a} \end{pmatrix}, \tag{3.14}$$

which separates as $H^s = \mathcal{H}_+^s + \mathcal{H}_-^s$. We obtain the full spectra of the eight hybridized bands,

$$\mathcal{E}_{\pm D}^{(\tau,\alpha)}(\mathbf{k}) = \frac{1}{2}\left[E_s + \tilde{\varepsilon}_{\pm D}^\tau + \alpha\sqrt{\left(E_s - \tilde{\varepsilon}_{\pm D}^\tau\right)^2 + 4V_s^2}\right], \tag{3.15}$$

where $\alpha = (+,-)$ indexes the upper/lower quartet of bands, $\tilde{\varepsilon}_{\pm D}^\tau = \varepsilon_{\pm D}^\tau - \mu$, and $(E_s,\ V_s) = (E_d + \ell, rV)$. In Appendices A6-ch:app-prb, we prove that the $|+D\rangle$ sector is always gapped, whereas the $|-D\rangle$ sector allows Weyl nodes when $0 < \frac{m}{4|\lambda|} < 1$, and determine $\mu = -V_s^2/E_s$ fixes the Fermi energy at the Weyl nodes at the 1/4-filling.

To determine $r,\ \ell$, H^s must be solved self-consistently from the saddle-point equations

$$\begin{aligned} &\frac{1}{2N_u}\sum_{\mathbf{k},a=\pm}\left\langle \breve{\xi}_{\mathbf{k}a}^\dagger \breve{\xi}_{\mathbf{k}a}\right\rangle + r^2 = 1, \\ &\frac{V}{4N_u}\sum_{\mathbf{k},a=\pm}\left[\left\langle \breve{\psi}_{\mathbf{k}a}^\dagger \breve{\xi}_{\mathbf{k}a}\right\rangle + \text{H.c.}\right] + r\ell = 0, \end{aligned} \tag{3.16}$$

where N_u is the number of the unit cell. The equations are solved on a $64 \times 64 \times 64$ cell of the diamond lattice, with error $\epsilon \leq \mathcal{O}(10^{-5})$.

We consider the regime with the onsite interaction U being large compared to the bare c-electron bandwidth ($U/t \to \infty$). We approach the prohibition of d fermion double occupancy by an auxiliary-particle method [152]: $d_{i\sigma}^\dagger = f_{i\sigma}^\dagger b_i$. Here, the $f_{i\sigma}^\dagger$ (b_i) are fermionic (bosonic) operators, which satisfy a constraint that is enforced by a Lagrange multiplier ℓ. This approach leads to a set of saddle-point equations, where b_i condenses to a value r, which yields an effective hybridization between the f-quasiparticles and the conduction c-electrons. The details of the method are described

in the Materials and Methods section. To be definite, we consider the case that the d-electron level lies below the conduction-electron band. We analyze the problem at a quarter filling, corresponding to one electron per site.

The corresponding quasiparticle band structure is shown in Fig. 3.2. Nodal points exist at the Fermi energy, in the bands for which the pseudospin (defined earlier) has an eigenvalue $-D$. They occur at the wave vectors $\mathbf{k}_W$, determined in terms of the hybridized bands,

$$\begin{aligned} \mathcal{E}_{-D}^{(+,+)}(\mathbf{k}_W) &= \mathcal{E}_{-D}^{(-,+)}(\mathbf{k}_W), \\ \mathcal{E}_{-D}^{(+,-)}(\mathbf{k}_W) &= \mathcal{E}_{-D}^{(-,-)}(\mathbf{k}_W), \end{aligned} \tag{3.17}$$

for the upper and lower branches, respectively. The Weyl nodes appear along the Z lines (lines connecting the X and W points) in the three planes of the BZ as illustrated in Fig. 3.1(c). The locations of the Weyl points being on the Z lines are specific to the zinc blende lattice. For other types of lattices, the Weyl nodes may occur away from the high symmetry parts of the Brillouin zone. We stress a key feature of the nodal excitations, namely they develop out of the Kondo effect: the bands near the Fermi energy have a width much reduced from the noninteracting value; the reduction factor corresponds to r^2 (the ratio of the Kondo energy to the bare width of the conduction electron band), which is about 0.067 in the case shown in Fig. 3.2. We remark that in the absence of hybridization between the f- and conduction electrons, the ground state would be an insulator instead of a semimetal: the f-electrons would be half-filled and form a Mott insulator, while the conduction electrons would be empty, forming a band insulator.

To demonstrate the monopole flux structure of the Weyl nodes, we calculate the Berry curvature in the strong coupling regime. We show the results at the $k_z = 2\pi$ boundary of the 3D BZ, in the grey plane of Fig. 3.1(c) whose dispersion is shown in Fig. 3.3(b). In Fig. 3.3(b), the arrows represent the field's unit-length 2D projection onto the $k_x k_y$-plane, $\hat{\Omega}(k_x, k_y, 2\pi) = |\vec{\Omega}(k_x, k_y, 2\pi)|^{-1} \Big(\Omega_{yz}(k_x, k_y, 2\pi),\ \Omega_{zx}(k_x, k_y, 2\pi)\Big)$.

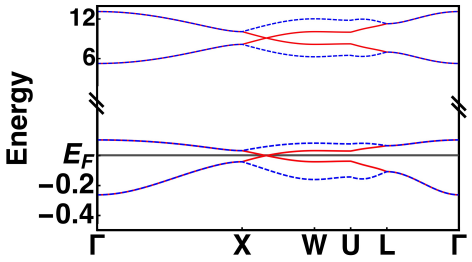

Figure 3.2 : **Energy dispersion of the bulk electronic states.** Shown here is the energy *vs.* wavevector **k** along a high symmetry path in the BZ, defined in Fig. 3.1(c). The bottom four bands near E_F show a strong reduction in the bandwidth., The bare parameters are $(t, \lambda, m, E_d, V) = (1, 0.5, 1, -6, 6.6)$. In the self-consistent solution, $r \simeq 0.259$ and $\ell \simeq 6.334$.

The Weyl node locations (blue/red circles) are clearly indicated by the arrows flowing in or out, representing negative or positive monopole "charge."

We next analyze the surface states. Focusing on the (001) surface, we find the following energy dispersion for the surface states:

$$\mathfrak{E}(k_x, k_y) = -2\sin\left(\frac{k_x}{4}\right)\sin\left(\frac{k_y}{4}\right) + \frac{V_s^2 + (E_s)^2}{2E_s} - \sqrt{\left(2\sin\left(\frac{k_x}{4}\right)\sin\left(\frac{k_y}{4}\right) - \frac{V_s^2 - (E_s)^2}{2E_s}\right)^2 + V_s^2}, \tag{3.18}$$

where we define the parameters $(V_s, E_s, \mu_s) = (rV, E_d + \ell, -(rV)^2/(E_d + \ell))$. (For the derivation, see Supplementary Information.) In Figs. 3.4(a)-3.4(b), we show the energy dispersion along a high symmetry path in the **k**-space. The solid lines represent the surface states, and the dashed lines show where they merge with the bulk states and can no longer be sharply distinguished. The surface electron spectrum has a width that is similarly narrow as the bulk electron band (compare Fig. 3.4(b) with Fig. 3.3(a)), implying that the surface states also come from the Kondo effect. The surface Fermi arcs (where $\mathfrak{E}(k_x, k_y) = 0$) connect the Weyl nodes along $k_x = 0$ and $k_y = 0$, separating the positive and negative energy surface patches, marked by the solid black lines in Fig. 3.4(a).

As is typical for strongly correlated systems, the most dominant interactions in

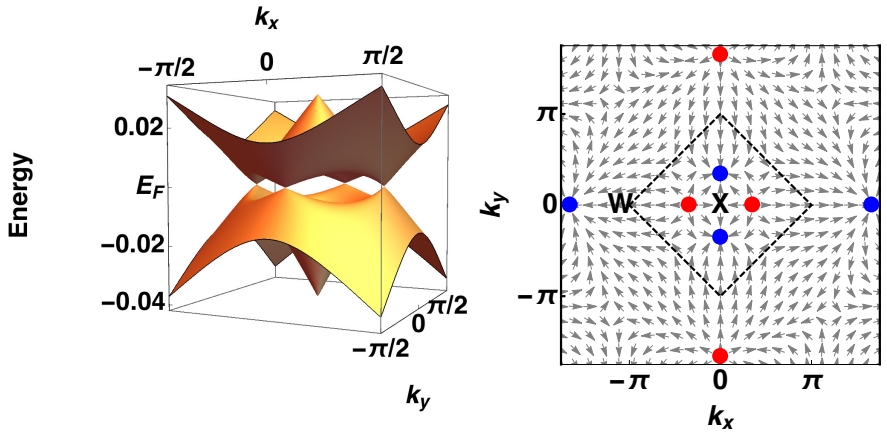

(a) (b)

Figure 3.3 : **Characterization of the Weyl nodes.** The plots are in the (k_x, k_y)-plane of the four Weyl nodes at $k_z = 2\pi$ (gray plane in Fig. 3.1(c)). **(a),** Energy dispersion, showing the band degeneracies at the Weyl node points and a strong reduction of the bandwidth; **(b),** The distribution of the Berry curvature field. The bare parameters are the same as in Fig. 3.2.

heavy fermion systems are onsite, making it important to study them in lattice models (as opposed to the continuum limit). Our explicit calculations have been possible using a well-defined model on a diamond lattice that permits inversion-symmetry breaking. Nonetheless, we expect our conclusion to qualitatively apply to other non-centrosymmetric 3D systems. Finally, the WKSM is expected to survive the effect of a time-reversal symmetry breaking term, such as a magnetic field; this is illustrated in the Supplementary Information.

3.3 Discussion

We now turn to the implications of our results for heavy fermion semimetals. The entropy from the bulk Weyl nodes will be dictated by the velocity v^*, and the corresponding specific heat per unit volume has the following form (see Supplementary

Information):

$$c_v \sim (k_B T/\hbar v^*)^3 k_B \tag{3.19}$$

The utility of thermodynamical quantities as a key signature reflects an important distinction of the WKSM from weakly correlated Weyl semimetals. The Kondo temperature of heavy fermion systems is usually considerably smaller than the Debye temperature. This is to be contrasted with the weakly correlated systems, in which the bandwidth of the conduction electrons is typically much larger than the Debye temperature. Therefore, in a WKSM, the nodal contributions to the entropy would dominate over the phonon component. The corresponding form of entropy also implies that the nodal excitations will have large contributions to the thermopower.

Eq. (3.19) can be readily tested, given that an important feature of the overall heavy fermion materials class is the existence of a considerable number of semimetal compounds [17]. A noncentrosymmetric heavy-fermion system $Ce_3Bi_4Pd_3$ has recently been discovered to display semimetal behavior based on transport measurements, and its specific heat is well described in terms of Eq. (3.19) [Ref. [137]]. A fit in terms of our theoretical expression Eq. (S29) (Supplementary Information) reveals an effective velocity, v^*, that is three orders of magnitude smaller than that expected for weakly correlated systems, reflecting the reduction in the energy scale – the Kondo temperature for $Ce_3Bi_4Pd_3$ – from the bandwidth of the latter by a similar order of magnitude [137]. This analysis provides strong evidence that $Ce_3Bi_4Pd_3$ is a candidate WKSM system with strongly-correlated Weyl nodes, and provides the motivation for further studies on such quantities as magnetotransport and high-resolution angle-resolved photoemission spectroscopy (ARPES) in this system. More recently, Eq. (3.19) has been used to fit the specific heat of another heavy fermion system, YbPtBi, suggesting it be another candidate WKSM system [153].

Our theoretical results provide guidance in the search for Weyl semimetals in other heavy fermion systems. For instance, in the $4f$-based system CeSb, Weyl physics has been suggested based on magnetotransport measurements [154, 155]. Even though

any nodes in this system are likely to be away from the Fermi energy, the fact that its energy scales are low makes it likely that they can readily be tuned towards the Fermi energy by pressure or chemical doping, and we propose specific heat measurements and our (3.19) as a means of ascertaining the role of the $4f$-electrons in this system. In addition, the noncentrosymmetric $CeRu_4Sn_6$ also displays semimetal properties [134] and has been discussed as a potential topological system [135]. Its electronic structure has been studied by *ab initio* calculations combined with dynamical mean field theory (DMFT) [134, 156] or the Gutzwiller projection method [157]. While the two types of calculations disagree on the low-energy dispersion and the latter study does not appear to capture the strong renormalizations expected in a Kondo system, the existence of linearly-dispersing nodes and their Weyl nature have been suggested in the latter study. The low-temperature specific heat in single crystalline $CeRu_4Sn_6$ [158] implies the importance of the $4f$-electrons to the low-energy physics but does not appear to have the form of (3.19). Our theoretical results suggest that further thermodynamic and thermoelectrical studies will be instructive in ascertaining the potential WKSM nature of $CeRu_4Sn_6$.

3.4 Conclusions

We close with several observations. First, we have focused on a model defined on an nonsymmorphic diamond lattice, which is representative of the cases in which the crystallographic space group symmetry and filling enforce a semimetal state for noninteracting electrons [84, 86]. Our study here demonstrates that for Kondo systems defined on such a lattice and in the presence of inversion-symmetry breaking, the Weyl-Kondo semimetal phase arises in a robust way. On the other hand, for noninteracting systems in 3D a Dirac semimetal can also arise at the phase transition between a topological and a normal insulator. It will therefore be instructive to search for Weyl-Kondo semimetal phase at 3D strongly-corrlelated f-electron systems, at the topological phase transitions in Kondo systems, which we leave for future studies.

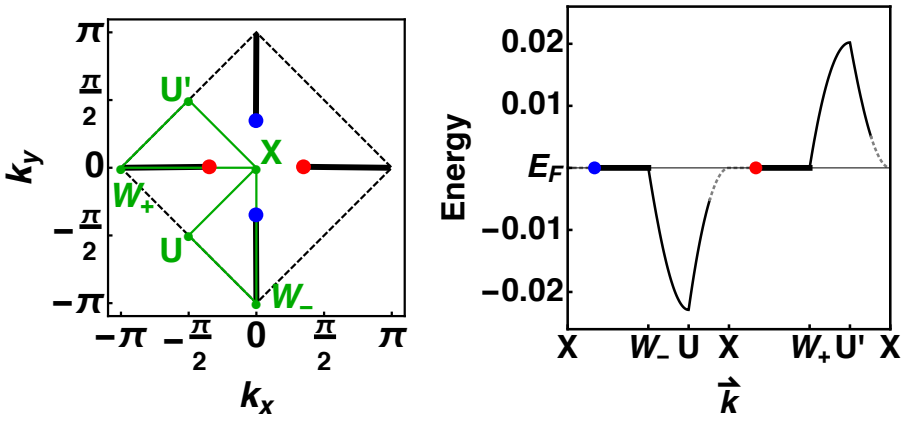

(a) (b)

Figure 3.4 : **Energy dispersion of the surface electronic states.** The spectrum shows the (anti-)Weyl nodes marked with blue (red). The solid black lines connecting the nodes represent Fermi arcs and black dashed lines represent the BZ around the X point. **(a),** High-symmetry **k**-space contour taken on the BZ boundary at $k_z = 2\pi$; **(b),** Energy dispersion of the surface state along the path specified in (a); the grey dotted line denotes the decay of the surface states into the bulk states. The parameters are the same as in Fig. 3.2.

Second, our work provides a proof of principle demonstration for the emergence of Weyl Kondo semimetal state in a Kondo lattice with inversion symmetry breaking. This makes it likely that Kondo lattices in 3D with other crystallographic symmetries but with the breaking of inversion symmetry will host a WKSM phase. The candidate WKSM material $Ce_3Bi_4Pd_3$ has a nonsymmorphic space group (220), and its Kondo-driven Weyl nodes may very well be enforced by its crystallographic symmetry and electron filling. Our findings here motivates further studies that incorporates the realistic electronic structure of $Ce_3Bi_4Pd_3$.

Third, in the WKSM state advanced here, the electron correlations produce a zeroth-order effect given that the localized moments of the $4f$-electrons underlie the Weyl excitations. Correspondingly, the renormalization factors are extremely large, typically on the order of $10^2 - 10^3$. This distinguishes the WKSM from other types of interacting Weyl semimetals discussed previously. The large renormalization factor

is responsible for the possibility of using thermodynamics to probe the Weyl nodes. Our work also sets the stage for calculations of additional signature properties for the Weyl physics, such as the optical conductivity and related dynamical quantities.

Finally, the emergence of a WKSM makes it natural for quantum phase transitions in heavy fermion systems from such a topological semimetal to magnetically ordered and other correlated paramagnetic states. Moreover, the existence of Weyl nodes also enhances the effect of long-range Coulomb interactions. While the density fluctuations of the f-electrons are strongly suppressed in the local-moment regime, it still will be instructive to explore additional nearby phases such as charge-density-wave order [159]; other type of long-range interactions could produce topologically-nontrivial Mott insulators [160]. As such, the study of WKSM and related semimetals promises to shed new light on the global phase diagram of quantum critical heavy fermion systems [17] and other strongly correlated materials [161].

In summary, we have demonstrated an emergent Weyl-Kondo semimetal phase in a model of heavy fermion systems with broken inversion symmetry, and have determined the surface electronic spectra which reveal Fermi arcs. The nodal excitations of the WKSM phase develop out of the Kondo effect. This leads to unique experimental signatures for such a phase, which are realized in noncentrosymmetric heavy fermion systems. Our results are expected to guide the experimental search for f-electron-based Weyl semimetals. In general, they open the door for studying topological semimetals in the overall context of quantum phases and their transitions in strongly correlated electron systems and, conversely, broaden the reach of strongly correlated gapless and quantum critical states of matter.

Chapter 4

Weyl-Kondo semimetals in nonsymmorphic systems

4.1 Introduction

In the previous chapter, I described the emergence of a Weyl-Kondo semimetal (WKSM) phase in a Kondo lattice model; such a phase was contemporaneously advanced in experimental studies [137, 162]. My theoretical work considered a Kondo lattice model, which is time-reversal invariant but inversion-symmetry breaking. The defining characteristics of the Weyl-Kondo semimetal include linearly-dispersing Weyl nodal excitations with highly reduced velocity and Weyl nodes being pinned to the Fermi energy.

As alluded to in the previous chapter, we show in some detail the role of nonsymmorphic space group symmetry cooperates with the strong correlation effects in producing these properties. In this chapter, I will expound on this mechanism and suggests that it represents a general framework to search for other types of correlation-driven topological states. As already introduced, we consider a periodic Anderson/Kondo model on a diamond lattice, with inversion symmetry broken by a staggered potential, at quarter filling [117]. Focusing on the limit of large on-site Coulomb repulsion, the model is equivalent to a Kondo lattice. As I will describe in detail, in the absence of Kondo coupling, the nonsymmorphic space group symmetry generates Weyl nodes that are located far away from the Fermi energy, and the ground state is topologically trivial. Because of the Kondo effect, strongly renormalized quasiparticles are produced near the Fermi energy. When this happens, the space-group symmetry in turn ensures that the Weyl nodes develop precisely at the Fermi energy; this makes the Weyl nodal excitations to be long-lived and, hence,

well-defined, even in the present strongly interacting setting. In addition, the renormalized nodal velocity is smaller than the usual non-interacting value by the ratio of the Kondo temperature to the bare conduction-electron bandwidth, which can be as large as three orders of magnitude. We will also analyze further the effect of a tilting potential [162] to the Weyl-Kondo solution itself and the Berry curvature distribution. All these properties are important in giving rise to new signatures of the Weyl-Kondo semimetal not only for thermodynamic [117, 137] properties discussed in the previous chapter, but also for transport properties [162]. In addition, we will discuss how these results enrich the global phase diagram of heavy fermion metals. This enrichment captures the role of spin-orbit coupling in the interplay between competing phases, all of which develop out of the underlying spin degrees of freedom of the $4f$ electrons.

To set the stage for our analysis about how the space-group symmetry interplays with strong correlations, we start by briefly outlining the role of space-group symmetry in the noninteracting case.

4.1.1 Role of nonsymmorphic space group symmetry and protection of topological semimetal phases

We focus our discussion on three dimensional (3D) crystals. In topological semimetals, the bulk already has a gapless excitation spectrum. This is to be contrasted with topological insulators, in which the bulk excitations are fully gapped and only the surface states are gapless. Both of these topological phases must have band inversion, a reordering of conduction and valence bands which allows the topological insulator surface states to connect the conduction and valence bands. In three dimensions, a quadratic Hamiltonian can be classified into a topological equivalence class depending on its nonspatial symmetries: time-reversal symmetry (TRS), particle-hole symmetry, and chiral symmetry. This is commonly known as the tenfold way, which can be applied to topological insulators and topological semimetals, and can accommo-

date spatial symmetries as well [51]. More specifically to Weyl semimetals, these are characterized by energy levels that meet in pairs of twofold degenerate points in momentum space as a result of tuning Hamiltonian parameters. Without other symmetries in the system, this requires tuning three parameters to achieve degeneracy, but space group symmetries may protect the degeneracies [86]. In the efforts to identify topological materials, several studies have applied symmetry classification criteria to space groups [163, 78, 164] and more specifically to particular lattice realizations, [92, 91] as well as considered the fillings at which nonsymmorphic symmetries will enforce gapless phases [90].

To obtain such degeneracy, a mechanism of band inversion is a necessary but insufficient ingredient. Band inversion can occur by lattice strain, scalar relativistic effects, or spin-orbit coupling (SOC) [81, 82, 83]. Given the crucial role of the SOC, the search for topological materials tends to focus on systems that are based on heavy elements with large SOC. Conveniently, the lanthanides and actinides where the f-orbital elements as well as the often-involved heavy elements (e.g., Bi) associated with heavy fermion materials provides substantial SOC.

We are interested in topological semimetals in 3D crystals with SOC and additional space-group symmetries that can protect nodal band crossings. It turns out that many nonsymmorphic space groups can support four-dimensional irreducible representations on the zone boundaries, which produce robust symmetry protected Dirac semimetal phases, provided they do not lie along threefold or sixfold rotation axes [86, 84]. A nonsymmorphic symmetry is a space group operation $\{\mathcal{O}|\mathbf{t}\}$ which combines a spatial point-group operation (or nonspatial operation) $\mathcal{O}$ with a *partial* (non-primitive) lattice translation vector $\mathbf{t}$. Spatial symmetries are group operations that rotate and reflect different lattice sites onto one another, such as an n-fold rotation about the ith axis C_{ni}, or a reflection about the ab plane with normal vector $\hat{c}$, m_c. Respectively, the corresponding nonsymmorphic transformations are called screw operations ($\{C_{ni}|\mathbf{t}\}$ = rotation + fractional $\mathbf{t}$) and glide operations ($\{m_c|\mathbf{t}\}$ =

reflection + fractional $\mathbf{t}$). Since multiple fractional translations are needed to traverse the unit cell, it is enlarged in real space, which causes the Brillouin zone (BZ) to fold. This creates a new Brillouin zone boundary (BZB) where any bands that intersect it are sharply reflected back into the BZ, causing a degeneracy at the BZB. For these reasons, nonsymmorphic space groups with SOC generically produce Dirac nodal band touching points or lines of degeneracy. The glide symmetry is familiar to the strongly correlated electron community of iron pnictides; there, the symmetry implies that the eigenstates come in (glide even and odd) pairs and, as a result, gives rise to an extra degeneracy at the boundary of the BZ associated with the physical two-iron unit cell [165].

With the nonsymmorphic symmetry-enforced Dirac semimetal as a starting point, a Weyl semimetal phase can arise from breaking TRS or inversion symmetry (IS) [86]. Without the protection of space-group symmetry, one would have to resort to IS breaking (ISB) systems tuned to within a band inversion transition between a trivial band insulator and a topological insulator [78, 166]. Bands that invert are allowed to cross because (1) the bands have different irreducible representations, such as the odd-even parity in s-f coupling; (2) bands of the same irreducible representation may have wavefunctions that differ by a Berry phase [51, 167]. Otherwise, the noncrossing theorem requires that the bands hybridize to open a topologically trivial gap at a generic point in the BZ. Thus a robust procedure is to search for space groups that anchor IS breaking or are also noncentrosymmetric, and can realize an even filling factor that is both gapless and has zero enclosed Fermi surface volume.

4.1.2 Topological states driven by strong correlations

Given all these considerations, a topological state driven by the Kondo effect arises if one first realizes a topologically trivial ground state without the Kondo effect, and when the Kondo effect is turned on, produces a topologically non-trivial phase. Our model has a solution that corresponds to such a Kondo-driven phase. We will show

that the result is robust to changes in parameters. This is because our Hamiltonian has the required crystal and local symmetries, and fulfills group-theoretical filling constraints that achieve topological semimetal phases in response to the Kondo effect. Therefore, our model illustrates that strong correlations help hone in on nontrivial topological phases in the vast multidimensional parameter space of the strong correlation global phase diagram in the presence of a large SOC. In this sense, a design principle follows from our work (as well as from experiments [137, 162]), namely to search for topological semimetals driven by strong correlations by focusing on strongly correlated semimetals with a nonsymmorphic space group and broken inversion symmetry.

4.2 Model and solution method

The model Hamiltonian is Eqs. 3.1-3.4, and we use the treatment of Section. 3.2 to render it analytically tractable, then solve the saddle point equations that correspond to the Kondo limit. Here the auxiliary boson procedure is described in more depth.

We focus on the case of quarter filling, which corresponds to total electron count of 1 per site. Explicitly we impose the condition

$$n_d + n_c = 1, \tag{4.1}$$

where,

$$n_d = \frac{1}{N_{\text{site}}} \sum_{i,\sigma} d^\dagger_{i\sigma} d_{i\sigma}, \tag{4.2}$$

$$n_c = \frac{1}{N_{\text{site}}} \sum_{i,\sigma} c^\dagger_{i\sigma} c_{i\sigma}, \tag{4.3}$$

with N_{site} counting the total number of sites in the lattice.

The interaction U term is an obstruction to obtaining the eigenstates. However, in the strong coupling limit of $U \to \infty$, one can use the auxiliary boson method [1] to treat the Coulomb term by considering it's large limit consequence, which is to

only allow density configurations of single particle-per-site occupation and empty occupancy. Thus the localized species acquires a boson as $d^\dagger_{i\sigma} = b_i f^\dagger_{i\sigma}$, which is, at the saddle-point level, averaged over the unit cell as $b_i \to \langle b_i \rangle = r$, where $0 < r < 1$. This necessitates including a Lagrange multiplier ℓ which parameterizes a constraint equation term introduced into the large U Hamiltonian as $\mathcal{H}_s = \mathcal{H} + \mathcal{H}_\ell$,

$$\mathcal{H}_\ell = \ell \left(\sum_{i,\sigma} f^\dagger_{i\sigma} f_{i\sigma} + r^2 - 1 \right), \tag{4.4}$$

and renormalizing the hybridization as $V \to \tilde{V} = rV$. Put together, this gives the strong coupling Hamiltonian $\mathcal{H}_s$.

The parameters $\mathbf{x} = (\mu, r, \ell)$ are obtained by solving the set of saddle point equations $\frac{\delta \mathcal{H}_s}{\delta x_i} = 0$ self consistently. The parameter ℓ renormalizes the localized electron's energy level to $E_d \to \tilde{E}_d = E_d + \ell$, which in practice is close to E_F (we define $E_F = 0$).

We eliminated the need to numerically solve for μ by finding the analytical solutions to nodal points in the Brillouin zone (see Appendix C1). The key step to solving for the eigenenergies is to find a suitable basis that renders the Hamiltonian separable. In Ref. [117], we performed the canonical (unitary) transformation on Eq. (3.4), which renders the conduction electron part block diagonal in the $|\pm D\rangle$ basis.

Based on previous studies, [87, 117] we know that the Weyl nodes only emerge in the $|-D\rangle$ sector corresponding to $h_{\mathbf{k}-}$. Since the bands have a definite ordering in terms of energy (see Appendix C1), we find the nodal band touchings occur only between particular bands (see Sec. 4.3.2).

With the number of particles per-site-per-spin (or simply fractional filling) of all fermions being $n_c + n_d = 1$ and since the localized electrons' filling was fixed at $n_f = 1 - r^2$, this implies that the conduction electron density is $n_c = r^2$ and thus small.

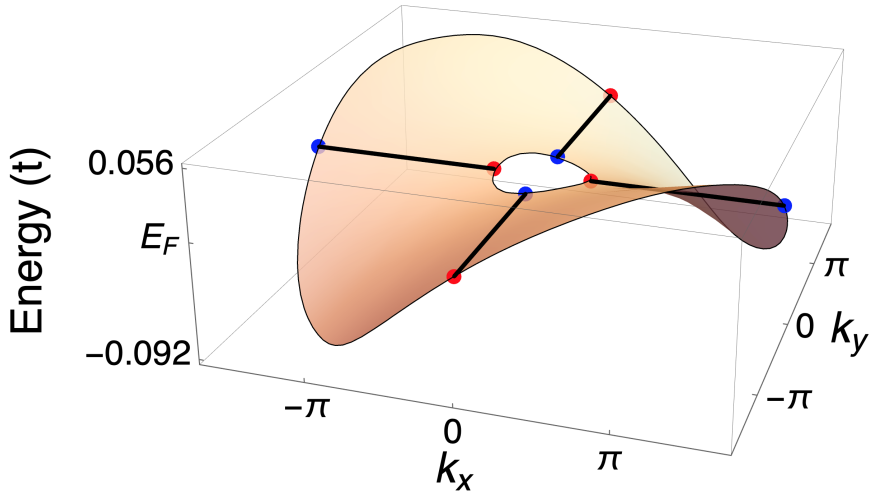

Figure 4.1 : Eigenenergy of the surface states of the [001] plane, with parameters $(E_d, \ell, r, V) = (-7, 7.28, 0.22, 7.5)$. Blue and red points show the position of the Weyl and anti-Weyl nodes of the Brillouin zone boundary, and thick black lines show the Fermi arcs connecting nodes to their opposite chirality partner on the four neighboring Brillouin zone boundaries.

4.3 Weyl-Kondo semimetal

In Chapter. 3, we established that our model captures a Weyl Kondo semimetal featuring Kondo renormalization-narrowed bulk and surface bandwidths, exhibiting bulk Weyl nodes and surface states with Fermi arcs. An example of the surface states and their band narrowing can be seen in Fig. 4.1, in which the bandwidth of the pure surface states is renormalized by the Kondo effect.

The configuration of Weyl monopoles is tuned along the Brillouin zone *boundaries* with a quarter of the bands filled (two of eight total), which is consistent with our choice of nonsymmorphic lattice and Hamiltonian [168, 78, 84]. The Weyl-Kondo quasiparticles form exactly at the Fermi energy, for reasons at two levels of sophistication

(i) the Weyl nodes appear within the Kondo resonances, which lie near the Fermi energy within a small energy window set by the Kondo temperature and

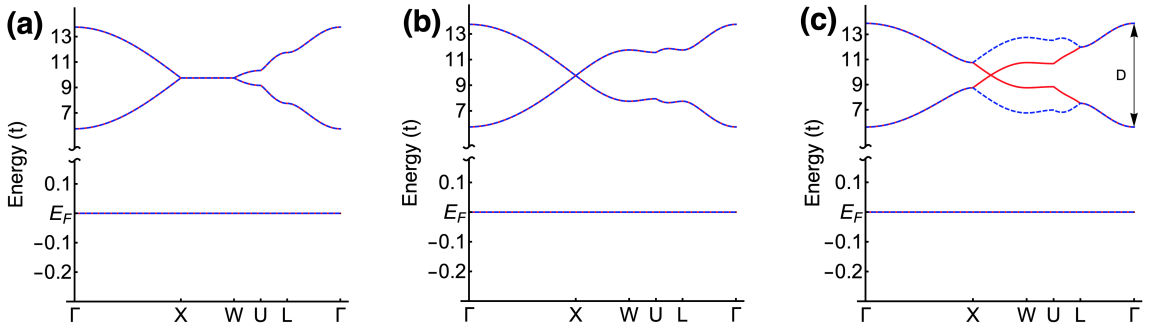

Figure 4.2 : *Model in the absence of the Kondo effect, $V = 0$.* Dispersion along a high symmetry path in the fcc Brillouin zone. The localized electrons' energy level is at the Fermi energy E_F. (a) Fourfold-degenerate line nodes along $X - W$ when SOC $\lambda = 0$ and inversion symmetry is preserved $m = 0$. (b) Dirac node develops at X from (a) when SOC is present, $\lambda > 0$. (c) Weyl nodes emerge from (b) when inversion symmetry is broken and $0 < \frac{m}{4\lambda} < 1$. $D \sim 8t$ denotes the unrenormalized conduction electron bandwidth.

(ii) the space group symmetry combined with the commensurate filling puts the nodes even closer to the Fermi energy - for the exact commensurate filling, the nodes are precisely at the Fermi energy.

In other words, the combination of the Kondo effect and space group symmetry pin the Weyl nodes to the Fermi energy.

Here, we analyze the mechanism that underlies this salient feature of the Weyl-Kondo semimetal phase.

4.3.1 Realization of the Weyl-Kondo semimetal through symmetry

In Sec. 4.1.1, we presented some considerations for seeking Weyl semimetals in 3D crystal lattices. We now turn to the specific case of the diamond lattice.

The diamond lattice has space group no. 227 ($Fd\bar{3}m$), which is centrosymmetric, nonsymmorphic, and bipartite, consisting of two fcc lattices displaced by $\mathbf{t} = a\{\frac{1}{4}\frac{1}{4}\frac{1}{4}\}$ (a is the cubic lattice constant). First, consider the Hamiltonian *without Kondo coupling ($V = 0$)* implemented on the diamond lattice, which involve four bands associated with two sublattices and two spin states, with localized E_d levels completely

decoupled from them. We consider the symmetry change as particular terms are successively added. In Fig. 4.2, the cases without Kondo coupling are shown, where the flat, trivial f bands are well separated in energy below the dispersive c bands. For the quarter-filling case we consider, the localized d electrons are at half filling, forming a Mott insulator, and the conduction c-electron bands are left completely empty, implying a topologically trivial insulator phase. If only the nearest-neighbor hopping and chemical potential terms [first two lines of Eq. (3.4)] are included, one has line nodes along $X - W$ as shown in the upper set of bands in Fig. 4.2(a). These fourfold degenerate line nodes crisscross the square BZB, due to a combination of the nonsymmorphic symmetry, two of the mirror planes, and the C_4 and C_2 rotations.

Next, we include the SOC (which preserves TRS and IS), which is shown in Fig. 4.2(b). The fourfold degeneracy at W is split, while a linearly dispersing degenerate Dirac point remains at X. The Dresselhaus SOC term which allows the pseudospin $|\pm D\rangle$ decomposition also allows the band inversion by introducing a linear-in-$\mathbf{k}$ coupling term based on the pseudospin eigenvalue $D(\mathbf{k})$, which is linear near the X point,

$$D\left[\mathbf{k}_X = (k_0, 0, 2\pi)\right] = 4\sqrt{\sin^2\left(\frac{k_0}{2}\right)} \sim 2|k_0| \tag{4.5}$$

for some $k_0 \sim 0$, and similarly for the other X points. The bands are twofold degenerate everywhere in the BZ except at the Dirac points, and in Fig. 4.2 this is indicated with solid red lines for the $|-D\rangle$ sector, and dashed blue lines for the $|+D\rangle$ sector. Since the SOC preserves TRS, the Kramers degeneracy at the time-reversal invariant momentum X is preserved, while the SOC splits them at W since it is not a time-reversal invariant momentum point. The space group analysis of how the nonsymmorphic symmetry of the diamond lattice produces such Dirac nodes at the X points have been established previously in a noninteracting model without a localized species; on the BZB, a projective representation with point group D_{4h} has a four-dimensional irreducible representation, which realizes a Dirac semimetal

generically [84].

We now include the ISB term parametrized by m, shown in Fig. 4.2(c). The $|\pm D\rangle$ degeneracy is split along the BZB, and doubly degenerate Weyl nodes of the $|-D\rangle$ sector emerge along all $X-W$ lines. This degeneracy produced by the internal sublattice degree of freedom is lifted, but since TRS is preserved, the Kramer's pairs remain with their TRS partners at X. This allows one to tune $\mathbf{k}$ between the X and W points to find a Weyl node degeneracy.

Put a different way, one can track the $X-W$ degeneracies as a function of the IS breaking. The Weyl semimetal phase region is $0 < m < 4\lambda$, with the Dirac node at X ($m = 0$) splitting and spawning the Weyl nodes as m is increased. The four nodes move outward toward each of the four W, and undergo a quadratic band touching at the critical value $m = 4\lambda$, before annihilating with the nodes of opposite chirality from the four neighboring BZs, which opens a trivial gap when $m > 4\lambda$ [166, 87].

It is also pertinent to consider the space group symmetry when identifying which pairs of bands can form band touching points, that is, to find what filling factor realizes a topological semimetal for a given space group. The filling factor ν counts the number of electrons per primitive unit cell; in our model [Eq. (D-1)], there are two types of fermions, two spins per fermion, and two sites per unit cell, so the total allowed filling factor is $\nu = 8$. At $\nu = 2$ corresponding to quarter-filling, the nonsymmorphic symmetry enforces that both the Fermi surface must be finite, and yet the Luttinger volume must vanish [90]. The only way to satisfy these conditions is to produce a zero dimensional nodal point Fermi surface, so nonsymmorphic space groups are a natural place to search for topological systems. When the space group symmetry is changed via ISB, this restores the ability of the system to connect adiabatically to a band insulator phase, when $m > 4\lambda$.

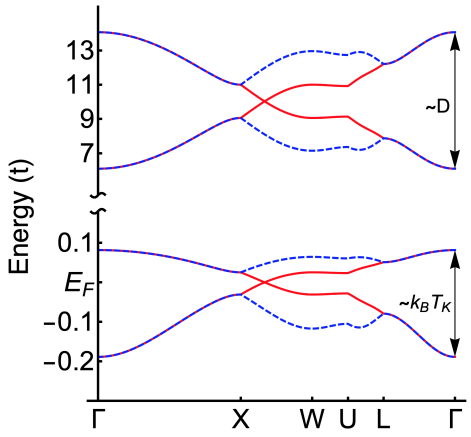

Figure 4.3 : *Kondo effect-driven Weyl nodes.* Dispersion along a high symmetry path in the fcc Brillouin zone. Weyl-Kondo semimetal with $V = 7.5$ and nodes pinned at E_F. This develops from Fig. 4.2(c) when the strong coupling is renormalized $\tilde{V} \to rV > 0$. The bandwidth of the upper quartet of bands is approximately that of the conduction electron bandwidth $\sim D$, whereas the strongly-renormalized lower quartet of heavy bands corresponds to the $k_B T_K$ energy scale. The parameters are $(E_d, \ell, r, V, \lambda, m) \simeq (-7, 7.279, 0.220, 7.5, 0.5, 1)$.

4.3.2 Kondo-driven node formation and pinning

We now wish to consider our model when the hybridization is nonzero, so that the conduction c and strongly correlated f electrons are coupled with each other. The choice of chemical potential and energy level $E_d = E_F$ before turning on hybridization is arbitrary, and was made to adiabatically connect the trivial insulator phase shown in Fig. 4.2 to the Kondo regime.

In the course of solving the saddle-point equations self-consistently, the starting value for E_d is far below E_F, and μ is determined analytically from the eigenergies as $\mu = -\frac{(rV)^2}{E_d+\ell}$ (see Appendix C1). A properly "strong" coupling solution usually means that r is small but nonzero, which arises for a range of V larger than some critical value. The small bosonic field measures a small but nonzero hole fluctuation r^2 away from $n_d = n_f = 1$, which is only coupled to V. A valid self-consistency solution always finds an r, ℓ that fixes the densities to the values specified. The solutions at this filling fix the Fermi energy such that of 8 total bands, 2 Kondo-driven bands are

filled, which corresponds to the $\nu = 2n$ filling enforcement condition.

A solution of this type was shown in Ref. [117]. To demonstrate its robustness, we solve the case with a different set of parameters. The result is plotted in Fig. 4.3, which shows the conduction electron bands with bandwidth D unoccupied, well-separated by a gap of $\sim 6t$ from the renormalized narrow f-bands with heavy Weyl-Kondo quasiparticle excitations around nodes fixed precisely at E_F. This demonstrates that the nodal states develop out of Kondo effect. The Kondo effect correlations produce this topological phase transition from trivial band insulator to WKSM, and *pin* the nodes to the Fermi energy as a fundamental property.

The role of the localized species near the Fermi energy can also be demonstrated by calculating the projected density of states. This is provided in Fig. 4.4, which corresponds to the hybridized parameters generating Fig. 4.3. The contributions of the c and f fermions are represented in shades of blue and red, respectively. The main panel of Fig. 4.4 shows that at the Fermi energy, the proportion of localized f fermions is large compared to that of the conduction c electrons, using an energy interval of $dE = t/10$. The inset of Fig. 4.4 shows a zoomed-in view of the projected density of states with a smaller energy interval of $dE = 0.005t$ to accommodate the reduced bandwidth. In the energies closest to E_F, the f fermions prominently characterize the states compared to the c's. The hybridization has allowed a tiny amount of c-electrons to mix (see inset) through the hole fluctuations of the r-bosonic condensate via $n_c = r^2$. This demonstrates that the localized f electrons are directly responsible for producing the Weyl-Kondo semimetal.

We close this subsection with two remarks. First, other quantities can also be calculated. For example, the surface states that correspond to the same parameter choice has already been shown in Fig. 4.1.

Second, going beyond the saddle-point level, the renormalized quasiparticles will acquire a finite lifetime due to the residual interactions. However, because the Kondo-driven Weyl nodes are pinned at the Fermi energy, the strongly renormalized nodal

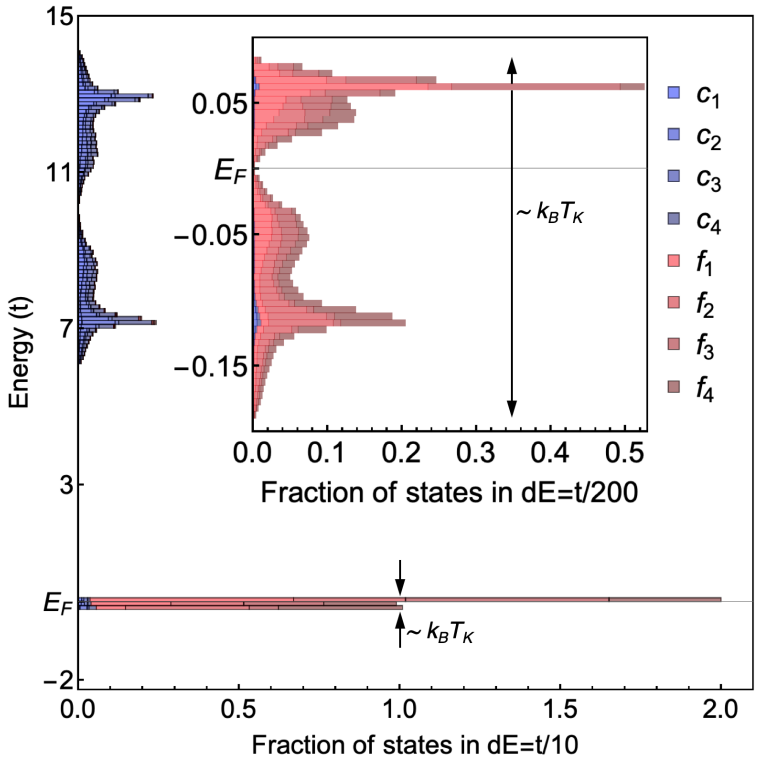

Figure 4.4 : Projected density of states, showing full energy range corresponding to Fig. 4.3. Inset: zoomed-in to localized set of bands near the nodes at E_F. Shades of red indicate contributions from f-fermions, and shades of blue indicate contributions from c-electrons. The parameters are $(E_d, \ell, r, V, \lambda, m) \simeq (-7, 7.279, 0.220, 7.5, 0.5, 1)$.

excitations will be long-lived, with the lifetime reaching infinity when the node is approached. This makes the Kondo-driven Weyl nodal excitations well defined even though it is a strongly interacting many-body system.

4.4 Tilted Weyl-Kondo semimetal

In the process of understanding a large spontaneous Hall effect observed in $Ce_3Bi_4Pd_3$, [162] a tilted variation of the Weyl-Kondo solution was introduced there. Here, we further investigate this effect. This allows us to analyze the details of the Berry curvature distribution near a small Fermi pocket centered around the Weyl nodes, and how this distribution can be made extremely asymmetric with respect to a Weyl or an anti-

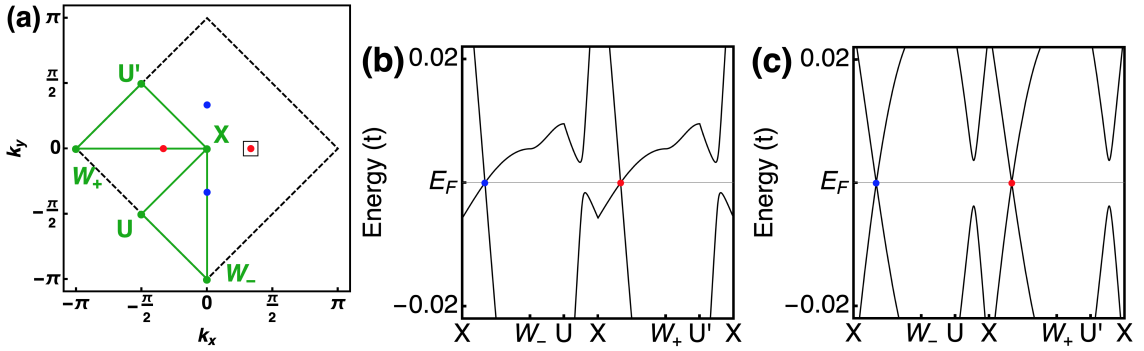

Figure 4.5 : *High-symmetry dispersion of the tilted WKSM model.* (a) high symmetry contour in green along the $\mathbf{k} = (k_x, k_y, 2\pi)$ Brillouin zone boundary plane, through (anti)nodes marked in (red)blue. The square marks the small region of the Brillouin zone over which the Berry-curvature distribution is shown in Fig. 4.6(a). (b) Bulk dispersion along the contour of the tilted model with $C = 0.8$, other parameters are found self-consistently to be $(E_d, \ell, r, V, \lambda, m) \simeq (-7, 7.282, 0.222, 7.5, 0.5, 1)$. (c) Bulk dispersion with $C = 0$, and the same parameters Fig. 4.3.

Weyl node by the tilting potential. Our results further support the analysis presented in Ref. [162].

4.4.1 Tilted Weyl dispersion and Berry curvature distribution

The tilting term in our diamond-lattice model [162] of the WKSM can locally adjust the anisotropy of the linear part of the dispersion. We specify it as

$$\mathcal{H}_t = C \sum_{\mathbf{k},\sigma} \left[1 - \frac{1}{2} D(\mathbf{k}) \right] n^c_{\mathbf{k}\sigma}, \tag{4.6}$$

which preserves the lattice symmetry and is added to the conduction electron Hamiltonian Eq. (3.4). Here, C sets the tilting potential, and we continue to consider the specific parameters of $m = 1$ and $\lambda = 1/2$. We have solved the saddle-point equations in the presence of the tilting term.

The resulting dispersion is contrasted to that of the un-tilted model, as shown in Fig. 4.5. The Weyl nodes remain pinned at the Fermi energy in the tilted case. This further illustrates the robustness of the mechanism discussed in the previous section for the formation and pinning of the Kondo-driven Weyl nodes.

To see the reason that the C term tilts the dispersion near the nodes, note that near the Weyl node, Eq. (**??**) is a 2×2 Hamiltonian matrix and can be linearized to obtain a $\mathbf{k} \cdot \boldsymbol{\tau}$ form. The Hamiltonian $\mathcal{H}_t$ is proportional to the matrix $\tau_0 \otimes \sigma_0$, which commutes with the canonical transformation, and after the transformation it contributes a term $C[1 - \frac{1}{2}D(\mathbf{k})]\tau_0$ to $h_{\mathbf{k}-}$. Linearizing the full $h_{\mathbf{k}-}$ near the nodes gives a linear dispersion which adds velocity components that depend on the tilting direction $\hat{t}$ as $\mathbf{v}_t = C\hat{t}$. Now the effective Hamiltonian is

$$H_{\text{eff}} = \mathbf{v}_t \cdot \mathbf{k}\tau_0 + v\mathbf{k} \cdot \boldsymbol{\tau}. \tag{4.7}$$

Using the velocity ratio, the effective Hamiltonian has the regimes $|\frac{C}{v}| < 1$ (type I), and $|\frac{C}{v}| > 1$ (type II) [169]. The type-I behavior makes the dispersion anisotropic, and causes the Fermi surface to change shape within the BZ. A type-II Weyl semimetal arises when the tilt has become extreme enough to cause a Lifshitz transition of the Fermi surface.

In Fig. 4.5 we illustrate the tilting of the linear bands around the node when $C \neq 0$; we plot the eigenenergies along the green high-symmetry $\mathbf{k}$-contour in Fig. 4.5(a) that intersects with the Weyl nodes. Fig. 4.5(b) shows the dispersion of a strong coupling limit solution when $C = 0.8$, where there are anisotropic slow and fast bands along $X - W_{\pm}$. There also appears to be two Lifshitz transitions ready to happen: the type-I to type-II tilting transition, and the Fermi pocket lowering itself to the Fermi energy around U and U'. This is in contrast to the non-tilted $C = 0$ dispersion shown in Fig. 4.5(c), where the linear part of the dispersion appears isotropic along $X - W_{\pm}$ for energies sufficiently close to E_F.

We show in Fig. 4.6 the Berry curvature distribution for a tiny portion of the BZ that surrounds one of the Weyl nodes of Fig. 4.5(a) (denoted by the small square surrounding the right red node of Fig. 4.5(a)).

An intriguing question is how to tune the singular nature of the Berry curvature. Tilting the Weyl cone dispersion is one means of doing so. An example of the tilt behavior of the model is seen in Fig. 4.6. The color scale indicates the magnitude

of the Ω_{yz} component of the Berry curvature, which is highly concentrated around the node and discontinuous at the node, located in the center of each plot. The solid and dashed contours show the Fermi surface produced with $C = 0$ and $C = 0.9$, respectively, from a slightly metallic filling $n_d + n_c = 1 + 10^{-5}$. For both cases, but especially for the tilted case, the Berry curvature is very large on the Fermi surface, reflecting the proximity of the Fermi surface to a Weyl monopole.

In Fig. 4.6(a), the area in the momentum space shown corresponds to the small square surrounding the right red node of Fig. 4.5(a). This conveys how tiny the Fermi surfaces are compared to the extent of the BZ. In Fig. 4.6(b), we zoom in further from Fig. 4.6(a) to the vicinity of the node. Here, it is apparent that the $C = 0.9$ tilted Fermi surface (dashed line) still encloses the node, but it is much closer to the node as compared to the $C = 0$ Fermi surface (solid line). The tilting term is seen to make the Fermi pocket and the associated Berry curvature be distributed around the Weyl node in a highly asymmetrical way, in which highly singular Berry curvature fields strongly influence the heavy Weyl quasiparticles pinned at the Fermi surface.

In particular, Figs. 4.6(a) and 4.6(b) illustrate that the asymmetry induced by the tilting term has made one side of the Fermi pocket to be much closer to the node than the other. This makes an external electric field to be readily able to drive the system to a highly out-of-equilibrium response in the Berry-curvature-induced transverse conductance, a theoretical framework that was advanced for the spontaneous Hall effect in Ref. [162]. As such, our result concretely demonstrates the ready realization of the giant spontaneous Hall effect put forward there.

4.5 Signatures of correlated topological semimetals

Some of the conventional signatures of Weyl semimetals are quantum oscillation experiments, negative longitudinal magnetoresistance indicative of the chiral anomaly, and angle-resolved photoemission spectroscopy (ARPES) imaging of both the bulk and surface states, which probes the linear nodal dispersion in the bulk and veri-

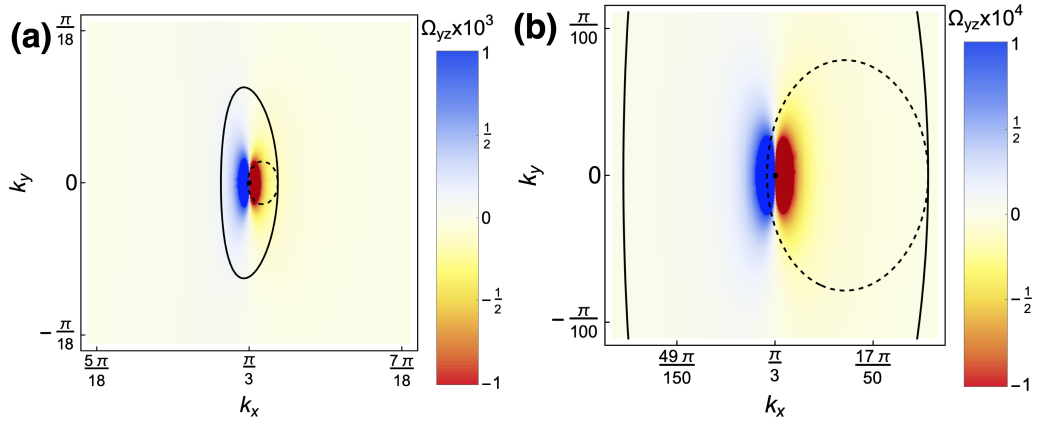

Figure 4.6 : *Berry curvature strength captured by Fermi surfaces.* The Berry curvature component Ω_{yz} [Eq. (1.11)] of the WKSM phase in the [001] plane of the Weyl node located at the center of the plot, $\mathbf{k} = (\frac{\pi}{3}, 0, 2\pi)$ (black dot), which corresponds to the right red point of Fig. 4.5(a), and Fermi surfaces from a slightly metallic filling $n_d + n_c = 1 + 10^{-5}$, sharing the parameters $(E_d, V, \lambda, m) \simeq (-7, 7.5, 0.5, 1)$. (a) The solid contour is the intersection of the three dimensional Fermi surface of the model with the BZ-boundary plane (*i.e.*, for $k_z = 2\pi$) without tilting, and self-consistently determined parameters $(C, \mu, r, \ell) \simeq (0, -9.748, 0.220, 7.279)$. The dashed contour is the counterpart for the Fermi surface of the tilted model, with parameters $(C, \mu, r, \ell) \simeq (0.9, -9.811, 0.222, 7.281)$. (b) Same as (a), but with an even smaller plot range in $\mathbf{k}$-space. The full range of the Berry curvature is truncated, and the deep blue and red regions near the node represent values that extend beyond the legend. Note that, in the three dimensional BZ, the Fermi pockets in the two cases have the same volume.

fies topology due to the bulk-boundary-correspondence. These experiments elegantly illustrate the signatures of *weakly correlated* Weyl semimetal material candidates.

As has been pointed out recently, [162] the *strongly correlated* Weyl-Kondo semimetal phase offers several obstacles to characterization by conventional experimental probes. For example, imaging the surface states would have to use an ARPES setup that could resolve features within a bandwidth of approximately $D^* \sim k_B T_K$, with for example, in $Ce_3Bi_4Pd_3$, $T_K \approx 13\,\mathrm{K}$, which would require an ultrahigh resolution much below $D^* \sim 1\,\mathrm{meV}$. On the other hand, the WKSM displays unique physics that offers more suitable probes. The WKSM phase exhibits node pinning that is contingent on the development of the Kondo effect, a slow effective Weyl fermion velocity, and, cor-

respondingly, a narrowed bandwidth. The Kondo-driven node pinning implies that a large Berry curvature singularity at the Fermi energy develops at $T < T_K$. This provides a means of using the Berry-curvature-induced anomalous velocity to probe the topological characteristics of the Kondo-driven Weyl nodes in the WKSM (that is time-reversal invariant in equilibrium), at zero magnetic field and in a nonlinear response to an applied electric field, as has recently been demonstrated in Ref. [162].

4.6 Conclusions and Outlook

We have expanded on several theoretical aspects of the Weyl-Kondo semimetal state in a noncentrosymmetric Kondo/Anderson lattice model with both strong correlations and large spin-orbit coupling. This state was advanced concurrently in theoretical [117] and experimental [137, 162] studies. It preserves the time-reversal invariance. The Weyl nodes are driven by the Kondo effect and, thus, must appear within the narrow energy range near the Fermi energy for the Kondo resonance; at the same time, their existence can be traced to the degeneracy of electronic states enforced by nonsymmorphic space-group symmetry. These two features combine to pin the Weyl nodes to the immediate vicinity of the Fermi energy. Moreover, the Kondo-driven nature makes the linearly-dispersing Weyl nodal excitations to have an energy scale $k_B T_K$, which is smaller than the bare conduction-electron bandwidth D by orders of magnitude (*c.f.* Fig. 4.3). Correspondingly, the velocity v^* is reduced from typical values of noninteracting electrons by several orders of magnitude. An immediate consequence of such a reduced velocity is that the specific heat $c_V = \Gamma T^3$, with the T-cubic prefactor Γ enhanced from the typical non-interacting value by a huge factor of $(v/v^*)^3$. The pinning of the Weyl nodes to the immediate vicinity of the Fermi energy also implies that the Berry curvature singularities of the Weyl nodes appear near the Fermi energy. This gives rise to a large anomalous velocity for the states on a small Fermi surface pocket surrounding the Weyl nodes. As such, this pinning of the Berry curvature singularities near the Fermi energy presents a means of

probing topological characteristics of Weyl nodal excitations through a spontaneous Hall effect, which is a nonlinear response to an applied electric field, even though the system under equilibrium preserves time-reversal symmetry.

The experimental developments have taken place in the Kondo-driven semimetal $Ce_3Bi_4Pd_3$, a cubic system for which the space group is nonsymmorphic (no. 220), the inversion symmetry is broken, but the time-reversal symmetry is preserved [162]. This new heavy fermion semimetal shows a T^3 specific heat with a huge prefactor Γ, so much so that it surpasses the phonon contribution, [137] and a giant spontaneous (zero magnetic field) Hall effect and an accompanying even-in-magnetic-field component. [162] The results provide direct evidence for ultraslow Weyl nodal excitations and its topological nature.

We close with a look into future directions. First, the developments along this direction point to the search for further Weyl-Kondo semimetals in heavy fermion systems with nonsymmorphic space groups, as already exemplified by the case of $Ce_3Bi_4Pd_3$. [137, 162, 170] Because the majority of the 230 space groups in three dimensions are nonsymmorphic, this suggests the prevalence of Weyl-Kondo semimetal phases in such systems. Of potential interest in this context include nonsymmorphic heavy fermion semimetals with broken inversion symmetry such as $CeRu_4Sn_6$ [158, 134, 135, 156, 157] and CeNiSn, [171, 139, 172] and those that are inversion symmetric but with time-reversal symmetry broken by an external magnetic field or magnetic ordering, such as YbBiPt [173, 174, 96, 153] and CeSbTe. [175, 176, 177]

Second, the considerations of symmetry open up different ways to think of accessing nearby topological phases, by reducing or restoring point-group or space-group symmetries. One path that has been explored is anisotropically tuning the hopping amplitudes t_{ij} of the lattice bonds [62, 166]. Such a symmetry-reducing tuning could be approximated through uniaxial stress, which, in Kondo systems, also tunes the strength of the Kondo effect. Another avenue is to explore nonspatial symmetries, such as time-reversal symmetry breaking [170]. In a one fermion flavor model [178],

we have established that a tunable TRSB term can coexist with the Weyl semimetal phase described in Sec. 4.3.1, but that when the TRSB term is larger than the ISB term, a topologically distinct Weyl semimetal phase can emerge with nodes in the Brillouin zone interior. It is an exciting next step to incorporate TRSB to the full Kondo-driven model. Finally, doping studies represent a promising way of tuning [137, 179].

Third, the theoretical and experimental results on the Weyl-Kondo semimetal sets the stage to address how the overall quantum phase diagram of heavy fermion metals, Fig. 1.1(b), is enriched by topologically nontrivial metallic phases driven by the combined effects of strong correlations and spin-orbit coupling. A recurring theme of heavy fermion metals is that novel phases develop in the quantum critical regime, at the border of electronic orders. This reflects the accumulation of entropy in the quantum critical regime [180, 181, 182, 44], as a result of which the electronic matter is soft and prone to developing novel phases. A canonical example of such emergent phases is unconventional superconductivity [183, 32], but it could also be nematic or other forms of secondary electronic orders [184]. An intriguing possibility is that, when the spin-orbit coupling and correlations are both strong, topologically nontrivial metallic states appear as emergent phases at the border of electronic order, albeit on the nonordered [i.e., disordered; cf. Fig. 1.1(a)] side.

Finally, the approach taken here represents a general means of treating the space-group symmetry enforcement of topological semimetals in strongly correlated settings. In the theoretical model, the Weyl nodes of the bare conduction electrons enforced by the space group symmetry are located far away from the Fermi energy. When the Kondo effect takes place, the Weyl nodes are transmitted to those of the Kondo-driven quasiparticles. The combination of strong correlations and space-group symmetry enforcement pins the Kondo-driven Weyl nodes to the immediate vicinity of the Fermi energy. This makes the strongly correlated Weyl-nodal excitations to be well-defined, even for a underlying many-body system that is strongly interacting. Equally important, it allows the theory to connect with the striking experiments in

$Ce_3Bi_4Pd_3$ [137, 162, 170]. This type of interplay between the space-group symmetry constraint and strong correlations is likely to be important in other settings of strongly correlated topological matter as well.

Chapter 5

Weyl-Kondo semimetal's nodal evolution under a magnetic field

5.1 Introduction

The heavy fermion systems have long been explored using the magnetic field as a probe, since it is a nonthermal tuning parameter that can help access quantum critical points and perturb the f electron local moments, which can provoke phase transitions. A magnetic field can reveal a jump in the normal Hall effect that originates from an abrupt change in the Fermi surface volume at a local quantum critical point [16, 31, 18, 17]. In Chapter 2, the anomalous Hall effect was monitored in Kondo lattice systems across a Kondo destruction QCP within paramagnetic phases that are time-reversal symmetry broken (TRSB) via chiral spin liquid phases. Similarly, the presence of a magnetic field breaks time reversal symmetry, as would an antiferromagnetic ordering of the localized moments.

With the contemporaneous discovery of evidence for a Weyl-Kondo semimetal phase in both theoretical models [116, 117] and experiments on the proposed WKSM $Ce_3Bi_4Pd_3$ [137, 162], there is still much to elucidate on the nature of strong correlations driven topology. More recently, a magnetic field study was carried out on $Ce_3Bi_4Pd_3$ [170]. By analyzing the Hall effect, resistivity, and torque magnetometry, it was suggested that the magnetic field tuned from a zero-field WKSM toward a nodal annihilation topological phase transition into a Kondo insulator type phase, and then through a second (perhaps quantum critical) point into a partially polarized metallic heavy Fermi-liquid.

Similarly, the work in Appendix C2 (Ref. [185]) has studied the phase diagram

of a single electron species model of an inversion symmetry broken WSM with a TRSB Zeeman term. There, it was found that the original WSM phase survived at a finite TRSB field until the Zeeman field strength surpassed the ISB staggered potential. Then, as the Zeeman term is increased, a series of distinct topological Lifshitz transitions of nodal annihilation and creation open up two new distinct WSM phases, before becoming a band insulator.

In this work, we use the same key elements: the lattice and its associated nonsymmorphic space group properties, and the symmetries of the Hamiltonian are largely similar. However, we now incorporate these into the two fermion species Anderson lattice model, and focus on the largest Zeeman coupling, which is to the magnetic moments, and find self-consistent solutions in the strong coupling (Kondo) limit. As a function of the Zeeman field, we find a progression of topological phase transitions that occur in the same symmetry determined sequence, albeit driven almost entirely by the f electrons and at a renormalized energy scale of the Zeeman field.

5.2 Model and methods

To investigate the magnetic field dependent properties of the WKSM, we begin with a diamond lattice, and use the Anderson lattice model [116, 117],

$$\mathcal{H} = \mathcal{H}_c + \mathcal{H}_{cd} + \mathcal{H}_d. \tag{5.1}$$

The conduction electrons of the system are based on the Fu-Kane-Mele model with broken inversion symmetry [62, 87, 166],

$$\begin{aligned}\mathcal{H}_c = t \sum_{\langle ij\rangle,\sigma} \left(c^\dagger_{i\sigma} c_{j\sigma} + \text{H.c.} \right) - \mu \sum_{i,\sigma} n^c_{i\sigma} \\ + i\lambda \sum_{\langle\langle ij\rangle\rangle} \left[c^\dagger_{i\sigma} \left(\boldsymbol{\sigma} \cdot \mathbf{e}_{ij} \right) c_{j\sigma} - \text{H.c.} \right] + m \sum_{i,\sigma} (-1)^i c^\dagger_{i\sigma} c_{i\sigma}.\end{aligned} \tag{5.2}$$

The hopping term is over nearest-neighbor bonds $\langle i, j\rangle$ with chemical potential μ, a Dresselhaus-type spin orbit coupling parameterized λ, and staggered onsite potential

m. These electrons are coupled to the d fermion species (representing the physical $4f$ moments) through the hybridization term

$$\mathcal{H}_{cd} = V \sum_{i,\sigma} \left(d^\dagger_{i\sigma} c_{i\sigma} + \text{H.c.} \right). \tag{5.3}$$

Last, the localized species is represented by

$$\begin{aligned} \mathcal{H}_d = & E_d \sum_{i,\sigma} d^\dagger_{i\sigma} d_{i\sigma} + U \sum_i n^d_{i\uparrow} n^d_{i\downarrow} \\ & + M_z \sum_i \hat{z} \cdot \left(d^\dagger_{i\sigma} \boldsymbol{\sigma} d_{i\sigma} \right), \end{aligned} \tag{5.4}$$

where the first line has the two typical Anderson lattice model terms, the highly localized energy level * E_d, and the Coulomb repulsion U between the d fermions discourages double occupation on a site i.

Since the TRS WKSM state appears in the Kondo limit, the interplay of the bosonic condensate and filling enforcement enabled local moments to access all Hamiltonian symmetries that produce Weyl nodes. The same ought to be true in the TRSB case, so including a TRSB Zeeman term should be adequate. In a heavy fermion system subjected to a magnetic field, the main effect is the response of the local moments. To model this we have included the Zeeman interaction in the second line of Eq. 5.4, aligned in the $\hat{z}$ direction.

We are interested in the Kondo limit at very strong correlations, so the slave boson method is implemented as in Section 4.2. The Coulomb repulsion is taken to infinity, which amounts to a constraint of no double occupancy of the d-electrons. We solve the problem at the saddle point level, where the constraint gives rise to a term in the Hamiltonian that takes the place of the Coulomb term:

$$\mathcal{H}_\ell = \ell \sum_{i,\sigma} (f^\dagger_{i\sigma} f_{i\sigma} + r^2 - 1). \tag{5.5}$$

This introduces a parameter ℓ that renormalizes the f fermion energy level. The parameters μ, ℓ and r are determined by solving the system of saddle point equations.

* E_d is assumed to lie far lower in energy than the conduction electron band edge [1, 60]

The solutions are obtained numerically through the Newton-Raphson and bisection methods. There are two main obstacles to the successful calculation of the solution. First, an initial guess of parameters are needed that is sufficiently close to the solution; this is more of an art than science. Second, in systems with nodal Fermi surfaces, the solutions might never converge or do so slowly. This is because the saddle point equations involve discretized integrals over the occupied bands of the BZ, one of which is the total density:

$$n_d = \frac{1}{N_{\text{site}}} \sum_{i,\sigma} d^\dagger_{i\sigma} d_{i\sigma}, \tag{5.6}$$

$$n_c = \frac{1}{N_{\text{site}}} \sum_{i,\sigma} c^\dagger_{i\sigma} c_{i\sigma}, \tag{5.7}$$

with N_{site} counting the total number of sites in the lattice.

In correcting the calculated density to match the filling factors $n_f,\ n_c$ requested, the parameters $\mu,\ \ell$ are changed by the solution algorithm. However, it is easy for the discretization to miss node locations, leading to slow or impossible convergence to a solution. In my approach, these two problems are tackled by initially doping the system by a tiny amount to get close to a solution, then reverse the doping to get the final solution. For instance, we are interested in a total quarter filling $n_d + n_c = 1$, which is 1 fermion per site; in the strong coupling limit we have $n_f + r^2 = 1$, implying that $n_c \sim r^2$. Doping the requested total density to $1 + 10^{-4}$ fermions per site, which gives a small, isolated Fermi surface surrounding each node. Once a doped solution is found, the solution is fed back into the self consistent calculations, and the quarter-filling solution can be quickly and accurately reached.

5.3 Results

For weakly correlated Weyl semimetals in the presence of a magnetic field, the electrons' dominant response to the magnetic field is the orbital effect which leads to the formation of Landau levels. However, in the Kondo limit, the orbital effect is much

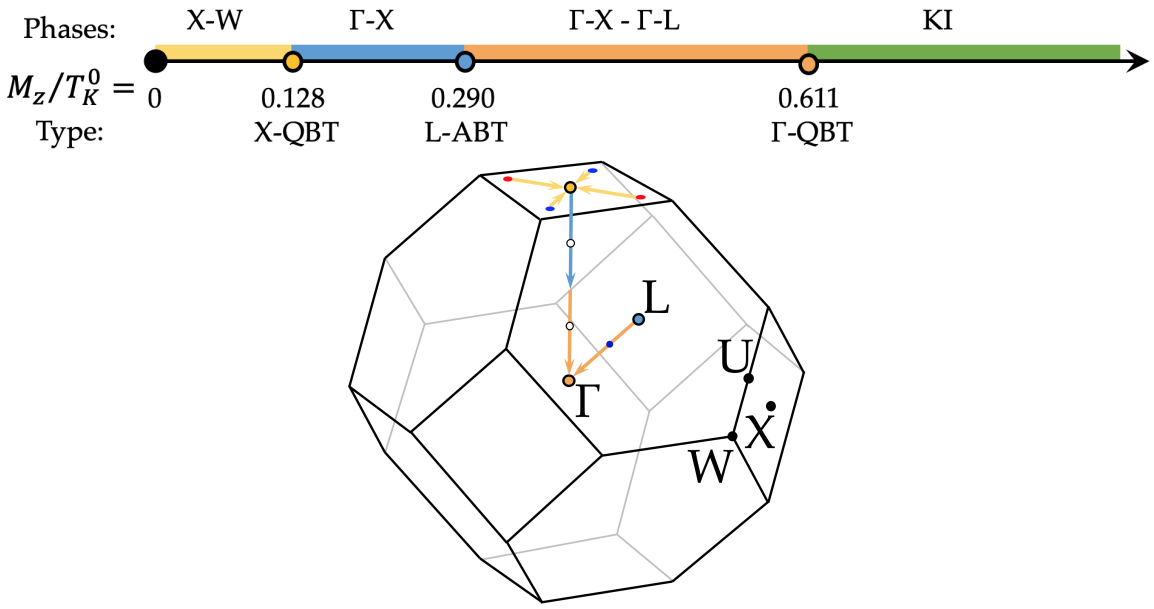

Figure 5.1 : (a) Phase diagram of the WKSM model as a function of the Zeeman field M_z normalized by the zero-field Kondo temperature T_K^0. (b) The path of selected nodes through the fcc Brillouin zone, with the arrow colors corresponding to the phases and critical points in (a).

weaker than the Zeeman effect. In Fig. 5.1, the top line diagram shows the progression of phases in the system as the TRSB Zeeman parameter M_z is increased. It is tuned relative to the Kondo temperature T_K^0, which is estimated from the bandwidth of the heavy Weyl bands for $M_z = 0$, as labeled in Fig. 5.2. The constant parameters throughout this study are $\{E_d, V, \lambda, m, t\} = \{-7, 9.29, 0.5, 1, 1\}$, and alone these input parameters determine the μ, r, ℓ solution. Fig. 5.2 shows the TRS-respecting WKSM phase at the $M_z = 0$ part of the phase diagram, with nodal points occurring along the X-W lines of the BZB [116, 117]. The BZ is shown in Fig. 5.1, where the red and blue dots mark the position of one set of Weyl node pairs, of Berry curvature monopoles and antimonopoles, possessing topological charge ± 1.

When the Zeeman field is turned on, remarkably, the Weyl nodes are not gapped out, nor do they leave the BZB, nor do they move away from the Fermi energy. Instead, the nodes move along the yellow arrows in Fig. 5.1, corresponding to the yellow

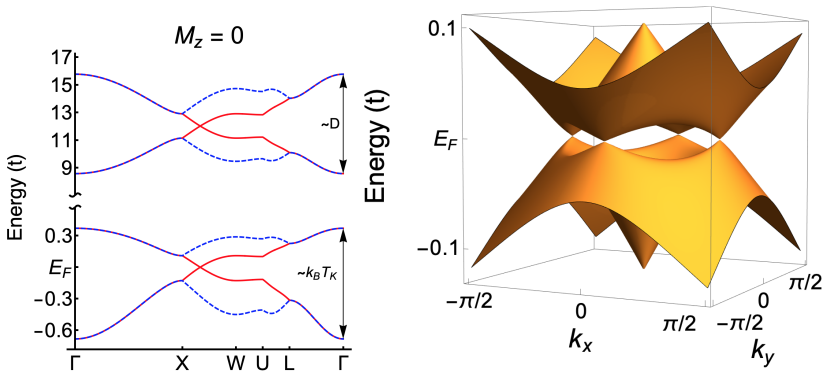

Figure 5.2 : X-W WKSM eigenenergy dispersion of the model at $M_z = 0$ (time-reversal symmetry is preserved). (a) One dimensional high symmetry path through the BZ. (b) On the $k_z = 2\pi$ plane.

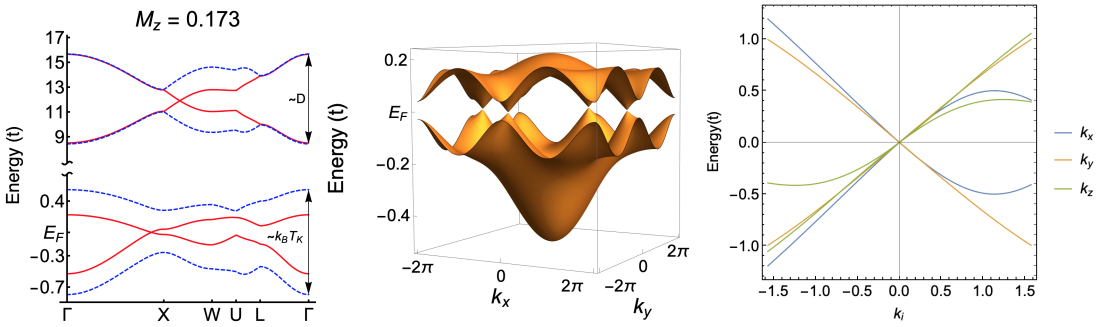

Figure 5.3 : Γ-X WKSM eigenenergy dispersion of the model at $M_z = 0.173$. (a) One dimensional high symmetry path through the BZ. (b) On the $k_z = 0$ plane. (c) Dispersion near the node along the three cartesian directions.

X-W regime above it. It is also worth noting that the bands are now inversion-split and Zeeman-split, and are generally nondegenerate, except at nodes. When $M_z/T_K^0 = 0.128$ (the yellow circle), the nodes meet at the X point, where the dispersion forms a non-Kramer's type quadratic band touching, hence the regime boundary is named X-QBT.

Next, new nodes are formed just inside the BZB along each of the six Γ-X lines; one is shown in Fig. 5.1 along the blue arrow (white circle). An example of the eigenenergy dispersion in one and three dimensions is shown in Fig. 5.3, which are typical of

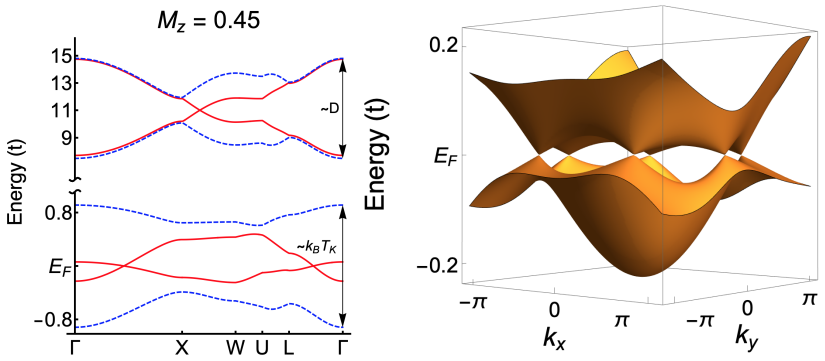

Figure 5.4 : Γ-X − Γ-L WKSM Eigenenergy dispersion of our model at $M_z = 0.45$ (as in Fig. **??**). (a) One dimensional high symmetry path through the BZ. (b) On the [011] plane, with origin at Γ.

the new Γ-X WKSM phase. Note that the node location of the empty conduction electron bands (left of Fig. 5.3) remain along the $X - W$ WKSM phase, and only displays Zeeman splitting, which is small compared to its bandwidth. Interestingly, the two pairs of nodes per BZB of the X-W phase has undergone a topological Lifshitz transition and become only three pairs of nodes. This is because the Γ-X node pairs that emerge from the QBT at X are in fact double-Weyl fermions which have two directions of quadratic dispersion and one direction with linear dispersion [186, 187, 188, 189, 190, 191, 192, 193, 194, 195]. For example, in the vicinity of the $+k_x$ Γ-X node, along the k_y directions the dispersion is linear, and quadratic in the k_x and k_z directions, shown in Fig. 5.3. However, since the quadratic k_x dispersion comes from the X-QBT, the nodes are formed on each side of the $k_x = 2\pi$ BZB as the upper and lower bands move past each other in energy; the quadratic k_z dispersion retains a QBT. Double Weyl fermions are associated with monopole charge ±2, and can be formed if two same-sign monopoles are combined [191, 193]. Such a scenario could explain how the number of Weyl node pairs is halved from the X-W WKSM phase to the Γ-X WKSM phase, if the same sign monopoles merged. This X-QBT transition thus shows the formation of double Weyl fermions as a function of tuning the Zeeman field.

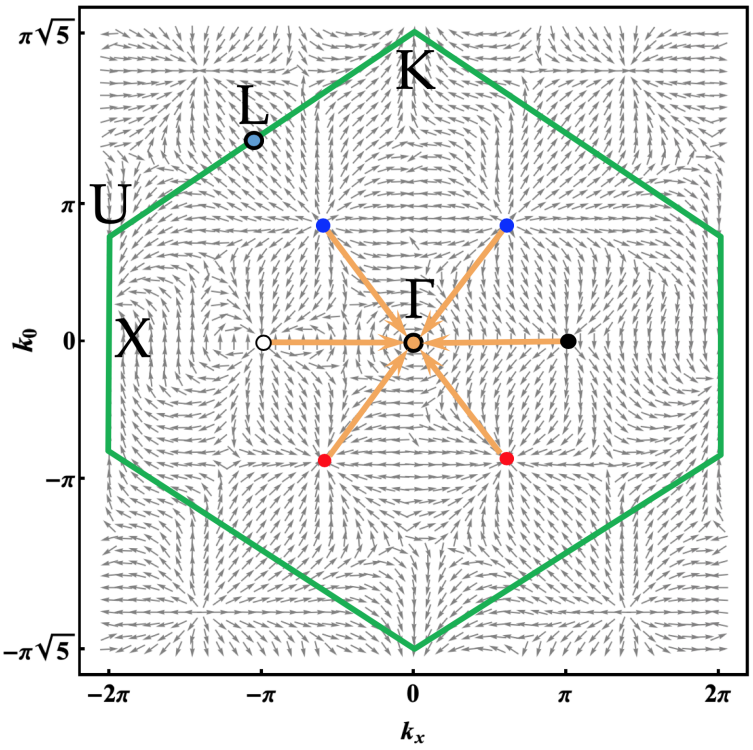

Figure 5.5 : Berry curvature projected onto the [011] plane of our model in the Γ-$X-$Γ-L Weyl-Kondo semimetal phase at $M_z = 0.45$. The Brillouin zone boundary is shown in green, and orange arrows indicate the node pairs' path toward simultaneous annihilation at the Γ point.

When $M_z/T_K^0 = 0.290$ (the blue circles in Fig. 5.1), the Γ-X nodes are at the halfway points through their trajectory towards Γ. Here another topological phase transition boundary occurs when an anisotropic band touching (ABT) occurs at the L points of the BZB, labeled the L-ABT critical point. Along the [111] directions, at quarter filling, there are two QBTs, but along other directions looks linear. As M_z is further increased, four pairs of (single) Weyl nodes appear from the L points on the interior of the BZ (see Fig. 5.4), and their presence does not disrupt the existing Γ-X nodes. The new sets of nodes move along the Γ-L (or [111]) direction towards Γ, along with the Γ-X nodes; this variant is named the Γ-$X-$Γ-L WKSM. This phase corresponds to the orange phase and arrows in Fig. 5.1.

The normalized Berry curvature field of the Γ-$X-$Γ-L WKSM is shown in Fig. 5.5, projected onto the [011] plane to show both the Γ-X and Γ-L nodes. The Γ-L nodes (blue and red points) have conventional monopole fields, while the Γ-X nodes have an unconventional Berry curvature field structure, which does not resemble the double-Weyl point fields of continuum models [189, 191, 192], nor what happens for crystal structures like $HgCr_2Se_4$ and $SrSi_2$ [187, 188, 190], or on (mostly) simple C_n point groups [186, 187, 188, 190, 194].

The Berry curvature field configuration in Fig. 5.5 can be somewhat compared to studies on the HgTe-class materials, such as the Luttinger semimetal α-Sn, which has a diamond lattice structure [195], but is weakly correlated. Ref. [195] used an effective $k \cdot p$ to study the creation of double-Weyl nodes in unstrained α-Sn, which are generated from the Luttinger semimetal phase under a magnetic field or off-resonant circularly polarized light; however the Weyl nodes generated often sit at differing energies (the WKSM does not have this issue, see Discussion Sec. 5.4). The WKSM model includes an inversion symmetry breaking term parameterized by m which changes the diamond lattice space group from no. 227($Fd\bar{3}m$) to the no. 216($F\bar{4}3m$) group, corresponding to zinc blende. However, Ref. [195] finds that including a linear inversion symmetry breaking term (which similarly reduces their diamond structure to zinc blende), and this perturbation splits the double-Weyl fermions into single-Weyl fermions. The WKSM model is able to realize double-Weyl fermions in the presence of TRSB and ISB.

It is a general property of (double) Weyl nodes that they are protected by and related to opposite chirality partners by point group symmetry operations [186, 187]. One difference between the models is that the α-Sn system has its nodes positioned close to the zone center Γ, which has a point group representation equivalent to the space group representation, which is T_d in zinc blende [187]. The WKSM model's single and double Weyl nodes lie along the namesake Γ-X and Γ-L high symmetry lines, which are associated with point groups C_{4v} and C_{3v}, respectively [79]. These lines

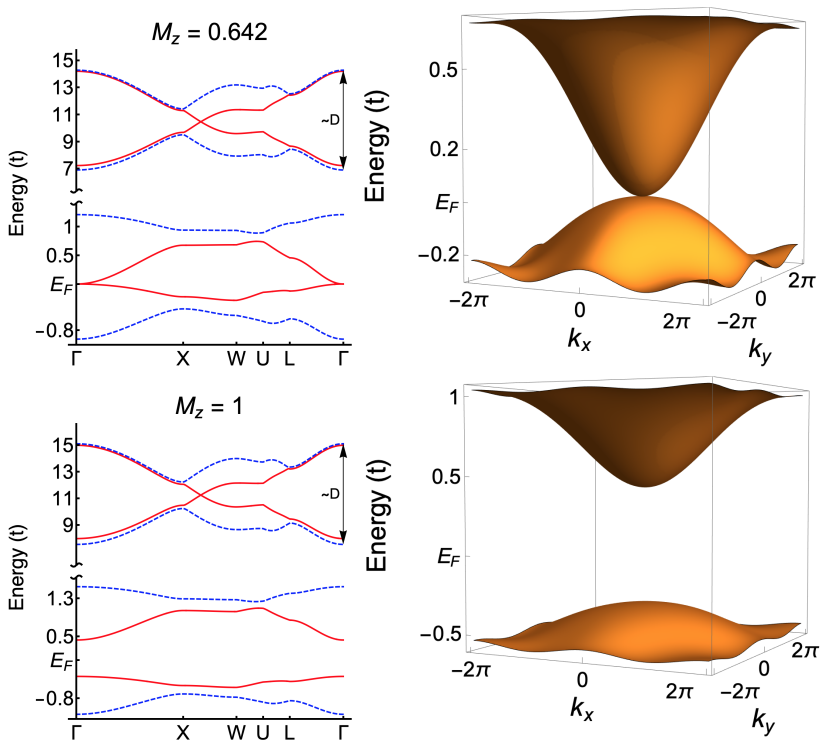

Figure 5.6 : (a) and (b): Γ-QBT Kondo semimetal eigenenergy dispersion of the model at $M_z = 0.642$; (c) and (d): Kondo insulator dispersion at $M_z = 1$. (a) and (c): One dimensional high symmetry path through the BZ. (b) and (d): On the k_x-k_y plane, with origin at Γ.

have lower symmetry than the zone center, and are the kind of quasi-two dimensional point groups that were explored in the double-Weyl literature [186, 187, 188, 190, 194], where it is also noted that the Γ-L line can generally not support double Weyl nodes [186, 187].

Finally, the orange arrows of Fig. 5.5 show the remaining trajectory of the nodes towards the Γ point as M_z is increased further. The Γ point labeled by the orange circle is placed in the phase diagram and BZ nodal trajectory as well in Fig. 5.1. However, the nodes do not immediately annihilate at the zone center, instead momentarily becoming a quadratic band touching critical point (labeled Γ-QBT), which is shown in Fig. 5.6(a)-(b). The Γ-QBT point is unusually non-Kramers due to the broken TRS, composed of singly degenerate bands. Beyond this value of M_z, the

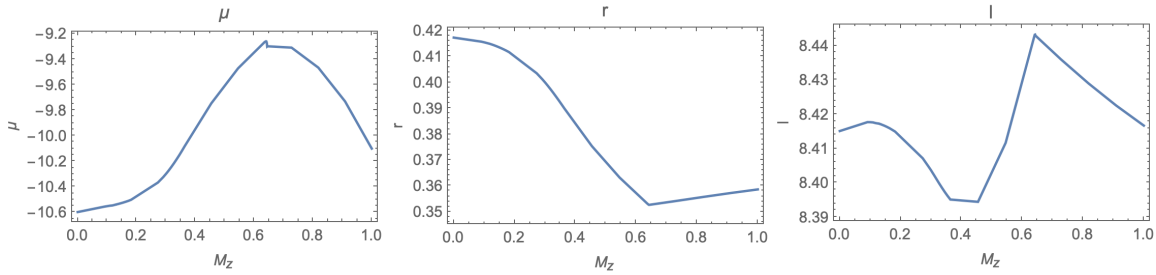

Figure 5.7 : The order parameters obtained by self-consistently solving the saddle point equations plotted as a function of M_z. (a) Chemical potential μ, (b) scalar bosonic condensate r, and (c) Lagrange multiplier ℓ.

Γ-QBT gaps out, leading to a Kondo insulator.

The Γ-QBT transition is not just a topological transition, but an actual transition in the WKSM model. This is evidenced by plotting the values of the self-consistently obtained parameters $\mu,\ r,\ \ell$ as a function of M_z, as shown in Fig. 5.7. Though μ shows only a small kink at the Γ-QBT Zeeman value of $M_z = 0.642$, the kinks in r and ℓ are much more pronounced [†]. The parameters seem to reverse slope after the kink, which likely results from the change in density of states at the Fermi energy. In general, the Kondo effect is highly sensitive to differently configurations of density of states, so it is responsible for the differences between the gapless versus gapped states, which manifests in the numerical solutions.

5.4 Discussion

The WKSM under a Zeeman field predominantly affecting the f-fermions produces three topologically distinct Weyl Kondo semimetal phases and an unusual avenue to a Kondo insulator. Two of the WKSM phases, spanning a large part of the M_z phase diagram, include double Weyl fermions, which have quadratic dispersions in

[†]The jaggedness of ℓ around $M_z \in (0.35, 0.46)$ is an artefact of a lower sampling rate, and does not correspond to a phase transition

two directions, and is linear in one direction. Because of the higher order dispersion, double WKSM nodes have an enhanced density of states at the Fermi energy. It has been suggested in weak interaction contexts that this makes double Weyl fermions more sensitive to the effects of interaction and disorder, which could lead to the emergence of a non-Fermi liquid state [187]. The anisotropic dispersion can also produce anomalous screening charge distributions around charged impurities [187]; it will be instructive to investigate the counterpart effects in our strongly correlated models for heavy fermion systems. It has also been shown that the anomalous Hall effect is twofold enhanced when double Weyl nodes are present [191]. Furthermore, since the number of surface state Fermi arcs are determined by the value of the topological invariant, we expect the double Weyl nodes to double the number of Fermi arc surface states between a ± 2 double Weyl pair [191].

The WKSM to Kondo insulator transition comes with a kink in the self-consistency solutions, verifying that the Kondo effect acts differently with different density of states around the Fermi level. Furthermore, the nodes are Kondo pinned to the Fermi energy, through the mechanisms explained in Chapters 3–4. The Zeeman field only reduces the symmetry of the spin degrees of freedom, and leaves the lattice space and point group symmetries unchanged, so they can enforce the nonsymmorphic-Kondo filling constraint.

Our model is not generically analytically tractable, but it shares symmetry and nodal path geometry with those of a previous conduction electron only model [185], albeit with a much larger scale of M_z. Therefore the phase diagram is expected to be similar to the uncorrelated model if ISB m is also tuned. The conduction electron only model has a metallic pocket that is accessible at values of $m > 1$. We predict a stronger value of inversion symmetry breaking in the full Anderson model may then allow a KI-to-metallic or WKSM-to-metallic transition. This model and the WKSM-to-metallic transition is relevant to the magnetic field experiments done on the nonmagnetic $Ce_3Bi_4Pd_3$ [170]. The experiments in that work also found a heavy

Fermi-liquid metallic phase at high field values. That transition is more traditional to the Kondo-insulator physics, and is not the focus of the present work. It is worth noting that, what is nontrivial in our finding is that the topological transitions take place at a Zeeman field scale that is smaller than the Kondo scale, where the Kondo effect itself is suppressed by the Zeeman coupling. In that sense, our result captures the most surprising aspect of the experimental findings.

At very large values of $M_z \gtrsim T_K^0$, the WKSM model no longer supports nonzero r values, meaning the system has undergone a Kondo destruction phase transition. When that happens, a metallic phase ensues. However, this model reproduces the WKSM to KI transition as a function of M_z in $Ce_3Bi_4Pd_3$. It is not clear whether one should expect double Weyl points in $Ce_3Bi_4Pd_3$, but it appears as a generic effect of magnetic field. Future work will explore how to experimentally determine the nodal orders in $Ce_3Bi_4Pd_3$, and, relatedly, to carry out studies in more realistic models for this system.

Chapter 6

Connection to related theoretical work, implications, and discussion

We have stressed that the Weyl-Kondo semimetal solution is robust because of the cooperation of the Kondo effect with the space-group symmetry. We have identified the WKSM as a distinct state of matter: in the bulk, it features strongly renormalized Weyl nodes instead of being fully gapped; on the surface, and it hosts Fermi arcs from a band with a width of the Kondo energy. The focus of the WKSM has been on three dimensional models, but in principle a two-dimensional nonsymmorphic lattice could also harness the Kondo pinning mechanism. In this chapter, the WKSM model as it is presented here is compared with models of topological Kondo insulators, and models that can realize topological semimetals as well.

The context of heavy fermion systems links the WKSM phase advanced here with the topological Kondo insulators (TKI) [57] and the physics of their surface states [196]. It will be instructive to explore Kondo-driven bulk nodal excitations near the Fermi energy in a variety of related models that use the heavy fermion system as a platform for finding topology [61, 140, 141, 197, 198, 199, 59]. Recently, there was a realization of a heavy fermion type Weyl semimetal in a modified TKI model, with an added parity symmetry breaking term incorporated into the odd-form-factor hybridization [200]. The heavy Weyl semimetal develops from the TKI model at half-filling when the hybridization is nonzero, and its surface states show a Kondo destruction transition. The most widely used TKI model is a half-filled Kondo lattice model on a cubic lattice (usually the intersite RKKY term is neglected for simplicity), with conventional conduction electron dispersion and a localized bare

f electron level [57, 56, 201, 198]. The TKI models realize a gapped Kondo insulator with nontrivial surface Dirac nodes. There is also some disagreement as to if the main proposed TKI material candidate (intermediate valence compound SmB_6) is in fact nontrivial, as several works have attempted to settle - for example, Refs. [202, 203].

Additionally, while we have emphasized the space group symmetry to produce WKSM in three dimensions, it is also instructive to consider the role of space group symmetry in two dimensions.

One study looked at a Kondo lattice model on the honeycomb lattice which realizes a Dirac-Kondo semimetal (DKSM) to TKI phase transition at the inclusion of the spin-orbit coupling in the conduction electrons [140]. The correlated DKSM phase could be found in heavy fermion systems in a dilute carrier limit, where the conduction electron band is nearly empty.

As another example, a Shastry-Sutherland Kondo lattice model revealed a partially screened Kondo semimetal phase that breaks a symmetry [204], and its phase diagram was later reconsidered in light of the constraints imposed by nonsymmorphic glide symmetry [141]. Refs. [204, 141] proposed an even-filling Kondo lattice model Luttinger invariant on top of the (often zero) Fermi volume, which if nonzero, hints that the system may compensate with gapless dispersion or fractionalization, and that any finite Fermi surface can only be removed by breaking this glide symmetry (*i.e.* changing the Luttinger invariant to zero). Though the idea of the Fermi volume as a topologically protected object is older [205], this idea of topological 'Luttinger invariants' that can help classify the type of semimetal for nonsymmorphic systems was later generalized [206].

The second remarkable feature of the WKSM is the Kondo pinning mechanism, which constrains the Weyl nodes to the Fermi energy. It has been established that the Kondo pinning mechanism relies on the filling enforcement granted by both the nonsymmorphic symmetry and strong correlations. Since the Kondo-screened phase includes the f electron species in its Luttinger count towards the Fermi volume, it

imposes additional constraints in the Kondo limit; and that nonsymmorphic space group symmetry constrains the filling where gapless semimetals occur. The diamond lattice space group has been shown to be a band insulator for fillings of $\nu = 4n$ where n is a positive integer; this means that the diamond lattice is only a band insulator if it is completely empty or full [90]. The quarter-filling chosen for the WKSM is $\nu = 2n$ with $n = 1$, which would be an even-filled commensurate band insulator if it was symmorphic, however the multiple nonsymmorphic symmetries require extra band crossings and is highly degenerate. Since $\nu = 2n$ is not a band insulator filling, the phase must be gapless with a Fermi surface present, but because any even filling encloses zero Luttinger volume, the Fermi surface can be a point, so the circumstances favor the formation of a nodal semimetal phase. Our work here has provided how such insights, gained from studies of non-interacting electron topology, can cooperate with strong correlations to produce novel correlation-driven electronic topological states.

Local moments are also the key to exploring the magnetic parts of the heavy fermion global phase diagram, as well as taking magnetic fluctuations into account. In quantum phase transitions, the local moment fluctuations near a magnetic phase boundary drive emergent phases to develop. Physically, this is the origin of our view that the f electrons of the system drive topology; in the presence of spin orbit coupling, these fluctuations can also cause topological phases to emerge. There have been few examples of a magnetically ordered phase that is also a topological electronic state, though theoretical studies have been more abundant. For example, in a study of magnetic Weyl Kondo semimetals, heterostructures of SmB_6 and AB_6 (A is a magnetic rare earth elements) were found to favor Dirac or Weyl semimetal states depending on whether the A moments ordered antiferromagnetically or ferromagnetically, respectively [197].

This thesis has made the contribution of exploring the paramagnetic, highly frustrated region of the global phase diagram, and the paramagnetic heavy fermi liquid approaching the border of a magnetic phase in the global phase diagram including

spin orbit interaction. A new appreciation for the significance of spin orbit coupling and its realistic modeling has been promoted here, and its contribution to topology cannot be understated due to the need for band inversion. There is also a recognition that because a strong Kondo screening can indirectly change the Luttinger count, and consequently the local moments control the topological properties connected to the Fermi surface through the Kondo effect. This is an encouraging sign that topology and heavy fermion properties interplay in surprising ways, and that there is much more to explore within their intersection.

Chapter 7

Summary

This thesis has considered heavy fermion systems, which comprises a system with delocalized electrons interacting with magnetic localized fermions, and possesses competing paramagnetic heavy Fermi liquid and antiferromagnetic metallic ground states. The quantum phase transitions between these phases are determined by the degree of magnetic frustration and the small-large Kondo Fermi surface energy scale, organized in the global phase diagram. However, the spin orbit coupling in real heavy fermion systems is substantial enough to warrant inclusion in models, and naturally offers a way to connect Kondo physics to topological phases. Topological metals and semimetals are natural states to investigate in the heavy fermion systems, since the finite Fermi surface is amenable to transport and thermodynamic measurements, and are highly tunable in general. This makes heavy fermion systems an ideal platform to study the intersection of topology and quantum phase transitions.

Inspired by the many fascinating studies of the pyrochlore iridate $Pr_2Ir_2O_7$, we study a pair of two-dimensional Kondo lattice models hosting f fermions in a TRSB chiral spin liquid state, and calculate the anomalous Hall response as a function of Kondo coupling. In the paramagnetic region of the global phase diagram, the small-to-large Fermi surface transition marks when the local moments must be included in the Luttinger count due to Kondo screening. The Luttinger count includes only conduction electrons in the small Fermi surface phase, and the large Fermi surface phase counts them and the localized moment spins per unit cell; however the Luttinger count is modulo even numbers of electrons. The anomalous Hall signal originates from the Berry curvature on the Fermi surface, and it is used to probe and compare

a pair of two-dimensional lattices. For the 2 spin per unit cell square $J_1 - J_2$ lattice in a nontrivial flux state, the AHE evolved smoothly across the small-large Fermi surface transition since the Luttinger count changed by an even number of spins; interestingly, the Fermi surface itself is invariant across the transition. In contrast, the model implemented on the three spin per unit cell kagomé lattice produces a large jump in the AHE across the small-large Fermi surface transition, accompanied by a reconstruction of the Fermi surface topology and Fermi volume.

Contemporaneously with the new materials realizations of Weyl semimetals and the Weyl-Kondo semimetal candidate $Ce_3Bi_4Pd_3$, a periodic Anderson model with spin orbit coupling and broken inversion symmetry that theoretically realizes the WKSM phase in the Kondo limit. The WKSM phase is characterized by Kondo pinning, renormalized narrow linearly dispersing bands with a slow Weyl fermion velocity which enhances the specific heat, and the specific heat having an orders of magnitude enhanced T^3 specific heat prefactor which onsets below the Kondo temperature.

What underlies the WKSM solution is the cooperation between strong correlations and space-group symmetry constraint, which we have developed in considerable depth. The symmetry mechanisms for node formation are explained, beginning with a 'natural' nodal line semimetal phase of conduction electrons, as a consequence of the nonsymmorphic space group operations creating degeneracy at the zone boundary. Adding band inversion by including spin orbit coupling produces a Dirac semimetal state with pseudospin degrees of freedom; this becomes a Weyl semimetal when sublattice exchange symmetry is violated by broken inversion symmetry, with the Dirac cone splitting into two pairs of nodes each. Before turning on hybridization, the f fermions of the model are in a trivial insulator phase, and the conduction electrons bands are empty. In the strong coupling Kondo limit, the hybridization allows the f fermion to form mobile quasiparticles, which take on a narrow, renormalized version of the nodal dispersion allowed by symmetry: nodal Kondo line semimetal, Dirac

Kondo semimetal and Weyl-Kondo semimetal phases are accessible.

The Kondo pinning mechanism is shown to result from a combination of factors:

- The nonsymmorphic symmetry causes certain commensurate energy band fillings to be gapless, rather than a trivial band insulator, and protects the degeneracies it creates against SOC and other perturbations;
- The solution in the Kondo limit is constrained such that the number of f fermions in the unit cell is one per site;
- At quarter filling, the filling constraint and the nonsymmorphic symmetry enforced gapless filling occur between the same bands.

A tilting modification to the WKSM that preserves lattice symmetry is also presented, which can shift the balance of net Berry curvature near a Weyl node singularity. The tilting is suggested to enhance the spontaneous Hall signal from Weyl semimetals, suggesting that the large spontaneous Hall effect measured in $Ce_3Bi_4Pd_3$ may have similarly tilted Weyl-Kondo nodes.

An important advantage provided by strong correlations is the high tunability, and we have illustrated this point by considering the effect of a Zeeman field to the WKSM solution. A Zeeman field is implemented on the localized f fermions in the WKSM model, and a phase diagram is mapped out, where three distinct WKSM phases are accessible before a gap is opened. The original WKSM phase is chosen as a starting point, but when the Zeeman field is turned on and time reversal symmetry is broken, the nodes begin to move back together until they meet in a quadratic band touching on the Brillouin zone boundary. As the Zeeman field is increased beyond a critical value, double-Weyl fermions emerge from the touching point to the interior of the Brillouin zone, and with higher magnetic field, four more node pairs emerge in the Brillouin zone. All nodes then converge into a non-Kramers quadratic band touching point at the Brillouin zone center, before opening a gap in a phase transition

to a Kondo insulator. These results are consistent with magnetic field studies on $Ce_3Bi_4Pd_3$ which found a WKSM to Kondo insulator phase transition [170].

The study presented in this thesis opens up new frontiers in the exploration of the interplay between strong correlations and electronic topology. For example, the inclusion of magnetism into topological quantum materials has long been a goal, and the works shown here have taken strides to investigate the nonmagnetic and paramagnetic aspects of heavy fermion topology. This leaves the magnetic phases and their phase transitions to explore in the topological global phase diagram.

Appendix A: anomalous Hall effect and quantum criticality in geometrically frustrated heavy fermion metals

A1 Chiral interaction from perturbative expansion

To obtain Eq. 2.5 of Chapter 2, we integrate out the f-spinons from Eqs. 2.1-2.2 of Chapter 2 in the Kondo destroyed phase using the standard Feynman diagram procedure. Guided by the symmetry analysis, we only need to consider the third-order term $1/3!(\boldsymbol{s}_i \cdot \boldsymbol{S}_i)(\boldsymbol{s}_j \cdot \boldsymbol{S}_j)(\boldsymbol{s}_k \cdot \boldsymbol{S}_k)$. The effective chiral electronic interaction H_{cc} is obtained by contracting the spinons in triangle-loop diagrams as shown Fig. (A1). Since the CSL is gapped, it is sufficient to restrict to the most local three-site loops, i.e. the triangle within a unit cell, at equal time only. Then we can obtain H_{chiral} as

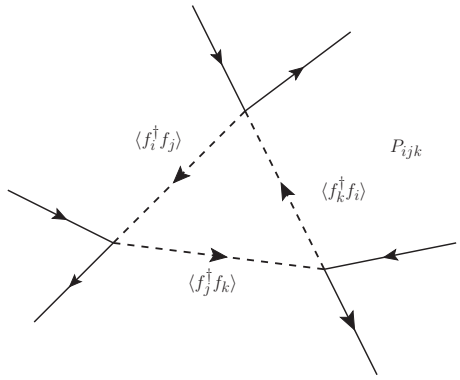

Figure A1 : Feynman diagrams of the triangle-loop contractions. The solid lines are the propagators for the conduction electrons.

follows:

$$
\begin{aligned}
&(\boldsymbol{s}_i \cdot \boldsymbol{S}_i)(\boldsymbol{s}_j \cdot \boldsymbol{S}_j)(\boldsymbol{s}_k \cdot \boldsymbol{S}_k) = \sum_{a,b,c} s_i^a s_j^b s_k^c \\
&\times \frac{1}{8}(f^\dagger_{i\alpha_i}\sigma^a_{\alpha_i\beta_i} f_{i\beta_i} f^\dagger_{j\alpha_j}\sigma^b_{\alpha_j\beta_j} f_{j\beta_j} f^\dagger_{k\alpha_k}\sigma^c_{\alpha_k\beta_k} f_{k\beta_k}) \\
&\underset{\rightarrow}{\triangle} \sum_{a,b,c} s_i^a s_j^b s_k^c (\langle f^\dagger_{i\alpha_i} f_{j\beta_j}\rangle\langle f^\dagger_{j\alpha_j} f_{k\beta_k}\rangle\langle f^\dagger_{k\alpha_k} f_{i\beta_i}\rangle \\
&+ \langle f^\dagger_{i\alpha_i} f_{k\beta_k}\rangle\langle f^\dagger_{k\alpha_k} f_{j\beta_j}\rangle\langle f^\dagger_{j\alpha_j} f_{i\beta_i}\rangle)\sigma^a_{\alpha_i\beta_i}\sigma^b_{\alpha_j\beta_j}\sigma^c_{\alpha_k\beta_k} \\
&= E_{ijk}\boldsymbol{s}_i \cdot (\boldsymbol{s}_j \times \boldsymbol{s}_k)/2,
\end{aligned}
\tag{A-1}
$$

where $\underset{\rightarrow}{\triangle}$ denotes triangular-loop contraction. The constraction is approximated by equal-time correlators, so $\langle f^\dagger_{i\alpha_i} f_{j\beta_j}\rangle = \delta_{\alpha_i,\beta_j}\chi_{ij}$. Discarding the density-density interactions, the second line of Eq. (A-1) can be written as

$$
\begin{aligned}
H_{\text{chiral}} \sim \sum_{\alpha_l,\alpha_j,\alpha_k} &(P_{ljk} d^\dagger_{l\alpha_k} d_{l\alpha_l} d^\dagger_{j\alpha_l} d_{j\alpha_j} d^\dagger_{k\alpha_j} d_{k\alpha_k} \\
&+ P_{lkj} d^\dagger_{l\alpha_j} d_{l\alpha_l} d^\dagger_{k\alpha_l} d_{k\alpha_k} d^\dagger_{j\alpha_k} d_{j\alpha_j}).
\end{aligned}
\tag{A-2}
$$

H_{chiral} of the Kondo Screened Phase

In order to obtain the spectral weight of the incoherent terms in the Kondo screened phase, we use the slave rotor theory[207] to tackle the f-fermion Hubbard model. As we shall briefly discuss below, the Kondo transition *is* the Mott transition for f-fermions in periodic Anderson model (PAM)[208], and is realized when the rotor fields are condensed. The condensation density describes the coherent charge degrees of freedom that would contribute to transport.

The PAM Hamiltonian is

$$
H_{\text{PAM}} = H^{(f')}_{\text{Hubbard}} + H^{(d)}_0 + V\sum_{i,\sigma}(f'^\dagger_{i,\sigma} d_{i,\sigma} + f'_{i,\sigma} d^\dagger_{i,\sigma}),
\tag{A-3}
$$

where

$$
H^{(f')}_{\text{Hubbard}} = -\sum_{ij,\sigma} t_{ij} f'^\dagger_{i,\sigma} f'_{j,\sigma} + U\sum_{i,\sigma,\sigma'} n^{(f')}_{i,\sigma} n^{(f')}_{i,\sigma'}
\tag{A-4}
$$

is the usual half-filled Hubbard model, and

$$H_0^{(d)} = -\sum_{ij,\sigma} t_{ij} d^\dagger_{i,\sigma} d_{j,\sigma} \tag{A-5}$$

describes the free d-band electrons.

First, we use the slave rotor formalism to treat the Hubbard model part by letting $f'_i \to f_i e^{-i\theta_i}$

$$H^{(f')} \to \frac{U}{2}\sum_{i,\sigma} \hat{L}^2_{i,\sigma} - \sum_{ij,\sigma}(t_{ij} f^\dagger_{i,\sigma} f_{j,\sigma} e^{i(\theta_i-\theta_j)} + h.c.). \tag{A-6}$$

The corresponding Lagrangian is

$$\begin{aligned} S_H = \int d\tau \sum_{i,\sigma} f^\dagger_{i,\sigma}\partial_\tau f_{i,\sigma} + \frac{(\partial_\tau\theta)^2}{2U} + \\ \sum_{\langle ij\rangle,\sigma} (t_{\langle ij\rangle} f^\dagger_{i,\sigma} f_{j,\sigma} e^{i(\theta_i-\theta_j)} + h.c.), \end{aligned} \tag{A-7}$$

here the kinetic energy of the rotors $\frac{U}{2}\sum_{i,\sigma}\hat{L}^2_{i,\sigma}$ is replaced by its conjugate variables $\hat{L}_{i,\sigma} = (\partial_\tau\theta + ih)/U$.

Let $e^{i\theta_i} = X_i$, so that X_is subject to the constraint $|X_i|^2 = 1$ on average (using Lagrangian multiplier). Using $\partial_\tau\theta_i = \frac{1}{i}X_i^*\partial_\tau X_i$, we have

$$S_H = S^0_X + S^0_f + \sum_{\langle ij\rangle,\sigma} (t_{\langle ij\rangle} f^\dagger_{i,\sigma} f_{j,\sigma} X_i X_j^* + h.c.). \tag{A-8}$$

with $S^0_f = \int d\tau \sum_{i,\sigma} f^\dagger_{i,\sigma}\partial_\tau f_{i,\sigma}$, and $S^0_X = \sum_i (\frac{|\partial_\tau X_i|^2}{2U} + \lambda_i(|X_i|^2 - 1))$. The exchange term is also expressed in terms of slave rotors

$$H_{\text{exc}} = V\sum_{i,\sigma}(f^\dagger_{i,\sigma} d_{i,\sigma} X_i + h.c.). \tag{A-9}$$

In the large-U-small-V limit, the system is in P_S phase. We can integrate out the rotor fields, and recover both the Heisenberg-J interaction, as well as the Kondo coupling

$$H_K = J_K \sum_i \boldsymbol{S}_f(i)\cdot\boldsymbol{s}_d(i), \tag{A-10}$$

where $J_K = 4V^2/U$.

Within the slave rotor approach, the onset of Kondo screening is described by the condensation of the X-field: $X_i \to X_i^0 + X_i'$. The exchange term becomes

$$H_{exc} = \sum_{i,\sigma} (V X_i^0 f_{i,\sigma}^\dagger d_{i,\sigma} + V X_i' f_{i,\sigma}^\dagger d_{i,\sigma} + h.c.). \tag{A-11}$$

The first term is the hybridazation term, which is equivalent to that of the Kondo model. We can identify that $\rho_K = V X_i^0 / J_K = \frac{U}{4V} X_i^0$. The second term now provides the incoherent fluctuations, which, as we argue in Chapter 2, can mediate the same chiral interactions for the d-electrons through the triangular diagrams. But in this approach, the X-field satisfies a spectral sum rule: $\int d\nu d^2k/(2\pi)^3 G_X(\nu; \mathbf{k}) = 1$, from which we can obtain that in the Kondo screened phase

$$H_{\text{chiral}} = \left(1 - \frac{4J_K}{U}\rho_K^2\right)^3 \frac{J_K^3}{2} E_{ijk} \boldsymbol{s}_i \cdot (\boldsymbol{s}_j \times \boldsymbol{s}_k). \tag{A-12}$$

Note that the prefactor $4J_K/U$ is changing as we tune J_K. In our calculation, we fix $U = 16t$, i.e. twice as the d-electron's bandwidth.

Hubbard-Stratonovich transformation of H_{chiral}

To decouple the six-fermion chiral interaction, in general we need to introduce two sets of Hubbard-Stratonovich (HS) fields, namely, γs, κs, which can be interpreted as a single bond / two consecutive bonds fields:

$$\gamma_{ij} \quad = \langle \textstyle\sum_\alpha d_{i,\alpha}^\dagger d_{j,\alpha} \rangle, \tag{A-13}$$

$$\kappa_{ij,k} \quad = \langle \textstyle\sum_{\alpha,\beta} d_{i,\alpha}^\dagger d_{k,\alpha} d_{k,\beta}^\dagger d_{j,\beta} \rangle, \tag{A-14}$$

which are in principle independent. The bond indices here are directional, i.e. $\gamma_{ji} = \gamma_{ij}^*$, $\kappa_{ji,k} = \kappa_{ij,k}^*$. In general, we have 6 complex γ's and 12 complex κ's.

The HS transformation is as follows

$$L_{\text{HS}} = \sum_{\mathbf{x}} (d_{\mathbf{x}}^\dagger (i\partial_t + \mu) d_{\mathbf{x}} - \widetilde{\Psi}^* \mathcal{M} \Psi + J^\dagger \Psi + \widetilde{\Psi}^* J - H_{\text{kin}}), \tag{A-15}$$

where $\widetilde{\Psi}^* = \{\kappa^*_{\mathbf{x}_i\mathbf{x}_j,k}, \ldots \kappa^*_{\mathbf{x}_i\mathbf{x}_j,\bar{k}}, \ldots, \gamma^*_{\mathbf{x}_i\mathbf{x}_j}, \ldots, \gamma^*_{\mathbf{x}_j\mathbf{x}_i}, \ldots\}$ is a 24-component vector. The indices $i-j$ run over all the links inside a unit cell given by $\mathbf{x}$, and $\{k, \bar{k}\}$ denote the other two sites for a given bond $\langle ij\rangle$ within the unit cell.

$$J^\dagger = \{\hat{\gamma}^\dagger_{ij}, \hat{\gamma_{ji}}^\dagger, \ldots, \kappa^\dagger_{ij,k}, \hat{\kappa}^\dagger_{ij,\bar{k}}, \ldots\}. \tag{A-16}$$

where we use $\hat{\gamma}^\dagger_{ij} = \sum_\alpha d^\dagger_{\mathbf{x}_j,\alpha} d_{\mathbf{x}_i,\alpha}$, $\hat{\kappa}^\dagger_{ij,k} = \sum_{\alpha,\beta} d^\dagger_{j,\alpha} d_{k,\alpha} d^\dagger_{k,\beta} d_{i,\beta}$.

To determine $\mathcal{M}$, suppose that we now integrate out all the HS fields, we should recover the effective interactions as

$$H_{eff-int} = J^\dagger \mathcal{M}^{-1} J = H_{\rm cc} + \ldots, \tag{A-17}$$

in which the $\ldots$ indicates other effective interactions. To have a stable HS transformation, we need to further include the 4-fermion effective interactions at $H^{(2)}_{eff-int} \sim \mathcal{O}(J_K^2)$ generated from $J_K^2(\boldsymbol{s}_i \cdot \boldsymbol{S}_i)(\boldsymbol{s}_j \cdot \boldsymbol{S}_j)$ as well as the 8-fermion process at $H^{(4)}_{eff-int} \sim \mathcal{O}(J_K^4)$. Since the f-fermions are gapped, we can keep only the short-range terms, i.e. within a unit cell, so that all the terms can be decoupled by the $\hat{\gamma}_{ij}$s and $\hat{\kappa}_{ij}$s in the large-N limit. Then $\mathcal{M}^{-1}$ can be written in a block form $\mathcal{M}^{-1} = \oplus(\mathcal{M}^{-1}_{(ij)})$, where $(\mathcal{M}^{-1}_{(ij)})$ is a 4×4 matrix for a given bond (ij) within the unit cell.

Here we estimate the matrix elements of $(\mathcal{M}^{-1}_{(ij)})$ within the approximations that are used for computing $H_{\rm chiral}$, i.e. equal-time contraction is used and only those within a unit cell are included:

$$(M^{-1})_{\hat{\gamma}^\dagger\hat{\gamma},(ij)} = J_K^2 {\rm sgn}[(ij)] \chi_{ij}\chi_{ji}/2! = \rho_{ij}^2, \tag{A-18}$$

$$(M^{-1})_{\hat{\kappa}\hat{\gamma},(ij)k} = J_K^3 P_{ijk}/(2 \times 3!), \tag{A-19}$$

$$(M^{-1})_{\hat{\kappa}^\dagger\hat{\kappa},(ij),kk'} = \delta_{k,k'} J_K^4 \rho_{ij}^4/4!. \tag{A-20}$$

${\rm sgn}[\langle ij\rangle]$ is a relative sign coming from the fact that $\hat{\gamma_{ij}}^\dagger \hat{\gamma_{ij}} \sim -\hat{\gamma_{ji}}^\dagger \hat{\gamma_{ji}}$. We see that $\det[M^{-1}]$ is indeed positive, and hence this is a stable HS transformation. $\mathcal{M}$ is then obtained by inversing $\mathcal{M}^{-1}$.

Therefore, we have a formal HS decoupling of $H_{\rm chiral}$. Further replacing the HS-fields by their expectation values in Eq. (A-15), we obtain both fermion bilinears

and four-fermion terms. To lower the total energy, we need to have $\gamma_{ij}\kappa^*_{ij,k} \sim -P_{ijk}$. Upon satisfying this constraint, we have an additional gauge degree of freedom to choose either $\gamma_{d,ij}$ or $\kappa^*_{ij,k}$ to be imaginary, i.e. explicitly breaking TRS, even though the underlying physical state is the same. For convenience, we can choose $\kappa^*_{ij,k}$s which couple to d-fermion bilinears ($\hat{\gamma}_{ij}$s) to be TRSB. By keeping only the TRSB terms in Eq. (A-15), we justify our choice of Eq. 2.8 in Chapter 2 as

$$H_{d,1} = \sum_{\langle ij \rangle, k} (\kappa^*_{ij,k}\hat{\gamma}_{ij} + h.c.). \tag{A-21}$$

A2 Berry curvature, Berry connection, Streda formula and Kubo formula

The AHE coefficient, σ_{xy}, presented in Chapter 2 are computed using the Streda formula:

$$\begin{aligned}\sigma_{xy} &= \int \frac{d\mathbf{k}}{(2\pi)^2} \sum_n \mathcal{F}^{xy}_n(\mathbf{k}) f(\epsilon_n(\mathbf{k})) \\ &= \sum_{n \neq n'} \int \frac{d\mathbf{k}}{(2\pi)^2} [f(\epsilon_n(\mathbf{k})) - f(\epsilon_{n'}(\mathbf{k}))] \\ &\times \mathrm{Im} \frac{\langle n, \mathbf{k}|v_x(\mathbf{k})|n', \mathbf{k}\rangle \langle n', \mathbf{k}|v_y(\mathbf{k})|n, \mathbf{k}\rangle}{[\epsilon_n(\mathbf{k}) - \epsilon_{n'}(\mathbf{k})]^2} \quad .\end{aligned} \tag{A-22}$$

Here, $v_a(\mathbf{k}) = \partial_a H_d(\mathbf{k})$ is the current operator of the conduction electrons, $\mathcal{F}^{xy}_n(\mathbf{k})$ the Berry curvature, and $f(\epsilon_n(\mathbf{k}))$ the Fermi function. Both $\hbar$ and e have been taken to be 1.

To discuss the role of the Berry curvature, we start from the more standard Kubo formula. The current operators are

$$\boldsymbol{J_q} = \frac{1}{\sqrt{N}} \sum_{\mathbf{k}} c^\dagger_{\mathbf{k}+\boldsymbol{q}/2} \frac{\partial H_k}{\partial \mathbf{k}} c_{\mathbf{k}-\boldsymbol{q}/2}. \tag{A-23}$$

In frequency-momentum space, the conductivity is computed via the current-current

correlation function

$$\pi_{ab}(i\nu) = \sum_{\omega} \int \frac{d^2k}{(2\pi)^2} \mathrm{Tr}\Big[\frac{\partial H}{\partial k_a} \times G(\omega - \nu, \mathbf{k} - \boldsymbol{q}/2)\frac{\partial H}{\partial k_b} G(\omega, \mathbf{k} + q/2)\Big], \tag{A-24}$$

where the sum over ω is Matsubara sum.

$$\sigma_{ab} = \lim_{\omega \to 0} \Big[- \mathrm{Im}[\pi_{ab}(i\nu)/\nu\big|_{i\nu \to \omega + i0^+}]\Big]. \tag{A-25}$$

For convenience, it is better to write both G and H in terms of the bloch bands projection operators $P_n(\mathbf{k}) = |n, \mathbf{k}\rangle\langle n, \mathbf{k}|$ (which is possible for fermion bilinear theory) with $\rangle n, \mathbf{k}$ being the eigenvectors of nth band at momentum $\mathbf{k}$:

$$H(\mathbf{k}) \quad = \textstyle\sum_n \epsilon_n(\mathbf{k}) P_n(\mathbf{k}), \tag{A-26}$$

$$G(\omega, \mathbf{k}) \quad = \textstyle\sum_n \frac{P_n(\mathbf{k})}{i\omega - \epsilon_n(\mathbf{k})}. \tag{A-27}$$

After inserting the expression into Eq. (A-24), we find only the following term contributes

$$\begin{aligned} \pi_{ab}(i\nu) &= \sum_{\omega} \int \frac{d^2k}{(2\pi)^2} \sum_{n_0,\ldots,n_3} \mathrm{Tr}\Big[\partial_{k_a} P_{n_0} \\ &\times P_{n_1} \partial_{k_b} P_{n_2} P_{n_3} \frac{\epsilon_{n_0}\epsilon_{n_2}}{(i(\omega - \nu) - \epsilon_{n_1})(i\omega - \epsilon_{n_3})}\Big] \\ &= \int \frac{d^2k}{(2\pi)^2} \sum_{n_0,\ldots,n_3} \mathrm{Tr}\Big[\partial_{k_a} P_{n_0} \\ &\times P_{n_1} \partial_{k_b} P_{n_2} P_{n_3} \frac{\epsilon_{n_0}\epsilon_{n_2}(f(\epsilon_{n_3}) - f(\epsilon_{n_1}))}{i\nu + \epsilon_{n_3} - \epsilon_{n_1}}\Big]. \end{aligned} \tag{A-28}$$

Here $f(\epsilon)$ is the Fermi distribution function, and arises from the Matsubara sum. Sum of n_i runs over band indices. After performing the Tr operation, we end up with the following result

$$\begin{aligned} \pi_{ab}(i\nu) = \int \frac{d^2k}{(2\pi)^2} \sum_{n,n'} \Big[&- A^a_{nn'} A^b_{n'n} \frac{f(\epsilon_n) - f(\epsilon_{n'})}{i\nu + \epsilon_n - \epsilon_{n'}} \epsilon_n \epsilon_{n'} \\ &+ A^a_{nn'} A^{b*}_{n'n} \frac{f(\epsilon_n) - f(\epsilon_{n'})}{i\nu + \epsilon_n - \epsilon_{n'}} \epsilon^2_{n'} + A^{a*}_{nn'} A^b_{n'n} \frac{f(\epsilon_n) - f(\epsilon_{n'})}{i\nu + \epsilon_n - \epsilon_{n'}} \epsilon^2_{n} \\ &- A^{a*}_{nn'} A^{b*}_{n'n} \frac{f(\epsilon_n) - f(\epsilon_{n'})}{i\nu + \epsilon_n - \epsilon_{n'}} \epsilon_n \epsilon_{n'} \Big], \end{aligned} \tag{A-29}$$

where $A^a_{n,n'} = -i\langle n|\partial_{k_a} n'\rangle$, $A^{a*}_{n,n'} = -i\langle \partial_{k_a} n|n'\rangle$ is the matrix element of ∂_{k_a}. Note only the diagonal elements are the Berry connection. Then we do analytic continuation $i\nu \to \omega + i\eta$, and take the imaginary part of $\pi_{ab}(\omega)/\omega$. In the end, we let $\omega \to 0$. When we take imaginary part of $\pi_{ab}(\omega)/\omega$, we have two different contributions:

$$\begin{aligned}\pi^{(1)}_{ab} = \int \frac{d^2k}{(2\pi)^2} \sum_{n,n'} \Big(&\mathrm{Im}[-A^a_{nn'} A^b_{n'n}] \\ &\times \mathrm{Re}[\frac{f(\epsilon_n) - f(\epsilon_{n'})}{\omega + \epsilon_n - \epsilon_{n'} + i\eta} \epsilon_n \epsilon_{n'}] + \dots \Big),\end{aligned} \tag{A-30}$$

$$\begin{aligned}\pi^{(2)}_{ab} = \int \frac{d^2k}{(2\pi)^2} \sum_{n,n'} \Big(&\mathrm{Re}[-A^a_{nn'} A^b_{n'n}] \\ &\times \mathrm{Im}[\frac{f(\epsilon_n) - f(\epsilon_{n'})}{\omega + \epsilon_n - \epsilon_{n'} + i\eta} \epsilon_n \epsilon_{n'}] + \dots \Big),\end{aligned} \tag{A-31}$$

where $\dots$ denotes the rest three terms. Note that $A^a_{nn'} = -A^{a*}_{nn'}$, $(A^a_{nn'})^* = A^{a*}_{n'n}$, we find

$$\begin{aligned}\pi^{(1)}_{ab} &= \int \frac{d^2k}{(2\pi)^2} \sum_{n,n'} \Big(\mathrm{Im}[-A^a_{nn'} A^b_{n'n}](f(\epsilon_n) - f(\epsilon_{n'})) \\ &\times \mathrm{Re}[\frac{(\epsilon_n - \epsilon_{n'})^2}{\omega + \epsilon_n - \epsilon_{n'} + i\eta} + \frac{(\epsilon_n - \epsilon_{n'})^2}{\omega - \epsilon_n + \epsilon_{n'} + i\eta}] \\ &= \int \frac{d^2k}{(2\pi)^2} \sum_{n,n'} \Big(\mathrm{Im}[-A^a_{nn'} A^b_{n'n}](f(\epsilon_n) - f(\epsilon_{n'})) \\ &\times \frac{2\omega(\epsilon_n - \epsilon_{n'})^2}{\omega^2 - (\epsilon_n - \epsilon_{n'})^2}.\end{aligned} \tag{A-32}$$

Therefore, after taking the limit $\pi^{(1)}_{ab}/\omega|_{\omega\to 0}$, we obtain

$$\sigma^{(1)}_{ab} = \int \frac{d^2k}{(2\pi)^2} \sum_{n\neq n'} \mathrm{Im}[A^a_{nn'} A^b_{n'n}](f(\epsilon_n) - f(\epsilon_{n'})), \tag{A-33}$$

which we can use the relation $\langle n|\partial_{k_a} H(k)|n'\rangle = (\epsilon_n - \epsilon_{n'}) A^a_{nn'} + \delta_{n,n'} \partial_{k_a} \epsilon_n$ to transform into the Streda formula. For $\pi^{(2)}_{ab}/\omega|_{\omega\to 0}$,

$$\mathrm{Im}[\frac{f(\epsilon_n) - f(\epsilon_{n'})}{\omega + \epsilon_n - \epsilon_{n'} + i\eta}] = \delta_{n,n'} \delta(\omega) \frac{f(\epsilon_n) - f(\epsilon_n + \omega)}{\omega}|_{\omega\to 0}. \tag{A-34}$$

Note that for $n \neq n'$, the factor is immediately zero when we take $\eta \to 0$. Only $n = n'$ terms survive, and $\pi^{(2)}_{ab}/\omega|_{\omega\to 0} \sim \delta(\omega)\partial f(\epsilon)/\partial\epsilon$. For $a \neq b$, $\mathrm{Re}[A^a_{nn} A^b_{nn}]$ is symmetric

upon exchanging $a \leftrightarrow b$. On the other hand, we know $\pi_{ab} = -\pi_{ba}$. Therefore, $\pi^{(2)}_{ab} = 0$ for $a \neq b$. When $a = b$, we recover the usual Kubo formula result of dc conductivity $\sigma_{xx} \sim \delta(\omega)$.

To show that σ^{AH}_{xy} is a Fermi surface property[25], we can rewrite Eq. (A-33) through an integration by part, and make use the fact [209] that $\sum_{n'} \mathrm{Im}[A^a_{nn'} A^b_{n'n}] = \nabla^a_{\mathbf{k}} A^b_{nn} - \nabla^b_{\mathbf{k}} A^a_{nn}$:

$$\begin{aligned}
\sigma^{(1)}_{ab} &= \int \frac{d^2k}{2\pi^2} \sum_n f(\epsilon_n)(\nabla^a_{\mathbf{k}} A^b_{nn} - \nabla^b_{\mathbf{k}} A^a_{nn}) \\
&= \int \frac{d^2k}{2\pi^2} \sum_n (A^b_{nn} \nabla^a_{\mathbf{k}} f(\epsilon_n) - A^a_{nn} \nabla^b_{\mathbf{k}} f(\epsilon_n)) \\
&= \sum_n \frac{1}{2\pi^2} \oint A^a_n(\mathbf{k}_F) d\mathbf{k}_{Fa}.
\end{aligned} \tag{A-35}$$

A3 Berry curvature distribution

The Berry curvature distributions are shown in Fig. (A2) for P_S phase (2(a)) and P_L phase (2(b))) the square lattice model, P_S phase (2(c)) and P_L phase (2(d)) of the kagomé lattice model. For (2(a)) and (2(b)), despite the visual resemblance, their difference is still significant as shown in Fig. 2.3(a).

A4 Reconstruction of Fermi Surfaces

We note that in the Kondo-destroying P_S phase, only conduction electrons participate in forming the Fermi surface. By contrast, in the Kondo-screened P_L phase, both the conduction electrons and local f-moments are involved in forming the Fermi surface [205]. In the case of the $J_1 - J_2$ model, the spinon excitations of the CSL phase are gapped. By contrast, in the Kagomé case, they are gapless.

To illustrate the point, we show the projected density of states (DOS) in Fig. (A3). The parent spinon TRSB flux state is gapped at zero energy (referred to as "E_F") for the $J_1 - J_2$ case, but is gapless at E_F for the Kagomé case. The DOS structure of the spinons survives the P_L phase (bottom row), but are constrained to straddle E_F.

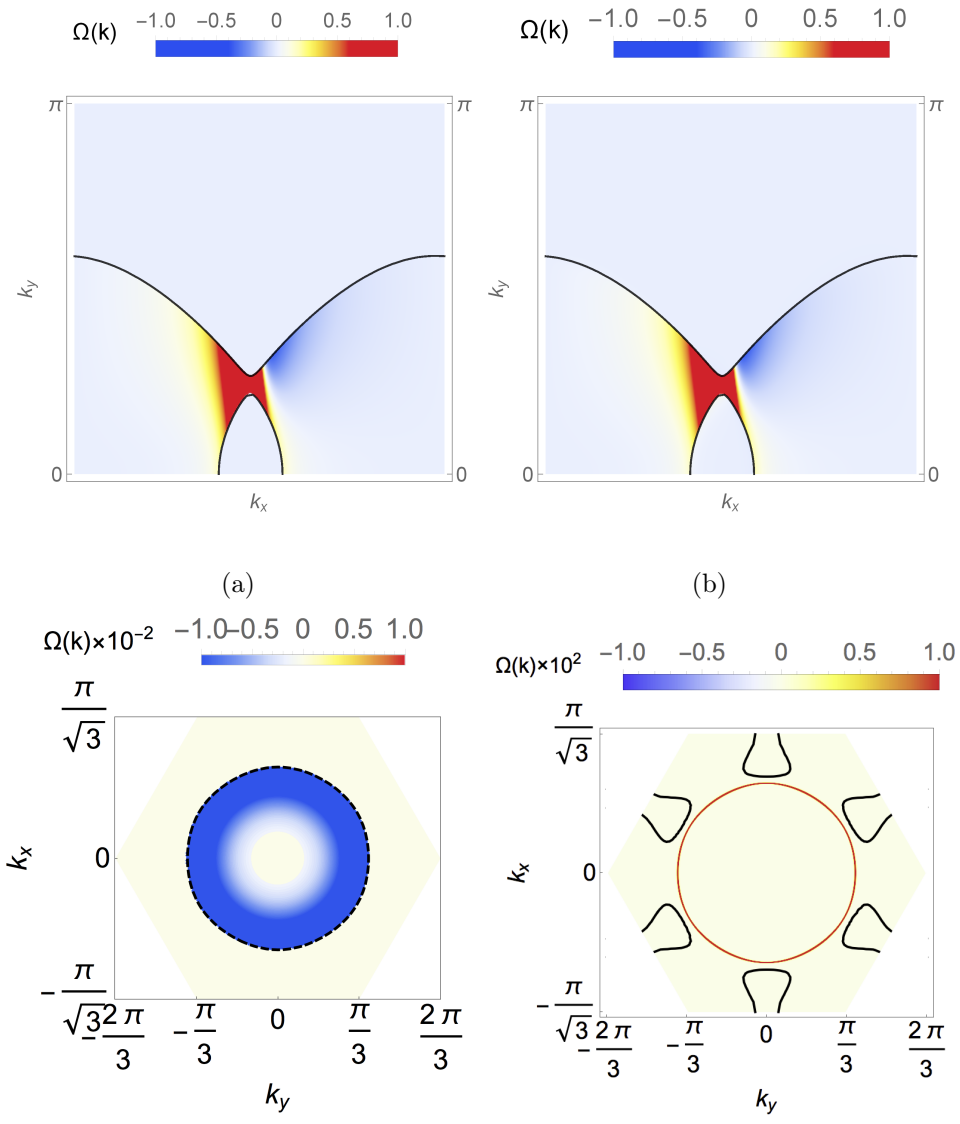

Figure A2 : (Color online) The Berry curvature distributions for the square lattice model P_S phase (2(a)), P_L phase (2(b)), the Kagomé lattice model P_S phase (2(c)) and P_L phase (2(d)). The Fermi surfaces are also shown as black dashed lines.

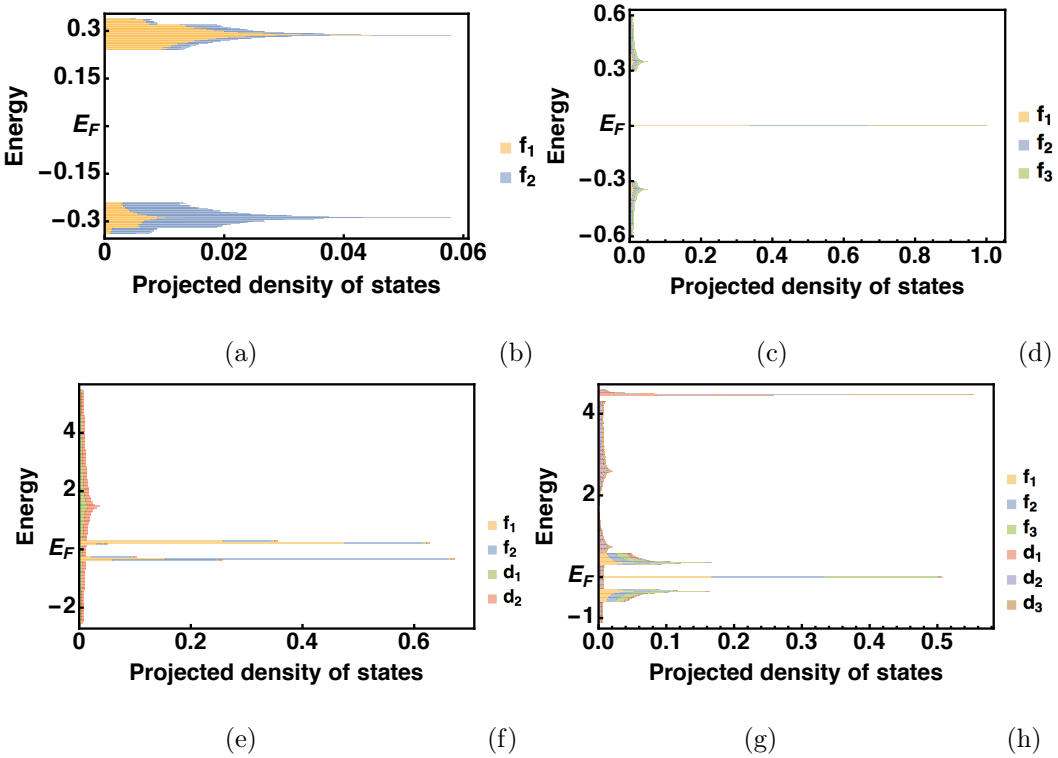

Figure A3 : Density of states projected to the sites of a unit cell, for (a) $J_1 - J_2$ spinons in CSL state, (c) kagomé spinons in $(\frac{\pi}{2}, -\pi)$ state, (e) Kondo screened phase of $J_1 - J_2$ model, (g) Kondo screened phase of Kagomé model; (b),(d),(f),(h) show the relevant legends for color corresponding to the original eigenfunction elements.

The Fermi surface is only affected in the Kagomé lattice.

This can be seen by directly plotting the Fermi surfaces. Fig. (A4) shows both the Kondo-destroyed and the Kondo-screened phases, for both the square lattice and the Kagomé lattice. It is clearly seen that, for the $J_1 - J_2$ model on the square lattice, the Fermi surface smoothly evolves through the QCP. By contrast, for the Kagomé lattice, the Fermi surface experiences a sudden jump across the QCP. We also note that the jump is very substantial. This is because, in the Kagomé CSL state, the middle spinon band happens to be a flat band.

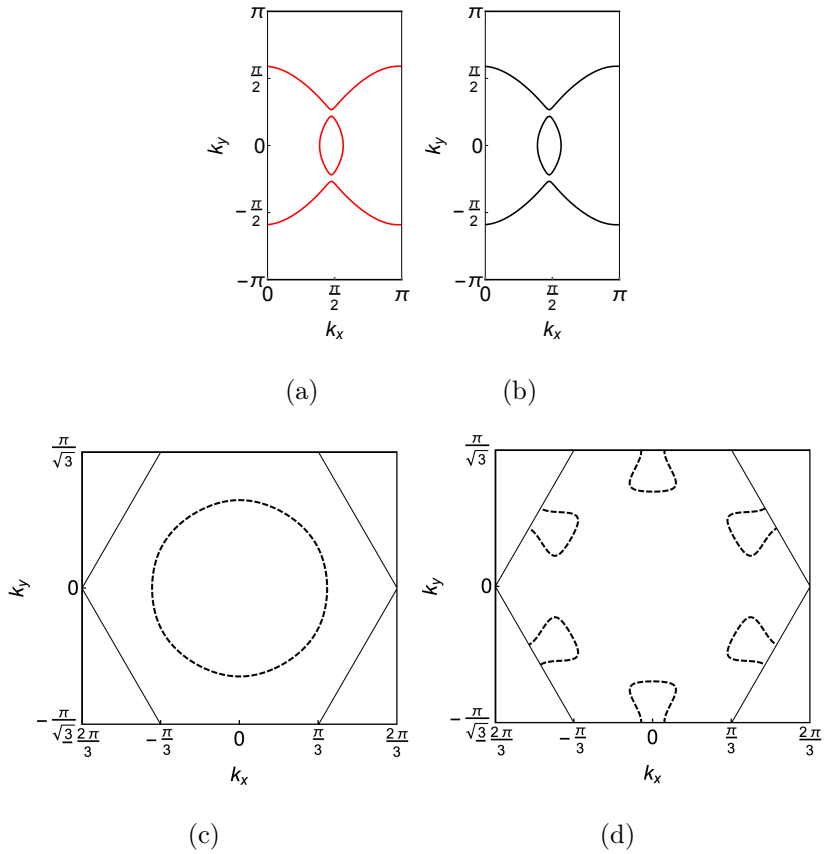

Figure A4 : The Fermi surfaces of the square lattice model in the P_S phase (4(a)) and in the P_L (4(b)) phase, and of the Kagomé lattice model in the P_S phase (4(c)) and in the P_L phase (4(d)).

A5 Analysis of the wavefunction reconstruction across the QCP

To further our understanding about the nonanalyticities across the QCP, we rewrite the Hamiltonian across the QCP in terms of the d-band and f-band eigenstates, which we denote as $|\phi^d_{\boldsymbol{k}}\rangle$ and $|\phi^f_{\boldsymbol{k}}\rangle$ respectively:

$$H = \sum_{\boldsymbol{k}} \begin{pmatrix} (\epsilon^d_{\boldsymbol{k}} - \mu + \lambda')|\phi^d_{\boldsymbol{k}}\rangle\langle\phi^d_{\boldsymbol{k}}| & \delta|\phi^d_{\boldsymbol{k}}\rangle\langle\phi^f_{\boldsymbol{k}}| \\ \delta|\phi^f_{\boldsymbol{k}}\rangle\langle\phi^d_{\boldsymbol{k}}| & (\epsilon^f_{\boldsymbol{k}} - \mu - \lambda')|\phi^f_{\boldsymbol{k}}\rangle\langle\phi^f_{\boldsymbol{k}}| \end{pmatrix}. \tag{A-36}$$

Here, δ is the hybridization strength. In addition, λ' is the Lagrangian multiplier, which is shifted from λ by a constant that can be absorbed into μ, to obtain the above symmetric form for later convenience. The hybridization, thus the wavefunction reconstruction, is the strongest at the $\boldsymbol{k}$ points where the conduction bands and spinon bands intersect, i.e. $\epsilon^f_{\boldsymbol{k}_0} - \mu = \epsilon^d_{\boldsymbol{k}_0} - \mu = 0$.

For the Kagomé case, Consider the case that the Fermi surface jumps. We expect λ' to track δ as the QCP is approached. Nonetheless, we can still start out with the points where $\epsilon^f_{\boldsymbol{k}_0} - \mu = \epsilon^d_{\boldsymbol{k}_0} - \mu = 0$. In this case, we can write the λ' term as $\lambda'\sigma_0 \otimes \tau_z$, where τ_z is the Pauli matrix for the orbital space. This term does not commute with the hybridization term, which is off-diagonal in the τ space. (Note that both the diagonal and off-diagonal blocks above are diagonal matrices in the sublattice space, and therefore commute with each other in that space.) Therefore, the presence of any λ' prevents us from block-diagonalizing the Hamiltonian even for infinitesimal δ. The new eigenstates are therefore reconstructed completely.

A6 Phase diagram in the saddle-point analysis

To illustrate our procedure, we consider the phase diagram arising from the saddle-point analysis in the case of $J_1 - J_2$ square lattice. We minimize the total energy of Eq. (**??**) with respect to the amplitudes of the link fields ρ_{ij} and $\rho_{K,i}$. The phase

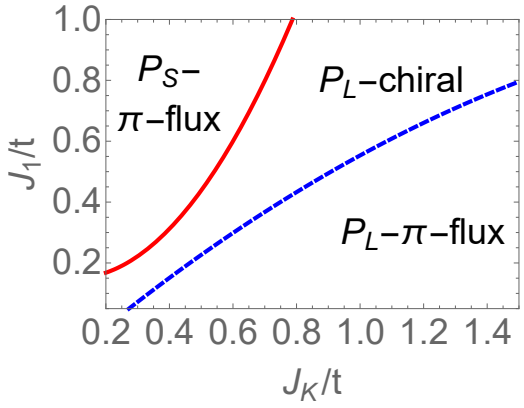

Figure A5 : (Color online) The phase diagram of $J_1 - J_2 - J_K$ model with $J_2 = J_1/2$ and $n_d = 0.5$ (A5).

diagram of the square lattice model is shown in Fig. (A5), where the red (solid) and blue (dashed) lines respectively mark a first-order phase transition and a crossover. It shows that both the flux-state and the chiral-state solutions can be stabilized, i.e. having lower energies than the unhybridized phase, for J_K larger than some critical $J_{K,c}$. The flux phase solution has the lowest energy when stabilized, signaling that the Kondo coupling favors the gapless states.

For the pyrochlore lattice, the CSL state is gapless [123], and our result here strongly suggests that a similar chiral state could be the ground state on the pyrochlore lattice when the Kondo coupling is introduced.

Appendix B: Weyl-Kondo semimetal in heavy fermion systems

B1 Analysis of the bulk spectrum

In the strong coupling regime that is relevant to heavy fermion systems, we can approach the prohibition of d_σ fermion double occupancy by an auxiliary boson method [152]. Representing $d^\dagger_{i\sigma} = f^\dagger_{i\sigma} b_i$, the $f^\dagger_{i\sigma}$ (b_i) are fermonic (bosonic) operators satisfying the constraint $b^\dagger_i b_i + \sum_\sigma f^\dagger_{i\sigma} f_{i\sigma} = 1$. At the saddle point level, we replace $b^\dagger_i,\ b_i \to r$, and introduce a Lagrange multiplier ℓ to enforce the local constraint. Defining $\Xi^T_{\mathbf{k}} \equiv \begin{pmatrix} d_{\mathbf{k}\uparrow,A} & d_{\mathbf{k}\uparrow,B} & d_{\mathbf{k}\downarrow,A} & d_{\mathbf{k}\downarrow,B} \end{pmatrix}$ and $\Psi^T_{\mathbf{k}} \equiv \begin{pmatrix} c_{\mathbf{k}\uparrow,A} & c_{\mathbf{k}\uparrow,B} & c_{\mathbf{k}\downarrow,A} & c_{\mathbf{k}\downarrow,B} \end{pmatrix}$, we can transform Hamiltonian H_c, H_{cd}, and H_d into the pseudospin basis using $\breve{\Xi}_{\mathbf{k}} = S^\dagger_\sigma \Xi_{\mathbf{k}}$ and $\breve{\Psi}_{\mathbf{k}} = S^\dagger_\sigma \Psi_{\mathbf{k}}$, with $S^\dagger_\sigma = U_\sigma \tau_0$ being a unitary matrix which consists of the $|\pm D\rangle$ eigenvectors. The effective hybridization becomes rV is nonzero only for $V > V_c$, whenever the conduction-electron density of states has a pseudogap form near the Fermi energy [61]. The hybridization part can be re-expressed as

$$H_{cd} = \sum_{\mathbf{k}} \left[\breve{\Psi}^\dagger_{\mathbf{k}} \cdot rV \mathbb{1}_4 \cdot \breve{\Xi}_{\mathbf{k}} + \text{H.c.} \right]. \tag{B-1}$$

Introducing $\breve{\Psi}^T_{\mathbf{k}} = \begin{pmatrix} \breve{\psi}^T_{\mathbf{k}+} & \breve{\psi}^T_{\mathbf{k}-} \end{pmatrix}$, $\breve{\Xi}^T_{\mathbf{k}} = \begin{pmatrix} \breve{\xi}^T_{\mathbf{k}+} & \breve{\xi}^T_{\mathbf{k}-} \end{pmatrix}$, where $\breve{\psi}^T_{\mathbf{k}\pm} = \begin{pmatrix} \breve{\psi}_{\mathbf{k}\pm,A} & \breve{\psi}_{\mathbf{k}\pm,B} \end{pmatrix}$ and $\breve{\xi}^T_{\mathbf{k}\pm} = \begin{pmatrix} \breve{\xi}_{\mathbf{k}\pm,A} & \breve{\xi}_{\mathbf{k}\pm,B} \end{pmatrix}$, we find that the strong-coupling Hamiltonian can straightforwardly be written in the $|\pm D\rangle$ basis as $H^s = \sum_{a=\pm} \mathcal{H}^s_a$,

$$\mathcal{H}^s_a = \sum_{\mathbf{k},a=\pm} \begin{pmatrix} \breve{\psi}^\dagger_{\mathbf{k}a} & \breve{\xi}^\dagger_{\mathbf{k}a} \end{pmatrix} \begin{pmatrix} h_{\mathbf{k}a} - \mu \mathbb{1}_2 & V_s \mathbb{1}_2 \\ V_s \mathbb{1}_2 & E_s \mathbb{1}_2 \end{pmatrix} \begin{pmatrix} \breve{\psi}_{\mathbf{k}a} \\ \breve{\xi}_{\mathbf{k}a} \end{pmatrix}, \tag{B-2}$$

where $V_s \equiv rV$ and $E_s \equiv E_d + \ell$. Straightforward diagonalization of the strong-coupling Hamiltonian yields a set of four quasiparticle bands for each spin sector

as

$$\mathcal{E}^{(\tau,\alpha)}_{\pm D}(\mathbf{k}) = \frac{1}{2}\left[E_s + \tilde{\varepsilon}^{\tau}_{\pm D} + \alpha\sqrt{\left(E_s - \tilde{\varepsilon}^{\tau}_{\pm D}\right)^2 + 4V_s^2}\right], \tag{B-3}$$

$$\tilde{\varepsilon}^{\tau}_{\pm D} = \varepsilon^{\tau}_{\pm D} - \mu, \tag{B-4}$$

$$\varepsilon^{\tau}_{\pm D} = \tau\sqrt{u_1(\mathbf{k})^2 + u_2(\mathbf{k})^2 + (m \pm \lambda D(\mathbf{k}))^2}, \tag{B-5}$$

where $\tau = (+,-)$, and $\alpha = (+,-)$ indexes the upper/lower quartet of bands, respectively.

To gain a deeper understanding of the gap structure of the hybridized bands, it is more convenient to first diagonalize the conduction electron part of the Hamiltonian, which is possible since the off-diagonal blocks and the bottom right block are all proportional to 2×2 identity matrices. Diagonalizing the conduction electron part of the Hamiltonian, we can rewrite the strong coupling Hamiltonian in a diagonal form,

$$h^D_{\mathbf{k}\pm} = \begin{pmatrix} \varepsilon^{+}_{\pm D} & 0 \\ 0 & \varepsilon^{-}_{\pm D} \end{pmatrix}, \tag{B-6}$$

and in the new basis, the Hamiltonian becomes

$$\mathcal{H}^s_{\pm} = \sum_{\mathbf{k}} \begin{pmatrix} (\psi^D_{\mathbf{k}\pm})^\dagger & (\xi^D_{\mathbf{k}\pm})^\dagger \end{pmatrix} \begin{pmatrix} h^D_{\mathbf{k}a} - \mu\mathbb{1}_2 & V_s\mathbb{1}_2 \\ V_s\mathbb{1}_2 & E_s\mathbb{1}_2 \end{pmatrix} \begin{pmatrix} \psi^D_{\mathbf{k}\pm} \\ \xi^D_{\mathbf{k}\pm} \end{pmatrix}. \tag{B-7}$$

We can then directly see that the matrix elements associated with the 1st and 3rd fields are decoupled from the 2nd and 4th fields, which means we can simplify the 4×4 matrix in either $|\pm D\rangle$ sector, to be two 2×2 matrices, which allows us to examine the eigenenergy bands analytically. Below, we discuss the cases in different $|\pm D\rangle$ sectors separately. Our main conclusion below is that the Weyl-Kondo semimetal phase can only occur at the $|-D\rangle$ sector in the hybridized band regime, and the hybridized bands in $|+D\rangle$ sector *always* remain gapped.

B1.1 $|+D\rangle$ sector:

For further analysis in the band gaps, we assume that E_s lies well below the conduction electron bands $\varepsilon^{\tau}_{\pm D}$. In addition, for the condition for 1/4-filling, E_s is required to be positive $E_s > 0$. Focusing on the two 2×2 matrices of the $|+D\rangle$ sector, we can separate the Hamiltonian into $\mathcal{H}^s_+ = \sum_{\alpha,\tau} H^{s,\tau}_{+,\alpha}$, the energies obtained are

$$\mathcal{E}^{(+,\alpha)}_{+D} = \frac{1}{2}\left[E_s + \tilde{\varepsilon}^{+}_{+D} + \alpha\sqrt{\left(E_s - \tilde{\varepsilon}^{+}_{+D}\right)^2 + 4V_s^2}\right], \tag{B-8}$$

$$\mathcal{E}^{(-,\alpha)}_{+D} = \frac{1}{2}\left[E_s + \tilde{\varepsilon}^{-}_{+D} + \alpha\sqrt{\left(E_s - \tilde{\varepsilon}^{-}_{+D}\right)^2 + 4V_s^2}\right]. \tag{B-9}$$

Since $\varepsilon^{+}_{+D} > \varepsilon^{-}_{+D}$, we can see $\mathcal{E}^{(+,+)}_{+D} > \mathcal{E}^{(-,-)}_{+D}$ and these two bands always remain gapped. Similarly, within each pair of branches $\mathcal{E}^{(\tau,+)}_{+D} > \mathcal{E}^{(\tau,-)}_{+D}$, and they should be always gapped. The only possibility that the gap closes occurs between $\mathcal{E}^{(+,-)}_{+D}$ and $\mathcal{E}^{(-,+)}_{+D}$. If there is a crossing between them at some momenta $\mathbf{k} = \mathbf{k}_0$, the two bands should be degenerate $\mathcal{E}^{(+,-)}_{+D}(\mathbf{k}_0) = \mathcal{E}^{(-,+)}_{+D}(\mathbf{k}_0)$, which leads to

$$\begin{aligned}
\varepsilon^{+}_{+D}(\mathbf{k}_0) - \varepsilon^{-}_{+D}(\mathbf{k}_0) &= \sqrt{\left(E_s - \tilde{\varepsilon}^{+}_{+D}(\mathbf{k}_0)\right)^2 + 4V_s^2} + \sqrt{\left(E_s - \tilde{\varepsilon}^{-}_{+D}(\mathbf{k}_0)\right)^2 + 4V_s^2} \\
&\geq \varepsilon^{+}_{+D}(\mathbf{k}_0) + \varepsilon^{-}_{+D}(\mathbf{k}_0) - 2E_s \\
&\Rightarrow \varepsilon^{-}_{+D}(\mathbf{k}_0) \leq E_s,
\end{aligned} \tag{B-10}$$

where we use the assumption that $E_s < \epsilon^{\tau}_{\pm D}$ in the second line. This in turn leads to a contradiction to our initial condition that the d fermion Fermi energy is well below the four conduction electron bands, $E_s < \varepsilon^{\tau}_{\pm D}$. Therefore, we conclude that there cannot be any crossing between $\mathcal{E}^{(+,-)}_{+D}$ and $\mathcal{E}^{(-,+)}_{+D}$. The hybridized bands in the $|+D\rangle$ sector *always* remain gapped at any momenta and Weyl nodes cannot reside there. Now let's examine the $|-D\rangle$ sector.

B1.2 $|-D\rangle$ sector:

In the $|-D\rangle$ sector, we can also decompose the 4×4 Hamiltonian matrix to two 2×2 matrices, $\mathcal{H}^s_+ = \sum_{\alpha,\tau} H^{s,\tau}_{+,\alpha}$, which gives the eigenvalues as

$$\mathcal{E}^{(+,\alpha)}_{-D} = \frac{1}{2}\left[E_s + \tilde{\varepsilon}^+_{-D} + \alpha\sqrt{\left(E_s - \tilde{\varepsilon}^+_{-D}\right)^2 + 4V_s^2}\right], \tag{B-11}$$

$$\mathcal{E}^{(-,\alpha)}_{-D} = \frac{1}{2}\left[E_s + \tilde{\varepsilon}^-_{-D} + \alpha\sqrt{\left(E_s - \tilde{\varepsilon}^-_{-D}\right)^2 + 4V_s^2}\right]. \tag{B-12}$$

The bands' dispersions associated with the conduction electrons show Weyl nodes at certain momenta, i.e. $\mathbf{k} = \mathbf{k}_W$, where $\varepsilon^+_{-D}(\mathbf{k}_W) = \varepsilon^-_{-D}(\mathbf{k}_W) = 0$. There are actually 12 inequivalent $\mathbf{k}_W$ along the $X - W$ lines on the 3D BZ boundary, determined by the condition $\frac{m}{4|\lambda|} = \sin(\frac{k_0}{2})$, where $\mathbf{k}_W$ is a cyclic permutation of the elements in a vector $(k_0, 0, \pm2\pi)$. At $\mathbf{k} = \mathbf{k}_W$, in the hybridized bands we then have

$$\mathcal{E}^{(+,+)}_{-D}(\mathbf{k}_W) = \mathcal{E}^{(-,+)}_{-D}(\mathbf{k}_W), \tag{B-13}$$

$$\mathcal{E}^{(+,-)}_{-D}(\mathbf{k}_W) = \mathcal{E}^{(-,-)}_{-D}(\mathbf{k}_W). \tag{B-14}$$

We can see that in the hybridized bands, there are actually *two* pairs of degenerate bands sitting at the momenta $\mathbf{k}_W$. Near $\mathbf{k}_W$, the band dispersions can be linearized.

Due to the constraints in the strong-coupling regime, $\mathcal{H}^s_a$ must be solved self-consistently with the saddle-point equations,

$$\tfrac{1}{2N_u}\textstyle\sum_{\mathbf{k},a=\pm}\left\langle \breve{\xi}^\dagger_{\mathbf{k}a}\breve{\xi}_{\mathbf{k}a}\right\rangle + r^2 = 1, \qquad \tfrac{V}{4N_u}\textstyle\sum_{\mathbf{k},a=\pm}\left[\left\langle \breve{\psi}^\dagger_{\mathbf{k}a}\breve{\xi}_{\mathbf{k}a}\right\rangle + \text{H.c.}\right] + r\ell = 0, \tag{B-15}$$

where N_u is the number of the unit cell. Here we can tune the chemical potential to be $\mu = -V_s^2/E_s$, with $E_s > 0$. This fixes the lower Weyl node to the Fermi energy, at 1/4-filling, as shown in Fig. 3.2 in Chapter 3. For the illustration in Chapter 3, we use the same bare coupling parameters to be $(t, \lambda, E_d, V) = (1, 0.5, 1, -6, 6.6)$, and solved self-consistently for $r \simeq 0.259$ and $\ell \simeq 6.334$, with error $\epsilon \leq \mathcal{O}(10^{-5})$ on a $64\times64\times64$ unit cell diamond lattice.

B2 Berry curvature

The Berry curvature field $\vec{\Omega}(\mathbf{k})$ is akin to a ficticious magnetic field in momentum space; analogously, the Weyl nodes manifest as monopole sources and sinks of Berry curvature [210, 145]. The field is a way of representing the tensor components since it is a 3×3 antisymmetric tensor in three dimensions, $\vec{\Omega}(\mathbf{k}) = (\Omega_{yz}(\mathbf{k}), \Omega_{zx}(\mathbf{k}), \Omega_{xy}(\mathbf{k}))$. The components are given by the gauge invariant equation [210, 145],

$$\Omega_{ab}(\mathbf{k}) = \sum_{n \neq n'} \mathcal{I}m \frac{\langle n\mathbf{k}|\partial_{c,k_a} H^s_{\mathbf{k}}|n'\mathbf{k}\rangle\langle n'\mathbf{k}|\partial_{c,k_b} H^s_{\mathbf{k}}|n\mathbf{k}\rangle}{(\mathcal{E}_n - \mathcal{E}_{n'})^2}, \tag{B-16}$$

where $H^s_{\mathbf{k}}$ is the 8×8 Bloch matrix in the strong coupling regime in physical spin space, ∂_{c,k_a} is the derivative with respect to *only* the conduction electrons corresponding to the velocity of the charge carriers. $\mathcal{E}_n = \mathcal{E}^{(\tau,\alpha)}_\nu$ and $|n\mathbf{k}\rangle$ are the Bloch eigenenergies and eigenstates of $H^s_{\mathbf{k}}$, with index n specifying one of the eight bands, $n = (\tau, \alpha, \nu) = (\pm, \pm, \pm D)$.

In Chapter 3, the Berry curvature of the heavy Weyl fermions in the strong coupling regime were shown; specifically we plot the field's unit length 2D projection onto the k_x-k_y plane,

$$\hat{\Omega}(k_x, k_y, 2\pi) = \frac{1}{|\vec{\Omega}(k_x, k_y, 2\pi)|} \Big(\Omega_{yz}(k_x, k_y, 2\pi),\ \Omega_{zx}(k_x, k_y, 2\pi)\Big). \tag{B-17}$$

B3 Surface states

Following the approach in Ref. [87], we also seek surface states in the $|-D\rangle$ sector near the Weyl nodes. The nodes are on the square faces of the fcc Brillouin zone boundary, along the lines connecting high symmetry points X and W. We find that the Hamiltonian matrix of $\mathcal{H}^s_-$, Eq. (B-2) can be expressed

$$\begin{aligned} h_-(\mathbf{k}) \quad &= (\kappa^0 + \kappa^z) \otimes \tfrac{1}{2}\left[u_1(\mathbf{k})\tau_x + u_2(\mathbf{k})\tau_y + (m - \lambda D(\mathbf{k}))\tau_z)\right] \\ &+ \left[(E_s - \mu)\kappa^0 - (E_s + \mu)\kappa^z + V_s\kappa^x\right] \otimes \tau_0 \end{aligned} \tag{B-18}$$

where κ^i are Pauli matrices acting on the $\left(\breve{\psi}_{\mathbf{k}-}, \breve{\xi}_{\mathbf{k}-}\right)$ basis. We linearize the Hamiltonian matrix near $\mathbf{q} = \left(k_x, k_y, 2\pi\right)$ in $\tilde{q}_z = k_z - 2\pi$ around $\tilde{q}_z = 0$. Defining

$u'_{1/2} \equiv \partial_{k_z} u_{1/2}(\mathbf{k})|_{k_z=2\pi}$, $u' \equiv \sqrt{(u'_1)^2 + (u'_2)^2}$, and $u \equiv \sqrt{u_1^2 + u_2^2}$, we obtain

$$\begin{aligned} h_-(\mathbf{q}) \quad &= (\kappa^0 + \kappa^z) \otimes \tfrac{1}{2}[\tilde{q}_z u'(\mathbf{q})\tau_x - u(\mathbf{q}) sgn(k_x k_y)\tau_y + (m - \lambda D(\mathbf{q}))\tau_z] \\ &+ \left[(E_s - \mu)\kappa^0 - (E_s + \mu)\kappa^z + V_s \kappa^x\right] \otimes \tau_0. \end{aligned} \tag{B-19}$$

Making the real-space replacement $\tilde{q}_z \to -i\partial_z$, we can enforce the boundary condition by assigning the value of the staggered mass to be $m = m_+ > 4|\lambda|$ outside for $z > 0$ (trivially insulating vacuum), and $m = m_- < 4|\lambda|$ for $z < 0$, such that the bulk is in a stable Weyl semimetal phase.

Generalizing the wavefunction suggested in Ref. [87], we find the surface eigenstates in the plane of the four Weyl nodes around the X point to be

$$\psi_s(k_x, k_y, z) \quad = A_s e^{\mp \frac{z}{\xi_\pm}} |\kappa\rangle \otimes |\tau_y = +1\rangle \otimes |-D\rangle, \tag{B-20}$$

with

$$|\kappa\rangle \quad = B_s \begin{pmatrix} 1 \\ -\sqrt{1 - \left(\frac{\beta^s_{\mathbf{k}}}{V_s}\right)^2} - \frac{\beta^s_{\mathbf{k}}}{V_s} \end{pmatrix}, \tag{B-21}$$

$$\beta^s_{\mathbf{k}} \quad \equiv -\frac{1}{2}\left[u(\mathbf{q}) sgn(k_x k_y) + E_s + \mu\right], \tag{B-22}$$

where A_s, B_s are normalization constants. We identify $\xi_\pm = \pm u'(\mathbf{q})/(m_\pm - \lambda D(\mathbf{q}))$ as the penetration depth of the surface wavefunctions. Inside the boundary, the divergence of ξ_- when $D(\mathbf{q}) = m_-$ indicates that the surface states merge with the bulk states, becoming indistinguishable [87].

B4 Conduction electrons: Inversion-symmetry breaking and time-reversal-symmetry breaking

Here we consider H_c in the presence of a static magnetic field, as an illustration of the effect of a time-reversal symmetry breaking on the Weyl state. Consider the

conduction electron Hamiltonian,

$$H_c = \sum_{\langle ij\rangle,\sigma}\left(t_{ij}c^\dagger_{i\sigma}c_{j\sigma}+\text{H.c.}\right)+i\lambda\sum_{\langle\langle ij\rangle\rangle}\left[c^\dagger_{i\sigma}\left(\boldsymbol{\sigma}\cdot\mathbf{e}_{ij}\right)c_{j\sigma}-\text{H.c.}\right] \tag{B-23}$$

$$+m\sum_{i,\sigma}(-1)^i c^\dagger_{i\sigma}c_{i\sigma}+\sum_j \boldsymbol{M}\cdot\left(c^\dagger_{j\sigma}\boldsymbol{\sigma}c_{j\sigma}\right) \tag{B-24}$$

where $\mathbf{e}_{ij}=\frac{\mathbf{e}_i\times\mathbf{e}_j}{|\mathbf{e}_i\times\mathbf{e}_j|}$ are determined by the two bond vectors connecting second-nearest-neighbors, and $\boldsymbol{\sigma}=(\sigma_x,\sigma_y,\sigma_z)$ are the Pauli matrices acting on spin space, and the last term is the time reversal symmetry breaking (TRB) term, with $\boldsymbol{M}$ being the local moment and $c^\dagger_{j\sigma}\boldsymbol{\sigma}c_{j\sigma}$ being the conduction electron spin.

The non-centrosymmetric diamond lattice (the "zincblende" lattice) is presented in Fig. 1(a). Although the diamond and zincblende lattices are structurally the same, the different on-site potential m reduces the O_h cubic point group symmetry of the diamond lattice to tetragonal T_d symmetry in the zincblende. The simplest way to visualize the inversion symmetry-breaking introduced by the m term is to compare the interlocked sublattice unit cells under the inversion operationas in Fig. 1(b). If one reflects the position of any site across the indicated dotted inversion "plane" (the (1,1,1)-direction being normal to it), the upper four sites neatly exchange positions with the lower four. Conversely, if the on-site potential differentiates the sublattices via m, an inversion operation exchanges the distinct sublattice sites, as seen in Fig. 1(c), so inversion symmetry is broken.

Here we show an example of a Weyl semimetal phase in the broken time reversal symmetry ($\boldsymbol{M}\neq 0$), in the case of the diamond lattice ($m=0$). For simplicity, below we choose $\boldsymbol{M}=M_z\hat{z}$ and the second term becomes a Zeeman-like term. Following the same procedure as before, we introduce the basis in momentum space $\Psi^T_{\mathbf{k}}=\begin{pmatrix}c_{\mathbf{k}\uparrow,A} & c_{\mathbf{k}\uparrow,B} & c_{\mathbf{k}\downarrow,A} & c_{\mathbf{k}\downarrow,B}\end{pmatrix}$. The Hamiltonian of the conduction electron becomes $H^{TRB}_{c,M}=\Psi^\dagger_{\mathbf{k}}\cdot h^{TRB}_c\cdot\Psi_{\mathbf{k}}$, with

$$h^{TRB}_c=\sigma_0\left[u_1(\mathbf{k})\tau_x+u_2(\mathbf{k})\tau_y\right]+M_z\sigma_z\tau_0+\lambda\left[\mathbf{D}(\mathbf{k})\cdot\boldsymbol{\sigma}\right]\tau_z, \tag{B-25}$$

where $u_{1/2}$ and vector $\mathbf{D}$ are defined in Chapter 3. A 3D Dirac semimetal is realized

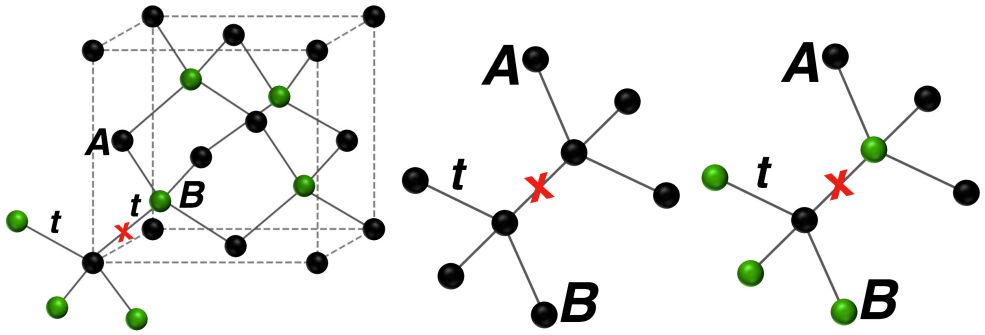

(a) (b) (c)

Figure B1 : (a) Zincblende lattice: diamond lattice with $\pm m$ differentiating A, B sublattice; (b) diamond lattice unit cell, and (c) zincblende unit cell. Translating an A atom across the inversion point marked "X" exchanges it with the B site, breaking inversion symmetry in (a) and (c), but preserving it in (b) since the two sites are equivalent.

with Dirac points located at X points in the absence of the TRB term, as ilustrated in Fig. 2(a).

Upon increasing the TRB term, first we observe that Weyl nodes appear along $X-\Gamma$ lines and along $X-W$ lines on the 3D BZ boundary parallel to $\hat{k}_z$-axis, and increasing to $M_z = 3$ moves both Weyl nodes toward the Γ point, illustrated in Fig. S2(b).

Next, we analyze the critical value of M_z signaling the phase transition that separates the aforementioned TRB-Weyl semimetals from the topologically trivial insulator phase. Focusing on one of the $X-\Gamma$ lines that we suspect to harbor Weyl nodes, we assume its position is at $\mathbf{k}_W = \mathbf{k}_X - \delta\mathbf{k}$, where $\mathbf{k}_X$ is the X-point momentum, and $\delta\mathbf{k} = (\delta k_x, 0, 0)$ with $|\delta k_x| > 0$. We can then straightforwardly find that all the components of $\mathbf{D}(\mathbf{k})$ along that line vanish. The Hamiltonian matrix along the line can be simplified to be

$$h_c^{TRB}|_{X\Gamma} = 2t\sigma_0 \left[\left(1 - \cos\left(\frac{\delta k_x}{2}\right) \right) \tau_x + \sin\left(\frac{\delta k_x}{2}\right) \tau_y \right] + M_z \sigma_z \tau_0,$$

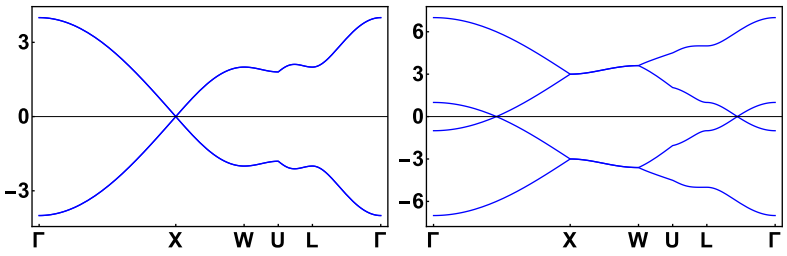

(a) (b)

Figure B2 : Band structure along the high symmetry points of the fcc Brillouin zone in the presence of time-reversal symmetry breaking (preserving inversion symmetry), originated from a local moment field M_z coupled to the conduction electron spin, using $\lambda = \frac{1}{2}$. (a) $M_z = 0$: Dirac semimetal; (b) $M_z = 3$: Weyl nodes along different lines are all moved toward Γ point.

which leads to the eigenvalues

$$E_c^{TRB,\sigma} = \sigma M_z \pm 2\sqrt{2\left[1 - \cos\left(\frac{\delta k_x}{2}\right)\right]}, \tag{B-26}$$

where $\sigma = \pm$ for spin=$\uparrow,\downarrow$. For $M_z > 0$, we can see that gaplessness can only occur when $M_z = 2\sqrt{2\left[1 - \cos\frac{\delta k_x}{2}\right]}$, which leads to the condition

$$\cos\left(\frac{\delta k_x}{2}\right) = 1 - \frac{M_z^2}{8}. \tag{B-27}$$

Therefore, we can see that the condition can be satisfied for $0 < M_z \leq M_z^c = 4$, after which the absolute value of the right hand side becomes greater than 1 and the condition can no longer be held. The critical value of $M_z^c = 4$ is fully consistent with the numerical analysis illustrated in Fig. B2.

B5 Specific heat from a Weyl node

The specific heat is calculated as

$$c_v \quad = \left(\frac{\partial u}{\partial T}\right)_V = \frac{\partial}{\partial T}\int_{BZ} \frac{d^3\mathbf{k}}{(2\pi)^3}\varepsilon_{\mathbf{k}} f(\varepsilon_{\mathbf{k}}), \tag{B-28}$$

where $\varepsilon_{\mathbf{k}}$ is the energy dispersion, u is the energy density, and the integral is over the first Brillouin zone. Here the occupation distribution function $f(\varepsilon_{\mathbf{k}})$ is the Fermi function. We focus on the linear dispersion regime where we can approximate $\varepsilon_{\mathbf{k}} = \hbar v^* k$. We will take the renormalized Fermi velocity v^* for its asymptotic low-temperature value. Analyzing the temperature dependence of the condensate amplitude in our saddle-point analysis will only cause subleading corrections to the temperature dependence of the specific heat.

The result for the specific heat per unit volume is

$$c_v = \frac{7\pi^2}{30} k_B \left(\frac{k_B T}{\hbar v^*}\right)^3. \tag{B-29}$$

This shows that the T^3 contribution to the specific heat becomes large when v^* is small, as in the case of heavy fermion systems.

B6 Fermi liquid theory approach for the specific heat of a Weyl fermion

Adopting the formula at section 19 in chapter 4 in Ref. [211], we can express the specific heat per volume from a Weyl fermion as

$$c_v = \int \frac{d^3\mathbf{k}}{(2\pi)^2} \frac{1}{2\pi i T} \int_{-\infty}^{\infty} \varepsilon \left[-\frac{\partial f(\varepsilon)}{\partial \varepsilon}\right] \left[\ln G_R(\mathbf{k},\varepsilon) - \ln G_A(\mathbf{k},\varepsilon)\right] d\varepsilon, \tag{B-30}$$

where T is the temperature, k_B is the Boltzmann constant, $f(\varepsilon)$ is the Fermi distribution function, $G_R(\mathbf{k},\varepsilon) = Z/(\varepsilon - \xi_{\mathbf{k}} + i0^+)$, is the retarded Green function of Fermi liquid quasi-particles, where Z is the quasi-particle weight, and $\xi_{\mathbf{k}} = \hbar v^* |\mathbf{k}| \equiv \hbar v^* k$ for $\xi_{\mathbf{k}} > 0$ ($\xi_{\mathbf{k}} = -\hbar v^* k$ for $\xi_{\mathbf{k}} < 0$), *i.e.*, a Weyl fermion dispersion, the advanced Green function is $G_A = G_R^*$, and we set the chemical potential $\mu = 0$ sitting exactly at the nodal point. Adopting the Sommerfeld expansion as

$$\int_{-\infty}^{\infty} d\varepsilon u(\varepsilon) \left[\frac{\partial f(\varepsilon)}{\partial \varepsilon}\right] \simeq -u(0) - \frac{\pi^2}{6}(k_B T)^2 \left(\frac{\partial^2 f(\varepsilon)}{\partial \varepsilon^2}\right)_{\varepsilon=0} - \frac{7\pi^4}{360}(k_B T)^4 \left(\frac{\partial^4 f(\varepsilon)}{\partial \varepsilon^4}\right)_{\varepsilon=0} + \cdots \tag{B-31}$$

Taking derivatives and setting $\varepsilon = 0$, we obtain

$$c_v = \int \frac{d^3\mathbf{k}}{(2\pi)^3} k_B \left[\frac{\pi}{3} k_B T \; Im\left(G_R^{-1} \partial_\varepsilon G_R\right)_{\varepsilon=0} + \frac{7\pi^4}{90}(k_B T)^3 Im\left(G_R^{-1}\partial_\varepsilon^3 G_R + 2G_R^{-3}\left(\partial_\varepsilon G_R\right)^3 - 3G_R^{-2}\partial_\varepsilon G\right.$$

where $Im\,(A)$ means the imaginary part of A. For a Weyl fermion, we find that $Im\left[G_R^{-1}\partial_\varepsilon G_R\right] = \pi\delta(\varepsilon - \xi_{\mathbf{k}})$, where $\delta(x)$ is the Dirac delta function and the identity

$$\frac{1}{x+i0^+} = \mathcal{P}_v\left(\frac{1}{x}\right) - i\pi\delta(x) \tag{B-33}$$

is explicitly used, where $\mathcal{P}_v$ means principle value. For the leading linear-T term, the integral involves

$$\int \frac{4\pi k^2 dk}{(2\pi)^3}\delta(\xi_{\mathbf{k}}) = 0, \tag{B-34}$$

and therefore the leading linear-T term vanishes. For the second term above, we find that

$$G_R^{-1}\partial_\varepsilon^3 G_R + 2G_R^{-3}\left(\partial_\varepsilon G_R\right)^3 - 3G_R^{-2}\partial_\varepsilon G_R\partial_\varepsilon^2 G_R = -2\left[\mathcal{P}_v\left(\frac{1}{\varepsilon-\xi_{\mathbf{k}}}\right) - i\pi\delta(\varepsilon-\xi_{\mathbf{k}})\right]^3$$
$$= -2\left[\mathcal{P}_v\left(\frac{1}{\varepsilon-\xi_{\mathbf{k}}}\right)^3 + 3\mathcal{P}_v\left(\frac{1}{\varepsilon-\xi_{\mathbf{k}}}\right)^2(-i\pi)\delta(\varepsilon-\xi_{\mathbf{k}}) + 3\mathcal{P}_v\left(\frac{1}{\varepsilon-\xi_{\mathbf{k}}}\right)(-i\pi)^2\delta^2(\varepsilon-\xi_{\mathbf{k}}) + (-i\pi\right.$$

Focusing on the imaginary terms, we find that only the second term in (B-35) contributes to the results. The last term vanishes because the integral of cubic delta function is zero. Therefore, we find that

$$Im\left(G_R^{-1}\partial_\varepsilon^3 G_R + 2G_R^{-3}\left(\partial_\varepsilon G_R\right)^3 - 3G_R^{-2}\partial_\varepsilon G_R\partial_\epsilon^2 G_R\right)_{\varepsilon=0} = 6\pi\mathcal{P}_v\left(\frac{1}{\xi_{\mathbf{k}}}\right)^2\delta(\xi_{\mathbf{k}}). \tag{B-36}$$

Combining everything, we can obtain the specific heat per volume as

$$c_v \simeq \frac{7\pi^4}{15}k_B(k_BT)^3\int\frac{d^3\mathbf{k}}{(2\pi)^3}\mathcal{P}_v\left(\frac{1}{\xi_{\mathbf{k}}}\right)^2\delta(\xi_{\mathbf{k}}) \tag{B-37}$$
$$= \frac{7\pi^4}{90}k_B(k_BT)^3\frac{1}{2}\int_{-\infty}^{\infty}\frac{4\pi k^2 dk}{(2\pi)^3}\frac{2}{(\hbar v^* k)^2}\delta(\hbar v^* k) \tag{B-38}$$
$$= \frac{7\pi^2}{30}k_B\left(\frac{k_BT}{\hbar v^*}\right)^3. \tag{B-39}$$

Note that the principle value evaluation is not necessary since the k^2 in the denominator cancel the k^2 from the numerator. The factor $1/2$ in front of the integral in (B-38) is due to the extension of integral range from $-\infty$ to $+\infty$ together with even function. The factor of 2 in the numerator of $2/(\hbar v^* k)^2$ inside the integral in (B-38) is

originated from the fact that for each momentum k, there are two contribution from $\xi_{\mathbf{k}} = \pm\hbar v^* k$ in the present Weyl fermion band distribution. We can see that the Landau Femi liquid approach also demonstrate that the leading renormalization effects of the specific heat come as the $(1/v^*)^3$.

Appendix C: Weyl-Kondo semimetal in nonsymmorphic systems

C1 Existence of the Weyl-Kondo semimetal nodes

Here we show that in our model, the eigenenergies have Weyl nodes at the Fermi energy. First, the method for obtaining the eigenenergies was detailed in Ref. [117], and the eigenenergies are

$$\mathcal{E}^{(\tau,\alpha)}_{\pm D}(\boldsymbol{k}) = \frac{1}{2}\left[E_s + \tilde{\varepsilon}^{\tau}_{\pm D} + \alpha\sqrt{\left(E_s - \tilde{\varepsilon}^{\tau}_{\pm D}\right)^2 + 4V_s^2}\right], \tag{C-1}$$

$$\tilde{\varepsilon}^{\tau}_{\pm D} = \varepsilon^{\tau}_{\pm D} - \mu, \tag{C-2}$$

$$\varepsilon^{\tau}_{\pm D} = \tau\sqrt{u_1^2(\boldsymbol{k}) + u_2^2(\boldsymbol{k}) + (m \pm \lambda D(\boldsymbol{k}))^2}, \tag{C-3}$$

$$u_1(\boldsymbol{k}) = t\left(1 + \sum_{n=1}^{3}\cos(\boldsymbol{k}\cdot\mathbf{a}_n)\right), \tag{C-4}$$

$$u_2(\boldsymbol{k}) = t\sum_{n=1}^{3}\sin(\boldsymbol{k}\cdot\mathbf{a}_n), \tag{C-5}$$

$$\begin{aligned} D(\boldsymbol{k}) = 2\Big\{&\sin^2\left(\tfrac{k_x}{2}\right)\left[\cos\left(\tfrac{k_y}{2}\right) - \cos\left(\tfrac{k_z}{2}\right)\right]^2 \\ &+ \sin^2\left(\tfrac{k_y}{2}\right)\left[\cos\left(\tfrac{k_x}{2}\right) - \cos\left(\tfrac{k_z}{2}\right)\right]^2 \\ &+ \sin^2\left(\tfrac{k_z}{2}\right)\left[\cos\left(\tfrac{k_x}{2}\right) - \cos\left(\tfrac{k_y}{2}\right)\right]^2\Big\}^{1/2}, \end{aligned} \tag{C-6}$$

where the index which labels $\tau = \pm 1$, $\alpha = \pm 1$, $\pm D = \pm D(\boldsymbol{k})$ distinguishes the eight bands of the system, and the $\mathbf{a}_n$ are the primitive lattice vectors of the diamond lattice. The Hamiltonian is only separable in terms of the $|\pm D\rangle$ pseudospin basis, and α distinguishes between the upper and lower quartet of bands; within each quartet,

τ distinguishes the upper two from the lower two bands, and one can write

$$\begin{aligned}\tilde{\varepsilon}^{\tau}_{\pm D} &= \tau\varepsilon_{\pm D} - \mu, \\ \varepsilon_{\pm D} &= \sqrt{u_1^2(\boldsymbol{k}) + u_2^2(\boldsymbol{k}) + (m \pm \lambda D(\boldsymbol{k}))^2}.\end{aligned} \tag{C-7}$$

Without loss of generality, we take the parameters $t, r, V \geq 0$. There are line or Dirac nodal touchings in the case of $m = 0$, depending on whether $\lambda = 0$ or nonzero. Here, we are only interested in Weyl node touchings, and thus we consider only the case with both λ, m being nonzero; for definiteness, we focus on $\lambda, m > 0$.

The periodic Anderson model also has a few additional specifications. In the Kondo regime, we have

$$\begin{aligned}E_s &= E_d + \ell, \\ V_s &= rV,\end{aligned} \tag{C-8}$$

and $V > V_c$ for some critical value, beyond which the r-bosonic field is small but nonzero. It is taken that the bare localized fermions representing the $4f$ electrons should have an energy level E_d that has a bare value well below the conduction-electron bands, $E_d \ll \varepsilon^{\tau}_{\pm D}$. We chose to define $E_F = 0$ and $E_d < 0$; we will determine the signs of μ, ℓ near the end, and in Appendix C2.

With these pieces in place, it is simple to observe the following. Since all parameters and eigenenergies are real, and each term in the summation within each square root is squared (nonnegative), the square root quantities are also nonnegative [Eqs. (C-1),(C-6),(C-7), and Eq. (3.12)]. In turn, Eq. (C-7) implies that

$$\varepsilon_{+D} \geq \varepsilon_{-D} \geq 0, \tag{C-9}$$

given that $m, \lambda, D(\boldsymbol{k}) > 0$, since the differentiating term involving $D(\boldsymbol{k})$ yields

$$|m + \lambda D(\boldsymbol{k}))| \geq m \geq |m - \lambda D(\boldsymbol{k})| \geq 0. \tag{C-10}$$

It then follows from Eq. (C-7) that

$$-\varepsilon_{+D} \leq -\varepsilon_{-D} \leq 0 \leq +\varepsilon_{-D} \leq +\varepsilon_{+D}. \tag{C-11}$$

In the diamond lattice space group, a nontrivial filling enforced semimetal [90] occurs at filling factor $\nu = 2n$, $n \neq 2$. For a quarter of the bands to be full, $\nu = 2(n_c + n_d) = 2$ of the eight bands must be full, so the gapless band touching point should occur between the third (hole) $\mathcal{E}_3(\boldsymbol{k})$ band, and the second (filled) $\mathcal{E}_2(\boldsymbol{k})$ band. We label the bands according to ascending order in energy. Then, the condition that determines when Weyl nodes $\boldsymbol{k}_W$ are present at quarter filling is

$$\lim_{\boldsymbol{k}\to\boldsymbol{k}_W} \Delta_{32}(\boldsymbol{k}) = \lim_{\boldsymbol{k}\to\boldsymbol{k}_W} [\mathcal{E}_3(\boldsymbol{k}) - \mathcal{E}_2(\boldsymbol{k})] = 0. \tag{C-12}$$

It is clear from the form of Eqs. (C-1) and (C-7) that only the $\varepsilon_{\pm D}$ terms are $\boldsymbol{k}$-dependent, so they shall determine where nodes may appear in momentum space. Because of this model's underlying nonsymmorphic symmetry, we know that the nodes should appear on the BZB, and that they generically avoid three- and sixfold symmetry axes when TRS is preserved, [84] so we search on the [001] face of the BZ (the other faces are related by symmetry). We seek solutions to $\varepsilon_{\pm D} = 0$ [Eq. (C-7)]. Considering just the expression $\sqrt{u_1^2(\boldsymbol{k}) + u_2^2(\boldsymbol{k})} = 0$, this has line degeneracy solutions along the $X - W$ lines. Therefore, the solutions to $\varepsilon_{\pm D} = 0$ will be realized for nonzero m, λ when $\sqrt{(m \pm \lambda D(\boldsymbol{k}))^2} = 0$ also, since the $|m \pm D(\boldsymbol{k})|$ term determines the gap in the $\varepsilon_{\pm D}$ expressions. Along an $X - W$ line such as $\boldsymbol{k}_{XW} = (\boldsymbol{k}_x, 0, 2\pi)$, we already know from Eq. (C-10) that $|m + \lambda D(\boldsymbol{k})|$ is bounded below by m, which we insist is nonzero. Thus we can eliminate the $|+D\rangle$ sector from consideration for the solution, and ask whether the $|-D\rangle$ sector has a solution. Along $\boldsymbol{k}_{XW}$,

$$\varepsilon_{-D}(\boldsymbol{k}_{XW}) = \sqrt{(m - \lambda D(\boldsymbol{k}_{XW}))^2} \tag{C-13}$$

$$= \left| m - 4\lambda \left| \sin\left(\frac{k_x}{2}\right) \right| \right| = 0, \tag{C-14}$$

$$\leftrightarrow \left| \sin\left(\frac{k_x}{2}\right) \right| = \frac{m}{4\lambda}, \tag{C-15}$$

so the Weyl nodes occur at

$$\boldsymbol{k}_W = (k_0, 0, 2\pi), \tag{C-16}$$

$$k_0 = 2 \arcsin\left(\frac{m}{4\lambda}\right), \quad \mod \pi, \tag{C-17}$$

where the modulo π node is the opposite chirality partner in the neighboring BZ; within the first BZ, there are six inequivalent pairs total. Therefore we conclude that Weyl-Kondo nodes develop only for bands in the $|-D\rangle$ sector.

Now it is pertinent to apply these results to the full eigenenergy expression of Eq. (C-1). Since the sign of α picks out whether the band is in the upper four or lower four, we consider $\alpha = -1$ to analyze quarter filling. Having shown that a Weyl node is permitted for the $|-D\rangle$ sector, τ must be opposite in sign for each band.

Therefore, the Weyl nodes should exist between the bands $\mathcal{E}_{-D}^{(-,-)}$ and $\mathcal{E}_{-D}^{(+,-)}$. To gain some more insight, we solve $\mathcal{E}_{-D}^{(-,-)}(\boldsymbol{k}_W) = 0$, and express μ in terms of other parameters. From Eq. (C-1), we get

$$E_s - \mu - \sqrt{(E_s + \mu)^2 + 4V_s^2} = 0,$$

which implies

$$-E_s\mu = V_s^2.$$

Therefore,

$$\mu = -\frac{(rV)^2}{E_d + \ell}, \tag{C-18}$$

so we find that the sign of μ depends on the sign of $(E_d + \ell)$.

In our numerical calculations for the Kondo regime at quarter filling, the solutions always follow $(E_d + \ell) > 0$; for a given $E_d < 0$, we find $\ell > 0$ and $|E_d| < \ell$. For example, in our parameter choice for Figs. 4.3-4.4, we had $E_d = -7$, $\ell = 7.279$, and such results are consistent for other values of E_d, V: $(E_d + \ell) > 0$. Thus μ is negative. We reiterate that μ can be determined analytically if the filling is integer.

C2 Methods of solving the saddle point equations

Here we comment on the self-consistency procedure used to obtain the parameters $\mu,\ r,\ \ell$ in Ref. [117] and this work. Since the WKSM system was separable into

pseudospin sectors, the Bloch Hamiltonian matrix was decomposed from one 8×8 to two 4×4 matrices. A matrix size of 4×4 yields a characteristic equation with an eigenvalue polynomial degree of four, which is the upper limit to an exactly solvable eigenvalue problem. When the calculation is exactly at quarter filling, the chemical potential does not have to be numerically determined, as shown in Appendix C1. However, for the calculations with a finite Fermi surface (e.g., Fig. 4.6), we can determine the chemical potential μ numerically.

The remaining two saddle point equations are solved using the Newton-Raphson method. [212] This method can solve nonlinear systems of equations, given an initial guess that is close enough to the eventual solution. Whenever r, ℓ are changed, μ is updated. If the filling is specified precisely at the nodes (integer), μ is defined in Eq. (C-18). If the filling is noninteger, *i.e.* metallic, it may be solved for by using the bisection method on the density $n(\mu)$ of particles per site per spin.

Appendix D: Weyl semimetal's nodal evolution under a magnetic field

D1 Weyl Semimetal model without inversion or time reversal symmetries

D1.1 Introduction

The usual focus in the study of topological states of electronic matter has been on insulating states, a tradition that dates back to the heyday of quantum Hall systems and continued into the era of topological insulators. Topological metals have only been studied recently [213]. An outstanding question is how topological metals can arise as a result of strong correlations. Of particular interest in this context are heavy-fermion semimetals [17], in which the electron correlations are strong and spin-orbit coupling may be large. Recently, concurrent theoretical and experimental studies have advanced the notion of a Weyl-Kondo semimetal. In Ref. [117, 116], a theoretical analysis was carried out for a strongly correlated model in which the inversion symmetry (IS) is broken while the time-reversal symmetry (TRS) is preserved. Meanwhile, Refs. [137, 162, 170] have experimentally discovered this phase in the non-magnetic non-centrosymmetric heavy fermion system $Ce_3Bi_4Pd_3$.

In this paper, we briefly summarize these developments in Sec. D1.2, and describe what is expected theoretically when the TRS is also broken in Sec. D1.3. Our results suggest that, upon the tuning of parameters that break both the TRS and IS, Weyl semimetal (WSM) nodes are moved about and annihilated through critical phase boundaries with distinct quadratic-band touchings. In Sec. D1.5, we discuss these results and point to further studies for the future.

D1.2 Weyl-Kondo semimetal with time-reversal invariance

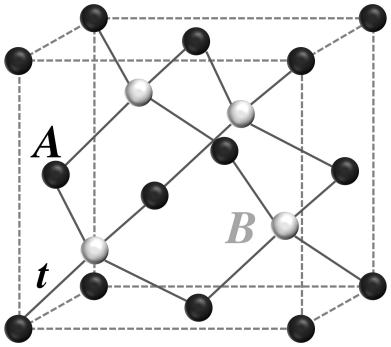

Figure D1 : The unit cell of the diamond lattice showing the two fcc sublattices A, B and the fermion hopping amplitude t along the nearest-neighbor bonds.

In Ref [117, 116], we proposed a periodic Anderson model on the diamond lattice (Fig. D1) of the form

$$\mathcal{H}_{\rm PAM} = \mathcal{H}_c + \mathcal{H}_d + \mathcal{H}_{cd}, \tag{D-1}$$

$$\mathcal{H}_c = t\sum_{\langle ij\rangle,\sigma}\left(c^\dagger_{i\sigma}c_{j\sigma} + \text{H.c.}\right) - \mu\sum_{i,\sigma} n^c_{i\sigma} + i\lambda\sum_{\langle\langle ij\rangle\rangle}\left[c^\dagger_{i\sigma}\left(\boldsymbol{\sigma}\cdot\mathbf{e}_{ij}\right)c_{j\sigma} - \text{H.c.}\right] + m\sum_{j,\sigma}(-1)^j c^\dagger_{j\sigma}c_{j\sigma}, \tag{D-2}$$

$$\mathcal{H}_d = E_d\sum_{i,\sigma} n^d_{i\sigma} + \mathcal{U}\sum_i n^d_{i\uparrow}n^d_{i\downarrow}, \tag{D-3}$$

$$\mathcal{H}_{cd} = V\sum_{i,\sigma}(c^\dagger_{i\sigma}d_{i\sigma} + \text{H.c.}). \tag{D-4}$$

It has the usual components of an Anderson lattice model. The d-operators describe the physical $4f$-electrons; their highly localized wavefunctions can be well treated in an atomic limit, with an energy level E_d and a mutual Coulomb interaction that assigns an energy penalty $\mathcal{U}$ to double occupation in Eq. D-3. The c-operators represent the *spd*-conduction electrons in the system, albeit with spin-orbit coupling (λ) and a sublattice-dependent term m which breaks IS. Finally there is uniform on-site hybridization between the localized and free conduction electrons of Eq. D-4, which is in the Kondo limit for large $\mathcal{U}$, with a Kondo coupling $J_K \sim V^2/|E_d|$.

We studied the model with $n_d + n_c = 1$ per site, corresponding to a quarter filling. To analyze the model in the strong-coupling limit ($\mathcal{U}/t \to \infty$), we implemented an auxiliary boson representation to effectively treat the Coulomb repulsion as fixing the localized electrons' density. When the Kondo coupling vanishes (via the hybridization $V \to 0$), an electron occupies the d-level, forming a Mott insulator, and the conduction electron bands are empty, leading to a topologically trivial state. In the Kondo-screened state (for V above a threshold value V_c), however, strongly renormalized Weyl nodes emerge and are pinned at the Fermi energy. This shows that the localized electron species play a central role in the formation of the Weyl nodes, which have a narrow bandwidth on the order of the Kondo temperature (T_K), a nodal velocity (v^*) that is reduced from a normal metal value (v) by several orders of magnitude, and the strong coupling from the localized electrons renormalizes the bands to fulfill the density constraint.

These characteristics are manifested in heavy fermion semimetals through several thermodynamic and transport signatures. The specific heat behaves as $c_v = \Gamma T^3$ with $\Gamma \propto (v/v^*)^3$ at an onset temperature of T_K (well-below the Debye temperature for phonons). This result is robust to residual interactions (Ref. [117], supporting information). This behavior was observed in specific heat measurements on $Ce_3Bi_4Pd_3$ [137]. In Ref. [162], $Ce_3Bi_4Pd_3$ was found to have a giant spontaneous Hall effect in the nonmagnetic phase without application of a magnetic field (TRS is preserved in the absence of a driving electric field), and a Hall resistivity that is even with respect to the magnetic field. Thus there has been substantial progess in studying heavy fermion semimetals which preserve TRS in non-centrosymmetric systems. Related observations have been reported in YbPtBi [153].

The IS-broken Weyl semimetal phases are generally well studied and understood as arising from a combination of crystalline and non-spatial symmetries, and has thus far been a major focus on studies of topological materials. We now shift our attention to topological semimetal phases that are not protected by TRS.

D1.3 The effect of breaking both time-reversal and inversion symmetries

Recent experimental studies [170] have used a magnetic field to tune and eventually annihilate the Weyl nodes of $Ce_3Bi_4Pd_3$. We are interested in understanding the behavior of this material, especially how the TRS breaking term controls its Weyl nodes. Since this issue is completely open, we will start by focusing on the symmetry aspects of the problem, namely how the Weyl nodes evolve from the Brillouin zone (BZ) boundary to its interior and their eventual annihilation, as the degrees of IS and TRS breaking are tuned. As a first step in the understanding, we will focus on the single fermion flavor model. Because the space-group symmetry is expected to play an important role in this evolution, we expect that the qualitative aspect of our results on the control of the Weyl nodes by the IS and TRS breaking potentials will be relevant to the full Kondo lattice model.

Thus, we consider the model $\mathcal{H}_c$ in the presence of a Zeeman coupling. The effect of breaking TRS but preserving the IS was reported in Ref. [117] (supporting information). There it was found that a Weyl semimetal phase evolves in two stages, with nodes occurring in the BZ interior instead of the BZ boundary.

Here, we study a variation on the conduction electron-only model by including terms that break both IS and TRS. We tune the symmetry-breaking terms to map out a phase diagram and find three distinct WSM phases, separated by critical phase boundary lines of distinct quadratic-band touching phases.

We consider $\mathcal{H}_c$ defined earlier on the diamond lattice in Fig. D1, with the addition of a Zeeman coupling:

$$\mathcal{H} = \mathcal{H}_c + M_z \sum_i \hat{z} \cdot \left(c^\dagger_{i\sigma} \boldsymbol{\sigma} c_{i\sigma} \right). \tag{D-5}$$

As already specified in Eq. D-2, the onsite potential $+m(-m)$ on the $A(B)$ sublattice breaks IS on the diamond lattice and reduces the space group from #227 ($Fd\bar{3}m$) to #216 ($F\bar{4}3m$, zincblende). The Zeeman term tuned by M_z breaks TRS. In this work, we fix $\lambda = 1/2$ to facilitate band inversion as a necessary (but insufficient) condition

towards a topological semimetal state.

The eigenenergies are obtained by diagonalizing the Bloch Hamiltonian. Although the full dispersion is analytically tractable, it is simpler to look at the eigenenergies when $M_z = 0,\ m \neq 0$ and vice versa. These are:

$$\varepsilon^{\alpha}_{\beta}(M_z = 0) = \alpha\sqrt{u_1^2 + u_2^2 + (m + \beta\lambda D_{\mathbf{k}})^2}, \tag{D-6}$$

$$\varepsilon^{\alpha}_{\beta}(m = 0) = \alpha\sqrt{u_1^2 + u_2^2 + \lambda^2 D_{\mathbf{k}}^2 + M_z^2 + 2\beta M_z\sqrt{u_1^2 + u_2^2 + \lambda^2 D_z^2}}, \tag{D-7}$$

where $\alpha, \beta = \pm 1$ index the four resulting bands, and $D_{\mathbf{k}} = \sqrt{\mathbf{D}(\boldsymbol{k}) \cdot \mathbf{D}(\boldsymbol{k})} = \sqrt{D_x^2 + D_y^2 + D_z^2}$. The notations are described in detail in Ref [117]. We immediately see that m competes with the spin orbit coupling term, whereas M_z competes with the $z-$component of the spin orbit interaction and the $u_1,\ u_2$ terms that come from the hopping terms proportional to t.

D1.4 Phase diagram: TRS- and IS-breaking coexistence and competition

We now describe the phases we encounter as we tune $M_z, m \geq 0$, as shown in Fig. D2. Note that these phases are symmetric with respect to the signs of M_z and m.

When TRS and IS are preserved ($M_z = m = 0$), this model realizes a Dirac semimetal, labeled at the origin of the phase diagram. In this phase, fourfold degenerate Dirac nodes are protected by nonsymmorphic symmetries at the X-points $\boldsymbol{k}_X = 2\pi\hat{r}$, which are time-reversal invariant momenta (TRIM). The Dirac point represents a critical point of the Fu-Kane-Mele model's phase diagram of topological insulators [62], which has been extended to WSM phases through IS breaking terms [166, 87].

Generically, the addition of TRS or IS breaking terms will split Dirac nodal points into one or more pairs of Weyl nodes, which is precisely what happens in our model. The next subsections explain the WSM phases and the boundaries between them in terms of which high symmetry lines contain Weyl nodes or quadratic band touching points. In Fig. D3(a) we show the fcc BZ with its high symmetry points and node

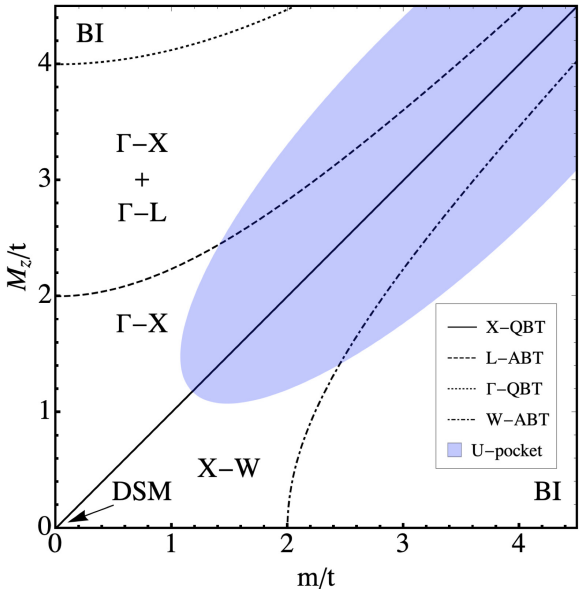

Figure D2 : Phase diagram for the WSM phases that our model captures with breaking both time-reversal and inversion symmetries. DSM=Dirac semimetal, BI=Band insulator, X/Γ-QBT = quadratic band touching at X or Γ, L/W-ABT=anisotropic band touching at L/W, and U-pocket denotes an approximate region where a Fermi pocket at U emerges and coexists with the labeled phases. The regions with labels of high symmetry lines are Weyl semimetals with the nodes found along those lines.

locations labeled for an example phase, as well as the [011] plane along which we plot the dispersion of the $\Gamma - X + \Gamma - L$ Weyl semimetal (Sec. D1.4) in Fig. D3(b).

$X - W$ Weyl semimetal

The $M_z = m > 0$ phase boundary (Fig. D2 solid line) marks a massful semimetal with a fourfold-degenerate quadratic band touching point at X, labeled $X - QBT$. When $M_z < m$ and m is small, the quadratic bands split into two pairs of Weyl nodes, and move along the $X - W$ lines, coexisting with the Zeeman field as long as $\sqrt{m^2 - 4} < M_z < m$. As m increases, the Weyl nodes move towards the W points, until the $W - ABT$ boundary (dashed-dotted line of bottom bound $M_z = \sqrt{m^2 - 4}$). Along this boundary, an anisotropic band touching occurs at W, with linear dispersion in the $W - U$ direction and quadratic along $X - W$, marking a critical line between

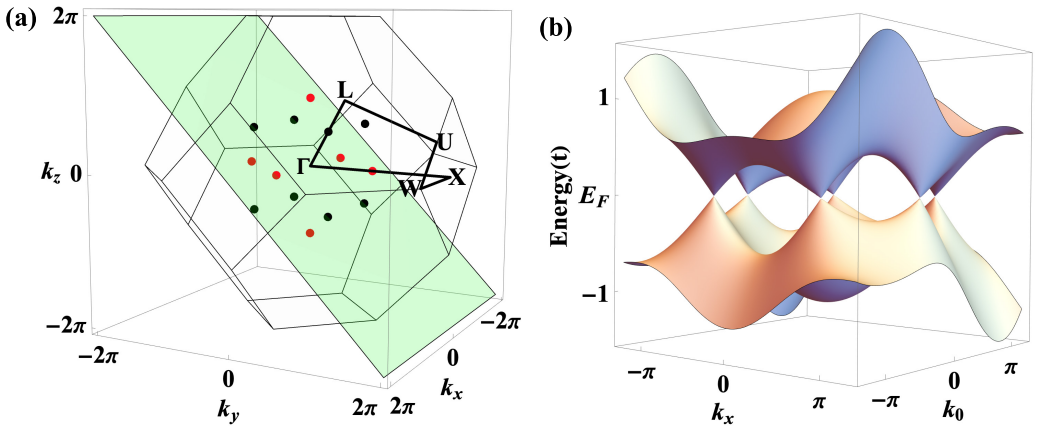

Figure D3 : (a) Locations in the Brillouin zone where Weyl nodes appear for $M_z = 3$, $m = 1$. High symmetry points are labeled, and Weyl node colors are red for $\Gamma - X$, black for $\Gamma - L$. The [011] plane that intersects $\Gamma - X$ and $\Gamma - L$ nodes is shown in green. (b) Eigenenergy dispersion projected onto the [011] plane shown in green in (a) that intersects with the $\Gamma - X$ and $\Gamma - L$ nodes.

semimetal and trivial [87] band insulator (BI).

$\Gamma - X$ Weyl semimetal

When $M_z > m \neq 0$, the $X - QBT$ bands split into Weyl nodes along $\Gamma - X$. Here a WSM phase distinct from the $X - W$ WSM phase emerges, with the restriction that $m < M_z < \sqrt{m^2 + 4}$. Because there are six $\Gamma - X$ lines, this produces three pairs of nodal points in the BZ.

The upper bound $M_z = \sqrt{m^2 + 4}$ marks the $L - ABT$ phase boundary marking an anisotropic band touching at the L point, dotted line in Fig. D2). Here, a quadratic touching along the $\Gamma - L$ line meets a linear dispersion along $L - U$.

$\Gamma - X + \Gamma - L$ Weyl semimetal

As one moves in parameter space above the $L - ABT$ line, new Weyl points evolve from the critical touching at L, where linearly dispersing nodes travel along the $\Gamma - L$ line. These new nodes coexist with the $\Gamma - X$ nodes, and their semimetal phase

persists as long as M_z is between $\sqrt{m^2+4} < M_z < \sqrt{m^2+16}$. The eigenenergies of this phase are plotted in Fig. D3(b), in the [011] plane, where one can see both sets of nodes along $\Gamma - X$ and $\Gamma - L$.

The $\Gamma - QBT$ phase boundary ($M_z = \sqrt{m^2+16}$) is marked by a dotted line in Fig. D2. Along this boundary, the nodes from $\Gamma - X$ lines and $\Gamma - L$ lines all meet at Γ and become a single, twofold degenerate quadratic band touching, labeled $\Gamma - QBT$. As the Zeeman field is increased, a band gap opens, and the system becomes an insulator.

$U-$Fermi surface coexistence metallic phase

Finally, a last phase diagram feature warrants analysis, namely the "U-pocket" region approximately represented in blue. When both the Zeeman splitting and the sublattice symmetry breaking are larger and close enough to each other, a Fermi pocket gradually emerges as a Fermi surface at U as $M_z \sim m$ increases. This metallic pocket does not eliminate most nodal point features or phase boundaries, except for those close to the $L - ABT$ boundary for large values of $M_z \sim 4$.

D1.5 Discussion and Summary

Our main result is the phase diagram shown in Fig. D2 as a function of the Zeeman coupling M_z and the IS-breaking potential m. Within our model, the Weyl semimetal phases survive the combined breaking of TRS and IS, and when the Zeeman term and the sublattice potential are larger and similar in size, a Lifshitz transition occurs where a hole pocket emerges at the U point of the Brillouin zone.

The most important phase boundary is the $X - QBT$ line for balanced $M_z = m$, because it evolves from the critical point of the Fu-Kane-Mele model which serves as the multi-dimensional intersection of several nonlocal and space group symmetries. For this reason, it represents a nexus of many phases. In our work's two-dimensional slice of the phase diagram, the $X - QBT$ boundary marks a change from nonsymmor-

phic symmetry-driven nodal degeneracy, enforced to exist on the BZ *boundary* (e.g. the $X - W$ WSM), to where the TRS-breaking terms dominate and nodal phases evolve along high symmetry lines within the *interior* of the BZ.

The phase boundaries are critical lines where the Weyl nodes become quadratic band touching at a high-symmetry point, just before the nodes annihilate or follow a different high symmetry line, depending on the neighboring phase.

In a full treatment of the Anderson lattice model, the f-electrons should be more responsive to the Zeeman field than the conduction electrons. In turn, this is expected to directly connect with the recent experiments [170] on the tuning of the Kondo-driven Weyl nodes by a magnetic field.

Bibliography

[1] A. C. Hewson, *The Kondo Problem to Heavy Fermions*. Cambridge University Press, 2003.

[2] P. Coleman, "Heavy fermions: electrons at the edge of magnetism." [cond-mat.str-el], January 2007.

[3] Q. Si, "Quantum criticality and the kondo lattice," in *Understanding Quantum Phase Transitions* (L. D. Carr, ed.), pp. 193–213, CRC Press, 2011.

[4] S. Kirchner, S. Paschen, Q. Chen, S. Wirth, D. Feng, J. D. Thompson, and Q. Si, "Colloquium: Heavy-electron quantum criticality and single-particle spectroscopy," *Rev. Mod. Phys.*, vol. 92, p. 011002, Mar 2020.

[5] Q. Si and F. Steglich, "Heavy fermions and quantum phase transitions," *Science*, vol. 329, no. 5996, pp. 1161–1166, 2010.

[6] S. Sachdev, *Quantum Phase Transitions*. Cambridge University Press, 2nd ed., 2011.

[7] H. J. Schulz, "Fermi liquids and non-fermi liquids." Arxiv, March 1995.

[8] P. Coleman, C. Pépin, Q. Si, and R. Ramazashvili, "How do fermi liquids get heavy and die?," *Journal of Physics: Condensed Matter*, vol. 13, no. 35, p. R723, 2001.

[9] P. W. Anderson and G. Yuval, "Exact results in the kondo problem: Equivalence to a classical one-dimensional coulomb gas," *Phys. Rev. Lett.*, vol. 23, pp. 89–92, Jul 1969.

[10] G. Yuval and P. W. Anderson, "Exact results for the kondo problem: One-body theory and extension to finite temperature," *Phys. Rev. B*, vol. 1, pp. 1522–1528, Feb 1970.

[11] P. W. Anderson and G. Yuval, "Some numerical results on the kondo problem and the inverse square one-dimensional ising model," *Journal of Physics C: Solid State Physics*, vol. 4, pp. 607–620, apr 1971.

[12] K. G. Wilson, "The renormalization group: Critical phenomena and the kondo problem," *Rev. Mod. Phys.*, vol. 47, pp. 773–840, Oct 1975.

[13] M. P. Marder, *Condensed Matter Physics*. John Wiley & Sons Inc., 2000.

[14] D. Neilson, "Landau fermi liquid theory," *Australian journal of physics*, vol. 49, no. 1, pp. 79–102, 1996.

[15] S. Sykora and K. W. Becker, "Heavy fermion properties of the kondo lattice model," *Scientific Reports*, vol. 3, pp. 1–6, September 2013.

[16] S. Paschen, T. Lühmann, S. Wirth, P. Gegenwart, O. Trovarelli, C. Geibel, F. Steglich, P. Coleman, and Q. Si, "Hall-effect evolution across a heavy-fermion quantum critical point," *Nature*, vol. 432, p. 881, 2004.

[17] Q. Si and S. Paschen, "Quantum phase transitions in heavy fermion metals and Kondo insulators," *Physica Stat. Solidi B*, vol. 250, no. 3, pp. 425–438, 2013.

[18] S. Nair, S. Wirth, S. Friedemann, F. Steglich, Q. Si, and A. J. Schofield, "Hall effect in heavy fermion metals," *Advances in Physics*, vol. 61, no. 5, pp. 583–664, 2012.

[19] J. Smit, "The spontaneous hall effect in ferromagnetics i," *Physica*, vol. 21, no. 6, pp. 877 – 887, 1955.

[20] J. Smit, "The spontaneous hall effect in ferromagnetics ii," *Physica*, vol. 24, no. 1, pp. 39 – 51, 1958.

[21] R. Karplus and J. M. Luttinger, "Hall effect in ferromagnetics," *Phys. Rev.*, vol. 95, pp. 1154–1160, Sep 1954.

[22] N. Nagaosa, J. Sinova, S. Onoda, A. H. MacDonald, and N. P. Ong, "Anomalous hall effect," *Rev. Mod. Phys.*, vol. 82, pp. 1539–1592, May 2010.

[23] T. Jungwirth, Q. Niu, and A. H. MacDonald, "Anomalous hall effect in ferromagnetic semiconductors," *Phys. Rev. Lett.*, vol. 88, p. 207208, May 2002.

[24] M. Onoda and N. Nagaosa, "Topological nature of anomalous hall effect in ferromagnets," *Journal of the Physical Society of Japan*, vol. 71, no. 1, pp. 19–22, 2002.

[25] F. D. M. Haldane, "Berry curvature on the fermi surface: Anomalous hall effect as a topological fermi-liquid property," *Phys. Rev. Lett.*, vol. 93, p. 206602, Nov 2004.

[26] J. Kondo, "Resistance minimum in dilute magnetic alloys," *Prog. Theor. Phys.*, vol. 32, no. 1, pp. 37–49, 1964.

[27] J. Kondo, "Anomalous hall effect and magnetoresistance of ferromagnetic metals," *Progress of Theoretical Physics*, vol. 27, no. 4, pp. 772–792, 1962.

[28] M. A. Ruderman and C. Kittel, "Indirect exchange coupling of nuclear magnetic moments by conduction electrons," *Phys. Rev.*, vol. 96, pp. 99–102, Oct 1954.

[29] T. Kasuya, "A theory of metallic ferro-and antiferromagnetism on zener's model," *Progress of theoretical physics*, vol. 16, no. 1, pp. 45–57, 1956.

[30] K. Yosida, "Magnetic properties of cu-mn alloys," *Phys. Rev.*, vol. 106, pp. 893–898, Jun 1957.

[31] Q. Si, "Global magnetic phase diagram and local quantum criticality in heavy fermion metals," *Physica B: Condensed Matter*, vol. 378-380, pp. 23 – 27, 2006.

[32] Q. Si, "Quantum criticality and global phase diagram of magnetic heavy fermions," *Phys. Status Solidi B*, vol. 247, no. 3, pp. 476–484, 2010.

[33] J. Custers, K.-A. Lorenzer, M. Müller, A. Prokofiev, A. Sidorenko, H. Winkler, A. M. Strydom, Y. Shimura, T. Sakakibara, R. Yu, Q. Si, and S. Paschen, "Destruction of the Kondo effect in the cubic heavy-fermion compound $Ce_3Pd_{20}Si_6$," *Nature Materials*, vol. 11, p. 189, 2012.

[34] L. Jiao, Y. Chen, Y. Kohama, D. Graf, E. D. Bauer, J. Singleton, J.-X. Zhu, Z. Weng, G. Pang, T. Shang, J. Zhang, H.-O. Lee, T. Park, M. Jaime, J. D. Thompson, F. Steglich, Q. Si, and H. Q. Yuan, "Fermi surface reconstruction and multiple quantum phase transitions in the antiferromagnet $CeRhIn_5$," *Proceedings of the National Academy of Sciences*, vol. 112, no. 3, pp. 673–678, 2015.

[35] Y. Luo, X. Lu, A. P. Dioguardi, P. S. F. Rosa, E. D. Bauer, Q. Si, and J. D. Thompson, "Unconventional and conventional quantum criticalities in $CeRh_{0.58}Ir_{0.42}In_5$," *npj Quantum Materials*, vol. 3, no. 1, p. 6, 2018.

[36] H. Zhao, J. Zhang, M. Lyu, S. Bachus, Y. Tokiwa, P. Gegenwart, S. Zhang, J. Cheng, Y.-f. Yang, G. Chen, Y. Isikawa, Q. Si, F. Steglich, and P. Sun, "Quantum-critical phase from frustrated magnetism in a strongly correlated metal," *Nature Physics*, vol. 15, no. 12, pp. 1261–1266, 2019.

[37] S. J. Yamamoto and Q. Si, "Global phase diagram of the kondo lattice: From heavy fermion metals to kondo insulators," *Journal of Low Temperature Physics*, vol. 161, pp. 233–262, Oct 2010.

[38] P. Coleman and A. H. Nevidomskyy, "Frustration and the kondo effect in

heavy fermion materials," *Journal of Low Temperature Physics*, vol. 161, no. 1, pp. 182–202, 2010.

[39] H. Shishido, R. Settai, H. Harima, and Y. Ōnuki, "A drastic change of the fermi surface at a critical pressure in $CeRhIn_5$: dhva study under pressure," *J. Phys. Soc. Jpn.*, vol. 74, pp. 1103–1106, 2005.

[40] J. A. Hertz, "Quantum critical phenomena," *Phys. Rev. B*, vol. 14, pp. 1165–1184, Aug 1976.

[41] T. Moriya, "Spin fluctuations in itinerant electron magnetism," *Springer series in solid-state sciences*, vol. 56, 1985.

[42] A. J. Millis, "Effect of a nonzero temperature on quantum critical points in itinerant fermion systems," *Phys. Rev. B*, vol. 48, pp. 7183–7196, Sep 1993.

[43] V. Martelli, A. Cai, E. M. Nica, M. Taupin, A. Prokofiev, C.-C. Liu, H.-H. Lai, R. Yu, K. Ingersent, R. Küchler, A. M. Strydom, D. Geiger, J. Haenel, J. Larrea, Q. Si, and S. Paschen, "Sequential localization of a complex electron fluid," *Proceedings of the National Academy of Sciences*, vol. 116, no. 36, pp. 17701–17706, 2019.

[44] S. Lucas, K. Grube, C.-L. Huang, A. Sakai, S. Wunderlich, E. L. Green, J. Wosnitza, V. Fritsch, P. Gegenwart, O. Stockert, *et al.*, "Entropy evolution in the magnetic phases of partially frustrated cepdal," *Physical Review Letters*, vol. 118, p. 107204, Mar 2017.

[45] J. G. Rau, E. K.-H. Lee, and H.-Y. Kee, "Spin-orbit physics giving rise to novel phases in correlated systems: Iridates and related materials," *Annual Review of Condensed Matter Physics*, vol. 7, no. 1, pp. 195–221, 2016.

[46] D. F. Agterberg, P. A. Frigeri, R. P. Kaur, A. Koga, and M. Sigrist, "Magnetic fields and superconductivity without inversion symmetry in cept3si," *Physica*

B: Condensed Matter, vol. 378-380, pp. 351 – 354, 2006. Proceedings of the International Conference on Strongly Correlated Electron Systems.

[47] E. Bauer, G. Hilscher, H. Michor, C. Paul, E. W. Scheidt, A. Gribanov, Y. Seropegin, H. Noël, M. Sigrist, and P. Rogl, "Heavy fermion superconductivity and magnetic order in noncentrosymmetric cept$_3$Si," *Phys. Rev. Lett.*, vol. 92, p. 027003, Jan 2004.

[48] L. P. Gor'kov and E. I. Rashba, "Superconducting 2d system with lifted spin degeneracy: Mixed singlet-triplet state," *Phys. Rev. Lett.*, vol. 87, p. 037004, Jul 2001.

[49] F. Steglich and S. Wirth, "Foundations of heavy-fermion superconductivity: lattice Kondo effect and Mott physics," *Reports on Progress in Physics*, vol. 79, p. 084502, 7 2016.

[50] Y. X. Zhao and A. P. Schnyder, "Nonsymmorphic symmetry-required band crossings in topological semimetals," *Phys. Rev. B*, vol. 94, p. 195109, Nov 2016.

[51] C.-K. Chiu, J. C. Y. Teo, A. P. Schnyder, and S. Ryu, "Classification of topological quantum matter with symmetries," *Rev. Mod. Phys.*, vol. 88, p. 035005, Aug 2016.

[52] C. Fang, Y. Chen, H.-Y. Kee, and L. Fu, "Topological nodal line semimetals with and without spin-orbital coupling," *Physical Review B*, vol. 92, no. 8, p. 081201, 2015.

[53] J. Wang, Y. Liu, K.-H. Jin, X. Sui, L. Zhang, W. Duan, F. Liu, and B. Huang, "Pseudo dirac nodal sphere semimetal," *Phys. Rev. B*, vol. 98, p. 201112, Nov 2018.

[54] T. Bzdušek and M. Sigrist, "Robust doubly charged nodal lines and nodal surfaces in centrosymmetric systems," *Physical Review B*, vol. 96, no. 15, p. 155105, 2017.

[55] S.-Y. Yang, H. Yang, E. Derunova, S. S. P. Parkin, B. Yan, and M. N. Ali, "Symmetry demanded topological nodal-line materials," *Advances in Physics: X*, vol. 3, no. 1, p. 1414631, 2018.

[56] M. Dzero, K. Sun, P. Coleman, and V. Galitski, "Theory of topological kondo insulators," *Phys. Rev. B*, vol. 85, p. 045130, Jan 2012.

[57] M. Dzero, K. Sun, V. Galitski, and P. Coleman, "Topological kondo insulators," *Phys. Rev. Lett.*, vol. 104, p. 106408, Mar 2010.

[58] C.-H. Min, P. Lutz, S. Fiedler, B. Y. Kang, B. K. Cho, H.-D. Kim, H. Bentmann, and F. Reinert, "Importance of charge fluctuations for the topological phase in smb_6," *Phys. Rev. Lett.*, vol. 112, p. 226402, Jun 2014.

[59] M. Legner, A. Rüegg, and M. Sigrist, "Topological invariants, surface states, and interaction-driven phase transitions in correlated kondo insulators with cubic symmetry," *Phys. Rev. B*, vol. 89, p. 085110, Feb 2014.

[60] P. Coleman, *Introduction to Many-Body Physics*. Cambridge University Press, 2015.

[61] X.-Y. Feng, J. Dai, C.-H. Chung, and Q. Si, "Competing topological and kondo insulator phases on a honeycomb lattice," *Phys. Rev. Lett.*, vol. 111, p. 016402, Jul 2013.

[62] L. Fu, C. L. Kane, and E. J. Mele, "Topological insulators in three dimensions," *Phys. Rev. Lett.*, vol. 98, p. 106803, Mar 2007.

[63] C. Lacroix, P. Mendels, and F. Mila, *Introduction to frustrated magnetism: materials, experiments, theory*, vol. 164. Springer Science & Business Media, 2011.

[64] A. Auerbach, *Interacting Electrons and Quantum Magnetism*. Springer, 1998.

[65] W. Nolting and A. Ramakanth, *Quantum Theory of Magnetism*. Springer-Verlag Berlin Heidelberg, 2009.

[66] J. Chalker, "Quantum theory of condensed matter, lecture notes." Online, 2013-14. p. 17.

[67] T. Giamarchi, *Understanding Quantum Phase Transitions*, ch. 12: Quantum Phase Transitions in Quasi-One-Dimensional Systems, pp. 289–309. CRC press, 2010.

[68] G. Baskaran, Z. Zou, and P. Anderson, "The resonating valence bond state and high-tc superconductivity - a mean field theory," *Solid State Communications*, vol. 63, no. 11, pp. 973 – 976, 1987.

[69] S. A. Kivelson, D. S. Rokhsar, and J. P. Sethna, "Topology of the resonating valence-bond state: Solitons and high-tc superconductivity," *Phys. Rev. B*, vol. 35, p. 8865, 1987.

[70] R. Moessner, S. L. Sondhi, and E. Fradkin, "Short-ranged resonating valence bond physics, quantum dimer models, and ising gauge theories," *Phys. Rev. B*, vol. 65, p. 024504, Dec 2001.

[71] R. Moessner and S. L. Sondhi, "Resonating valence bond phase in the triangular lattice quantum dimer model," *Phys. Rev. Lett.*, vol. 86, pp. 1881–1884, Feb 2001.

[72] N. Read and B. Chakraborty, "Statistics of the excitations of the resonating-valence-bond state," *Phys. Rev. B*, vol. 40, p. 7133, 1989.

[73] F. Ferrari, S. Bieri, and F. Becca, "Competition between spin liquids and valence-bond order in the frustrated spin-$\frac{1}{2}$ heisenberg model on the honeycomb lattice," *Phys. Rev. B*, vol. 96, p. 104401, Sep 2017.

[74] X. G. Wen, F. Wilczek, and A. Zee, "Chiral spin states and superconductivity," *Phys. Rev. B*, vol. 39, pp. 11413–11423, Jun 1989.

[75] I. Affleck and J. B. Marston, "Large-n limit of the heisenberg-hubbard model: Implications for high-tc superconductors," *Phys. Rev. B*, vol. 37, pp. 3774–3777, Mar 1988.

[76] G. Kotliar, "Resonating valence bonds and d-wave superconductivity," *Phys. Rev. B*, vol. 37, pp. 3664–3666, Mar 1988.

[77] E. Fradkin, *Field theories of condensed matter physics*. Cambridge University Press, 2 ed., March 2013.

[78] S. Murakami, M. Hirayama, R. Okugawa, and T. Miyake, "Emergence of topological semimetals in gap closing in semiconductors without inversion symmetry," *Sci Adv*, vol. 3, p. e1602680, May 2017.

[79] C. Bradley and A. Cracknell, *The mathematical theory of symmetry in solids: representation theory for point groups and space groups*. Oxford University Press, 2010.

[80] S. M. Young and C. L. Kane, "Dirac semimetals in two dimensions," *Phys. Rev. Lett.*, vol. 115, p. 126803, Sep 2015.

[81] Z. Zhu, Y. Cheng, and U. Schwingenschlögl, "Band inversion mechanism in topological insulators: A guideline for materials design," *Phys. Rev. B*, vol. 85, p. 235401, Jun 2012.

[82] C. L. Kane and E. J. Mele, "Z_2 topological order and the quantum spin hall effect," *Phys. Rev. Lett.*, vol. 95, p. 146802, Sep 2005.

[83] C. L. Kane and E. J. Mele, "Quantum spin hall effect in graphene," *Phys. Rev. Lett.*, vol. 95, p. 226801, Nov 2005.

[84] S. M. Young, S. Zaheer, J. C. Y. Teo, C. L. Kane, E. J. Mele, and A. M. Rappe, "Dirac semimetal in three dimensions," *Phys. Rev. Lett.*, vol. 108, p. 140405, Apr 2012.

[85] A. Burkov, "Weyl metals," *Annual Review of Condensed Matter Physics*, vol. 9, no. 1, pp. 359–378, 2018.

[86] N. P. Armitage, E. J. Mele, and A. Vishwanath, "Weyl and dirac semimetals in three-dimensional solids," *Rev. Mod. Phys.*, vol. 90, p. 015001, Jan 2018.

[87] T. Ojanen, "Helical fermi arcs and surface states in time-reversal invariant weyl semimetals," *Phys. Rev. B*, vol. 87, p. 245112, Jun 2013.

[88] L. Lepori, I. C. Fulga, A. Trombettoni, and M. Burrello, "*pt*-invariant weyl semimetals in gauge-symmetric systems," *Phys. Rev. B*, vol. 94, p. 085107, Aug 2016.

[89] A. Zyuzin, S. Wu, and A. Burkov, "Weyl semimetal with broken time reversal and inversion symmetries," *Physical Review B*, vol. 85, no. 16, p. 165110, 2012.

[90] H. Watanabe, H. C. Po, M. P. Zaletel, and A. Vishwanath, "Filling-enforced gaplessness in band structures of the 230 space groups," *Phys. Rev. Lett.*, vol. 117, p. 096404, Aug 2016.

[91] J. Cano, B. Bradlyn, Z. Wang, L. Elcoro, M. G. Vergniory, C. Felser, M. I. Aroyo, and B. A. Bernevig, "Building blocks of topological quantum chemistry: Elementary band representations," *Phys. Rev. B*, vol. 97, p. 035139, Jan 2018.

[92] B. Bradlyn, L. Elcoro, J. Cano, M. Vergniory, Z. Wang, C. Felser, M. Aroyo, and B. A. Bernevig, "Topological quantum chemistry," *Nature (London)*, vol. 547, no. 7663, p. 298, 2017.

[93] P. Coleman and A. J. Schofield, "Quantum criticality," *Nature*, vol. 433, pp. 226–229, Jan 2005.

[94] P. Gegenwart, Q. Si, and F. Steglich, "Quantum criticality in heavy-fermion metals," *nature physics*, vol. 4, no. 3, pp. 186–197, 2008.

[95] M. S. Kim and M. C. Aronson, "Spin liquids and antiferromagnetic order in the shastry-sutherland-lattice compound yb_2pt_2Pb," *Phys. Rev. Lett.*, vol. 110, p. 017201, Jan 2013.

[96] E. D. Mun, S. L. Bud'ko, C. Martin, H. Kim, M. A. Tanatar, J.-H. Park, T. Murphy, G. M. Schmiedeshoff, N. Dilley, R. Prozorov, and P. C. Canfield, "Magnetic-field-tuned quantum criticality of the heavy-fermion system ybptbi," *Phys. Rev. B*, vol. 87, p. 075120, Feb 2013.

[97] V. Fritsch, N. Bagrets, G. Goll, W. Kittler, M. J. Wolf, K. Grube, C.-L. Huang, and H. v. Löhneysen, "Approaching quantum criticality in a partially geometrically frustrated heavy-fermion metal," *Phys. Rev. B*, vol. 89, p. 054416, Feb 2014.

[98] Y. Tokiwa, C. Stingl, M.-S. Kim, T. Takabatake, and P. Gegenwart, "Characteristic signatures of quantum criticality driven by geometrical frustration," *Science Advances*, vol. 1, no. 3, p. e1500001, 2015.

[99] S. Nakatsuji, Y. Machida, Y. Maeno, T. Tayama, T. Sakakibara, J. v. Duijn, L. Balicas, J. N. Millican, R. T. Macaluso, and J. Y. Chan, "Metallic spin-liquid behavior of the geometrically frustrated kondo lattice $Pr_2Ir_2O_7$," *Phys. Rev. Lett.*, vol. 96, p. 087204, Mar 2006.

[100] Y. Machida, S. Nakatsuji, Y. Maeno, T. Tayama, T. Sakakibara, and S. Onoda, "Unconventional anomalous hall effect enhanced by a noncoplanar spin texture in the frustrated kondo lattice $Pr_2Ir_2O_7$," *Phys. Rev. Lett.*, vol. 98, p. 057203, Jan 2007.

[101] Y. Machida, S. Nakatsuji, S. Onoda, T. Tayama, and T. Sakakibara, "Time-reversal symmetry breaking and spontaneous hall effect without magnetic dipole order," *Nature*, vol. 463, no. 7278, pp. 210–213, 2010.

[102] G. Chen and M. Hermele, "Magnetic orders and topological phases from f-d exchange in pyrochlore iridates," *Phys. Rev. B*, vol. 86, p. 235129, Dec 2012.

[103] R. Flint and T. Senthil, "Chiral rkky interaction in $\mathrm{pr_2ir_2o_7}$," *Phys. Rev. B*, vol. 87, p. 125147, Mar 2013.

[104] S. Lee, A. Paramekanti, and Y. B. Kim, "Rkky interactions and the anomalous hall effect in metallic rare-earth pyrochlores," *Phys. Rev. Lett.*, vol. 111, p. 196601, Nov 2013.

[105] E.-G. Moon, C. Xu, Y. B. Kim, and L. Balents, "Non-fermi-liquid and topological states with strong spin-orbit coupling," *Phys. Rev. Lett.*, vol. 111, p. 206401, Nov 2013.

[106] L. Savary, E.-G. Moon, and L. Balents, "New type of quantum criticality in the pyrochlore iridates," *Phys. Rev. X*, vol. 4, p. 041027, Nov 2014.

[107] M. Udagawa and R. Moessner, "Anomalous hall effect from frustration-tuned scalar chirality distribution in $\mathrm{pr_2ir_2o_7}$," *Phys. Rev. Lett.*, vol. 111, p. 036602, Jul 2013.

[108] A. Kalitsov, B. Canals, and C. Lacroix, "Anomalous hall effect due to magnetic chirality in the pyrochlore lattice," *Journal of Physics: Conference Series*, vol. 145, p. 012020, jan 2009.

[109] J. G. Rau and H.-Y. Kee, "Symmetry breaking via hybridization with conduction electrons in frustrated kondo lattices," *Phys. Rev. B*, vol. 89, p. 075128, Feb 2014.

[110] Y. Tokiwa, J. J. Ishikawa, S. Nakatsuji, and P. Gegenwart, "Quantum criticality in a metallic spin liquid," *Nature Materials*, vol. 13, pp. 356–359, March 2014.

[111] S.-S. Gong, W. Zhu, and D. Sheng, "Emergent chiral spin liquid: fractional quantum hall effect in a kagome heisenberg model," *Scientific reports*, vol. 4, p. 6317, 2014.

[112] Y.-C. He, D. N. Sheng, and Y. Chen, "Chiral spin liquid in a frustrated anisotropic kagome heisenberg model," *Phys. Rev. Lett.*, vol. 112, p. 137202, Apr 2014.

[113] S. Bieri, L. Messio, B. Bernu, and C. Lhuillier, "Gapless chiral spin liquid in a kagome heisenberg model," *Phys. Rev. B*, vol. 92, p. 060407, Aug 2015.

[114] T. Kondo, M. Nakayama, R. Chen, J. J. Ishikawa, E. G. Moon, T. Yamamoto, Y. Ota, W. Malaeb, H. Kanai, Y. Nakashima, Y. Ishida, R. Yoshida, H. Yamamoto, M. Matsunami, S. Kimura, N. Inami, K. Ono, H. Kumigashira, S. Nakatsuji, L. Balents, and S. Shin, "Quadratic fermi node in a 3d strongly correlated semimetal," *Nature Communications*, vol. 6, no. 1, p. 10042, 2015.

[115] R. Kaneko, M.-T. Huebsch, S. Sakai, R. Arita, H. Shinaoka, K. Ueda, Y. Tokura, and J. Fujioka, "Enhanced thermopower in the correlated semimetallic phase of hole-doped pyrochlore iridates," *Phys. Rev. B*, vol. 99, p. 161104, Apr 2019.

[116] S. E. Grefe, H.-H. Lai, S. Paschen, and Q. Si, "Weyl-Kondo semimetals in nonsymmorphic systems," *Phys. Rev. B*, vol. 101, p. 075138, Feb 2020.

[117] H.-H. Lai, S. E. Grefe, S. Paschen, and Q. Si, "Weyl–Kondo semimetal in heavy-fermion systems," *Proceedings of the National Academy of Sciences*, vol. 115, p. 93, 01 2018.

[118] B. Cheng, T. Ohtsuki, D. Chaudhuri, S. Nakatsuji, M. Lippmaa, and N. P. Armitage, "Dielectric anomalies and interactions in the three-dimensional

quadratic band touching luttinger semimetal pr2ir2o7," *Nature Communications*, vol. 8, no. 1, p. 2097, 2017.

[119] K. Ueda, T. Oh, B.-J. Yang, R. Kaneko, J. Fujioka, N. Nagaosa, and Y. Tokura, "Magnetic-field induced multiple topological phases in pyrochlore iridates with mott criticality," *Nature Communications*, vol. 8, no. 1, p. 15515, 2017.

[120] K. Ueda, R. Kaneko, H. Ishizuka, J. Fujioka, N. Nagaosa, and Y. Tokura, "Spontaneous hall effect in the weyl semimetal candidate of all-in all-out pyrochlore iridate," *Nature Communications*, vol. 9, no. 1, p. 3032, 2018.

[121] H. Kumar, K. C. Kharkwal, K. Kumar, K. Asokan, A. Banerjee, and A. K. Pramanik, "Magnetic and transport properties of the pyrochlore iridates $(y_{1-x}pr_x)_2ir_2o_7$: Role of $f-d$ exchange interaction and $d-p$ orbital hybridization," *Phys. Rev. B*, vol. 101, p. 064405, Feb 2020.

[122] P. Streda, "Theory of quantised hall conductivity in two dimensions," *Journal of Physics C: Solid State Physics*, vol. 15, pp. L717–L721, aug 1982.

[123] F. J. Burnell, S. Chakravarty, and S. L. Sondhi, "Monopole flux state on the pyrochlore lattice," *Phys. Rev. B*, vol. 79, p. 144432, Apr 2009.

[124] N. A. Sinitsyn, A. H. MacDonald, T. Jungwirth, V. K. Dugaev, and J. Sinova, "Anomalous hall effect in a two-dimensional dirac band: The link between the kubo-streda formula and the semiclassical boltzmann equation approach," *Phys. Rev. B*, vol. 75, p. 045315, Jan 2007.

[125] P. Chandra, P. Coleman, and R. Flint, "Hastatic order in the heavy-fermion compound uru2si2," *Nature*, vol. 493, pp. 621–626, 2013.

[126] B. G. Ueland, C. F. Miclea, Y. Kato, O. Ayala-Valenzuela, R. D. McDonald, R. Okazaki, P. H. Tobash, M. A. Torrez, F. Ronning, R. Movshovich, Z. Fisk, E. D. Bauer, I. Martin, and J. D. Thompson, "Controllable chirality-induced

geometrical hall effect in a frustrated highly correlated metal," *Nature Communications*, vol. 3, no. 1, p. 1067, 2012.

[127] H. Shishido, T. Shibauchi, K. Yasu, T. Kato, H. Kontani, T. Terashima, and Y. Matsuda, "Tuning the dimensionality of the heavy fermion compound cein3," *Science*, vol. 327, no. 5968, pp. 980–983, 2010.

[128] S. K. Goh, Y. Mizukami, H. Shishido, D. Watanabe, S. Yasumoto, M. Shimozawa, M. Yamashita, T. Terashima, Y. Yanase, T. Shibauchi, A. I. Buzdin, and Y. Matsuda, "Anomalous upper critical field in cecoin$_5$/ybcoin$_5$ superlattices with a rashba-type heavy fermion interface," *Phys. Rev. Lett.*, vol. 109, p. 157006, Oct 2012.

[129] M. B. Maple and D. Wohlleben, "Nonmagnetic $4f$ shell in the high-pressure phase of sms," *Phys. Rev. Lett.*, vol. 27, pp. 511–515, Aug 1971.

[130] Y. Haga, J. Derr, A. Barla, B. Salce, G. Lapertot, I. Sheikin, K. Matsubayashi, N. K. Sato, and J. Flouquet, "Pressure-induced magnetic phase transition in gold-phase sms," *Phys. Rev. B*, vol. 70, p. 220406, Dec 2004.

[131] P. Wachter, "Chapter 132 intermediate valence and heavy fermions," in *Lanthanides/Actinides: Physics - II*, vol. 19 of *Handbook on the Physics and Chemistry of Rare Earths*, pp. 177 – 382, Elsevier, 1994.

[132] K. Matsubayashi, K. Imura, H. S. Suzuki, G. Chen, N. Mori, T. Nishioka, K. Deguchi, and N. K. Sato, "Pseudogap formation near at the border of an insulator–metal transition in sms," *Journal of the Physical Society of Japan*, vol. 76, no. 3, p. 033602, 2007.

[133] G. Aeppli and Z. Fisk, "Kondo insulators," *Comm. Condemns. Matter Phys.*, vol. 16, p. 155, 1992.

[134] V. Guritanu, P. Wissgott, T. Weig, H. Winkler, J. Sichelschmidt, M. Scheffler, A. Prokofiev, S. Kimura, T. Iizuka, A. M. Strydom, M. Dressel, F. Steglich, K. Held, and S. Paschen, "Anisotropic optical conductivity of the putative Kondo insulator $CeRu_4Sn_6$," *Phys. Rev. B*, vol. 87, p. 115129, Mar 2013.

[135] M. Sundermann, F. Strigari, T. Willers, H. Winkler, A. Prokofiev, J. M. Ablett, J.-P. Rueff, D. Schmitz, E. Weschke, M. M. Sala, A. Al-Zein, A. Tanaka, M. W. Haverkort, D. Kasinathan, L. H. Tjeng, S. Paschen, and A. Severing, "$CeRu_4Sn_6$: a strongly correlated material with nontrivial topology," *Scientific Reports*, vol. 5, p. 17937, December 2015.

[136] Y. Luo, F. Ronning, N. Wakeham, X. Lu, T. Park, Z.-A. Xu, and J. D. Thompson, "Pressure-tuned quantum criticality in the antiferromagnetic Kondo semimetal $CeNi_{2-\delta}As_2$," *Proceedings of the National Academy of Sciences*, vol. 112, no. 44, pp. 13520–13524, 2015.

[137] S. Dzsaber, L. Prochaska, A. Sidorenko, G. Eguchi, R. Svagera, M. Waas, A. Prokofiev, Q. Si, and S. Paschen, "Kondo insulator to semimetal transformation tuned by spin-orbit coupling," *Phys. Rev. Lett.*, vol. 118, p. 246601, Jun 2017.

[138] T. E. Mason, G. Aeppli, A. P. Ramirez, K. N. Clausen, C. Broholm, N. Stücheli, E. Bucher, and T. T. M. Palstra, "Spin gap and antiferromagnetic correlations in the kondo insulator cenisn," *Phys. Rev. Lett.*, vol. 69, pp. 490–493, Jul 1992.

[139] U. Stockert, P. Sun, N. Oeschler, F. Steglich, T. Takabatake, P. Coleman, and S. Paschen, "Giant isotropic Nernst effect in an anisotropic Kondo semimetal," *Phys. Rev. Lett.*, vol. 117, p. 216401, Nov 2016.

[140] X.-Y. Feng, H. Zhong, J. Dai, and Q. Si, "Dirac-Kondo semimetals and topological Kondo insulators in the dilute carrier limit," 2016.

[141] J. H. Pixley, S. B. Lee, B. Brandom, and S. A. Parameswaran, "Filling-enforced nonsymmorphic kondo semimetals in two dimensions," *Phys. Rev. B*, vol. 96, p. 081105(R), Aug 2017.

[142] M. Z. Hasan and C. L. Kane, "*Colloquium* : Topological insulators," *Rev. Mod. Phys.*, vol. 82, pp. 3045–3067, Nov 2010.

[143] X.-L. Qi and S.-C. Zhang, "Topological insulators and superconductors," *Rev. Mod. Phys.*, vol. 83, pp. 1057–1110, Oct 2011.

[144] J. E. Moore, "The birth of topological insulators," *Nature*, vol. 464, pp. 194–198, Mar 2010.

[145] B. A. Bernevig and T. L. Hughes, *Topological Insulators and Topological Superconductors*. Princeton University Press, 2013.

[146] S.-Y. Xu, I. Belopolski, N. Alidoust, M. Neupane, G. Bian, C. Zhang, R. Sankar, G. Chang, Z. Yuan, C.-C. Lee, S.-M. Huang, H. Zheng, J. Ma, D. S. Sanchez, B. Wang, A. Bansil, F. Chou, P. P. Shibayev, H. Lin, S. Jia, and M. Z. Hasan, "Discovery of a Weyl fermion semimetal and topological Fermi arcs," *Science*, vol. 349, no. 6248, pp. 613–617, 2015.

[147] B. Q. Lv, H. M. Weng, B. B. Fu, X. P. Wang, H. Miao, J. Ma, P. Richard, X. C. Huang, L. X. Zhao, G. F. Chen, Z. Fang, X. Dai, T. Qian, and H. Ding, "Experimental Discovery of Weyl Semimetal TaAs," *Phys. Rev. X*, vol. 5, p. 031013, Jul 2015.

[148] L. Lu, Z. Wang, D. Ye, L. Ran, L. Fu, J. D. Joannopoulos, and M. Soljačić, "Experimental observation of weyl points," *Science*, vol. 349, no. 6248, pp. 622–624, 2015.

[149] P. Hosur and X. Qi, "Recent developments in transport phenomena in Weyl semimetals," *Comptes Rendus Physique*, vol. 14, no. 9–10, pp. 857 – 870, 2013.

[150] X. Wan, A. M. Turner, A. Vishwanath, and S. Y. Savrasov, "Topological semimetal and Fermi-arc surface states in the electronic structure of pyrochlore iridates," *Phys. Rev. B*, vol. 83, p. 205101, May 2011.

[151] A. A. Burkov and L. Balents, "Weyl Semimetal in a Topological Insulator Multilayer," *Phys. Rev. Lett.*, vol. 107, p. 127205, Sep 2011.

[152] A. C. Hewson, *The Kondo Problem to Heavy Fermions:*. Cambridge: Cambridge University Press, 001 1993.

[153] C. Y. Guo, F. Wu, Z. Z. Wu, M. Smidman, C. Cao, A. Bostwick, C. Jozwiak, E. Rotenberg, Y. Liu, F. Steglich, and H. Q. Yuan, "Evidence for weyl fermions in a canonical heavy-fermion semimetal ybptbi," *Nature Communications*, vol. 9, no. 1, p. 4622, 2018.

[154] C. Guo, C. Cao, M. Smidman, F. Wu, Y. Zhang, F. Steglich, F.-C. Zhang, and H. Yuan, "Possible Weyl fermions in the magnetic Kondo system CeSb," *npj Quantum Materials*, vol. 2, p. 39, 2017.

[155] N. Alidoust, A. Alexandradinata, S.-Y. Xu, I. Belopolski, S. K. Kushwaha, M. Zeng, M. Neupane, G. Bian, C. Liu, D. S. Sanchez, P. P. Shibayev, H. Zheng, L. Fu, A. Bansil, H. Lin, R. J. Cava, and M. Z. Hasan, "A new form of (unexpected) Dirac fermions in the strongly-correlated cerium monopnictides," *arXiv:1604.08571*, 2016.

[156] P. Wissgott and K. Held, "Electronic structure of $CeRu_4Sn_6$: a density functional plus dynamical mean field theory study," *The European Physical Journal B*, vol. 89, no. 1, p. 5, 2016.

[157] Y. Xu, C. Yue, H. Weng, and X. Dai, "Heavy Weyl Fermion State in $CeRu_4Sn_6$," *Phys. Rev. X*, vol. 7, p. 011027, Mar 2017.

[158] S. Paschen, H. Winkler, T. Nezu, M. Kriegisch, G. Hilscher, J. Custers, A. Prokofiev, and A. Strydom, "Anisotropy of the Kondo insulator $CeRu_4Sn_6$," *Journal of Physics: Conference Series*, vol. 200, no. 1, p. 012156, 2010.

[159] H. Wei, S.-P. Chao, and V. Aji, "Long-range interaction induced phases in Weyl semimetals," *Phys. Rev. B*, vol. 89, p. 235109, Jun 2014.

[160] T. Morimoto and N. Nagaosa, "Weyl mott insulator," *Scientific Reports*, vol. 6, p. 19853, 2016.

[161] W. Witczak-Krempa, G. Chen, Y. B. Kim, and L. Balents, "Correlated quantum phenomena in the strong spin-orbit regime," *Annual Review of Condensed Matter Physics*, vol. 5, no. 1, pp. 57–82, 2014.

[162] S. Dzsaber, X. Yan, M. Taupin, G. Eguchi, A. Prokofiev, T. Shiroka, P. Blaha, O. Rubel, S. E. Grefe, H.-H. Lai, Q. Si, and S. Paschen, "Giant spontaneous Hall effect in a nonmagnetic Weyl-Kondo semimetal," 2018.

[163] J. Kruthoff, J. de Boer, J. van Wezel, C. L. Kane, and R.-J. Slager, "Topological classification of crystalline insulators through band structure combinatorics," *Phys. Rev. X*, vol. 7, p. 041069, Dec 2017.

[164] H. C. Po, A. Vishwanath, and H. Watanabe, "Symmetry-based indicators of band topology in the 230 space groups," *Nature communications*, vol. 8, no. 1, p. 50, 2017.

[165] E. M. Nica, R. Yu, and Q. Si, "Glide reflection symmetry, brillouin zone folding, and superconducting pairing for the $p4/nmm$ space group," *Phys. Rev. B*, vol. 92, p. 174520, Nov 2015.

[166] S. Murakami and S.-i. Kuga, "Universal phase diagrams for the quantum spin hall systems," *Phys. Rev. B*, vol. 78, p. 165313, Oct 2008.

[167] A. P. Schnyder, "Lecture notes on accidental and symmetry-enforced band crossings in topological semimetals." Topological Matter School, San Sebastian, Spain, August 2018.

[168] S. Murakami, "Phase transition between the quantum spin hall and insulator phases in 3d: emergence of a topological gapless phase," *New Journal of Physics*, vol. 9, no. 9, p. 356, 2007.

[169] A. A. Soluyanov, D. Gresch, Z. Wang, Q. Wu, M. Troyer, X. Dai, and B. A. Bernevig, "Type-ii weyl semimetals," *Nature*, vol. 527, pp. 495–498, 11 2015.

[170] S. Dzsaber, D. A. Zocco, A. McCollam, F. Weickert, R. McDonald, M. Taupin, X. Yan, A. Prokofiev, L. M. K. Tang, B. Vlaar, L. Stritzinger, M. Jaime, Q. Si, and S. Paschen, "Quenching a Weyl-Kondo semimetal by magnetic field," 2019.

[171] F. Strigari, *Hybridization and crystal-field effects in Kondo insulators studied by means of core-level spectroscopy.* PhD thesis, Universität zu Köln, 2015.

[172] C. Bareille, T.-S. Nam, T. Takabatake, K. Kuroda, T. Yajima, M. Nakayama, S. Kunisada, S. Akebi, M. Sakano, S. Sakuragi, R. Noguchi, B. I. Min, S. Shin, and T. Kondo, "Strongly anisotropic high-temperature fermi surface of the kondo semimetal cenisn revealed by angle-resolved photoemission spectroscopy," *Phys. Rev. B*, vol. 100, p. 045133, Jul 2019.

[173] Z. Fisk, P. C. Canfield, W. P. Beyermann, J. D. Thompson, M. F. Hundley, H. R. Ott, E. Felder, M. B. Maple, M. A. Lopez de la Torre, P. Visani, and C. L. Seaman, "Massive electron state in ybbipt," *Phys. Rev. Lett.*, vol. 67, pp. 3310–3313, Dec 1991.

[174] S. Chadov, X. Qi, J. Kübler, G. H. Fecher, C. Felser, and S. C. Zhang, "Tunable multifunctional topological insulators in ternary heusler compounds," *Nature Materials*, vol. 9, no. 7, pp. 541–545, 2010.

[175] L. M. Schoop, A. Topp, J. Lippmann, F. Orlandi, L. Müchler, M. G. Vergniory, Y. Sun, A. W. Rost, V. Duppel, M. Krivenkov, S. Sheoran, P. Manuel, A. Varykhalov, B. Yan, R. K. Kremer, C. R. Ast, and B. V. Lotsch, "Tunable weyl and dirac states in the nonsymmorphic compound cesbte," *Science Advances*, vol. 4, no. 2, p. eaar2317, 2018.

[176] L. M. Schoop, F. Pielnhofer, and B. V. Lotsch, "Chemical principles of topological semimetals," *Chemistry of Materials*, vol. 30, no. 10, pp. 3155–3176, 2018.

[177] A. Topp, M. G. Vergniory, M. Krivenkov, A. Varykhalov, F. Rodolakis, J. L. McChesney, B. V. Lotsch, C. R. Ast, and L. M. Schoop, "The effect of spin-orbit coupling on nonsymmorphic square-net compounds," *Journal of Physics and Chemistry of Solids*, vol. 128, pp. 296 – 300, 2019. Spin-Orbit Coupled Materials.

[178] S. E. Grefe, H.-H. Lai, S. Paschen, and Q. Si, "Weyl-Kondo semimetal: Towards control of Weyl nodes." arXiv:2002.07298, (to appear in JPS Conf. Proc.), Feb 2020.

[179] C. Cao, G.-X. Zhi, and J.-X. Zhu, "From trivial Kondo insulator $Ce_3Pt_3Bi_4$ to topological nodal-line semimetal $Ce_3Pd_3Bi_4$," 2019.

[180] L. Zhu, M. Garst, A. Rosch, and Q. Si, "Universally diverging grüneisen parameter and the magnetocaloric effect close to quantum critical points," *Phys. Rev. Lett.*, vol. 91, p. 066404, Aug 2003.

[181] J. Wu, L. Zhu, and Q. Si, "Entropy accumulation near quantum critical points: effects beyond hyperscaling," *Journal of Physics: Conference Series*, vol. 273, p. 012019, jan 2011.

[182] A. W. Rost, R. S. Perry, J.-F. Mercure, A. P. Mackenzie, and S. A. Grigera,

"Entropy landscape of phase formation associated with quantum criticality in $sr_3ru_2o_7$," *Science*, vol. 325, pp. 1360 – 1363, 2009.

[183] N. D. Mathur, F. M. Grosche, S. R. Julian, I. R. Walker, D. M. Freye, R. K. W. Haselwimmer, and G. G. Lonzarich, "Magnetically mediated superconductivity in heavy fermion compounds," *Nature*, vol. 394, pp. 39–43, 1998.

[184] F. Ronning, T. Helm, K. Shirer, M. Bachmann, L. Balicas, M. Chan, B. Ramshaw, R. McDonald, F. Balakirev, M. Jaime, *et al.*, "Electronic in-plane symmetry breaking at field-tuned quantum criticality in cerhin 5," *Nature*, vol. 548, no. 7667, p. 313, 2017.

[185] S. E. Grefe, H.-H. Lai, S. Paschen, and Q. Si, "Weyl–kondo semimetal: Towards control of weyl nodes," *JPS Conference Proceedings*, vol. 30, p. 011013, 2020.

[186] C. Fang, M. J. Gilbert, X. Dai, and B. A. Bernevig, "Multi-weyl topological semimetals stabilized by point group symmetry," *Phys. Rev. Lett.*, vol. 108, p. 266802, Jun 2012.

[187] B.-J. Yang and N. Nagaosa, "Classification of stable three-dimensional dirac semimetals with nontrivial topology," *Nature Communications*, vol. 5, no. 1, p. 4898, 2014.

[188] S.-K. Jian and H. Yao, "Correlated double-weyl semimetals with coulomb interactions: Possible applications to $hgcr_2se_4$ and $srsi_2$," *Phys. Rev. B*, vol. 92, p. 045121, Jul 2015.

[189] X. Li, B. Roy, and S. Das Sarma, "Weyl fermions with arbitrary monopoles in magnetic fields: Landau levels, longitudinal magnetotransport, and density-wave ordering," *Phys. Rev. B*, vol. 94, p. 195144, Nov 2016.

[190] S.-M. Huang, S.-Y. Xu, I. Belopolski, C.-C. Lee, G. Chang, T.-R. Chang, B. Wang, N. Alidoust, G. Bian, M. Neupane, D. Sanchez, H. Zheng, H.-T.

Jeng, A. Bansil, T. Neupert, H. Lin, and M. Z. Hasan, "New type of weyl semimetal with quadratic double weyl fermions," *Proceedings of the National Academy of Sciences*, vol. 113, no. 5, pp. 1180–1185, 2016.

[191] M. Ezawa, "Merging of momentum-space monopoles by controlling zeeman field: From cubic-dirac to triple-weyl fermion systems," *Phys. Rev. B*, vol. 96, p. 161202, Oct 2017.

[192] M. Ezawa, "Photoinduced topological phase transition from a crossing-line nodal semimetal to a multiple-weyl semimetal," *Phys. Rev. B*, vol. 96, p. 041205, Jul 2017.

[193] S. Ahn, E. J. Mele, and H. Min, "Optical conductivity of multi-weyl semimetals," *Phys. Rev. B*, vol. 95, p. 161112, Apr 2017.

[194] Z. Yan and Z. Wang, "Floquet multi-weyl points in crossing-nodal-line semimetals," *Phys. Rev. B*, vol. 96, p. 041206, Jul 2017.

[195] D. Zhang, H. Wang, J. Ruan, G. Yao, and H. Zhang, "Engineering topological phases in the luttinger semimetal α-sn," *Phys. Rev. B*, vol. 97, p. 195139, May 2018.

[196] P. Nikolić, "Two-dimensional heavy fermions on the strongly correlated boundaries of Kondo topological insulators," *Phys. Rev. B*, vol. 90, p. 235107, December 2014.

[197] S. Ok, M. Legner, T. Neupert, and A. M. Cook, "Magnetic Weyl and Dirac Kondo semimetal phases in heterostructures," 2017.

[198] M. Dzero, J. Xia, V. Galitski, and P. Coleman, "Topological Kondo Insulators," *Annual Review of Condensed Matter Physics*, vol. 7, no. 1, pp. 249–280, 2016.

[199] P.-Y. Chang, O. Erten, and P. Coleman, "Möbius kondo insulators," *Nature Physics*, vol. 13, no. 8, pp. 794–798, 2017.

[200] P.-Y. Chang and P. Coleman, "Parity-violating hybridization in heavy weyl semimetals," *Phys. Rev. B*, vol. 97, p. 155134, Apr 2018.

[201] V. Alexandrov, P. Coleman, and O. Erten, "Kondo breakdown in topological kondo insulators," *Phys. Rev. Lett.*, vol. 114, p. 177202, Apr 2015.

[202] P. Hlawenka, K. Siemensmeyer, E. Weschke, A. Varykhalov, J. Sánchez-Barriga, N. Y. Shitsevalova, A. V. Dukhnenko, V. B. Filipov, S. Gabáni, K. Flachbart, O. Rader, and E. D. L. Rienks, "Samarium hexaboride is a trivial surface conductor," *Nature Communications*, vol. 9, no. 1, p. 517, 2018.

[203] Y. Ohtsubo, Y. Yamashita, K. Hagiwara, S.-i. Ideta, K. Tanaka, R. Yukawa, K. Horiba, H. Kumigashira, K. Miyamoto, T. Okuda, W. Hirano, F. Iga, and S.-i. Kimura, "Non-trivial surface states of samarium hexaboride at the (111) surface," *Nature Communications*, vol. 10, no. 1, p. 2298, 2019.

[204] J. H. Pixley, R. Yu, and Q. Si, "Quantum phases of the shastry-sutherland kondo lattice: Implications for the global phase diagram of heavy-fermion metals," *Phys. Rev. Lett.*, vol. 113, p. 176402, Oct 2014.

[205] M. Oshikawa, "Topological approach to luttinger's theorem and the fermi surface of a kondo lattice," *Phys. Rev. Lett.*, vol. 84, pp. 3370–3373, Apr 2000.

[206] S. A. Parameswaran, "Topological 'luttinger' invariants for filling-enforced nonsymmorphic semimetals," *Journal of Physics: Condensed Matter*, vol. 31, p. 104001, jan 2019.

[207] S. Florens and A. Georges, "Slave-rotor mean-field theories of strongly correlated systems and the mott transition in finite dimensions," *Physical Review B*, vol. 70, no. 3, p. 035114, 2004.

[208] S. Florens and A. Georges, "Quantum impurity solvers using a slave rotor representation," *Physical Review B*, vol. 66, no. 16, p. 165111, 2002.

[209] K. Sun and E. Fradkin, "Time-reversal symmetry breaking and spontaneous anomalous hall effect in fermi fluids," *Physical Review B*, vol. 78, no. 24, p. 245122, 2008.

[210] G. E. Volovik, "Zeros in the fermion spectrum in superfluid systems as diabolical points," *JETP Lett.*, vol. 46, p. 98, 1987.

[211] A. A. Abrikosov, L. P. Gorkov, and I. E. Dzyaloshinski, *Methods of quantum field theory in statistical physics*. Dover Publications, Inc, 1975.

[212] W. H. Press, S. A. Teukolsky, W. T. Vetterling, and B. P. Flannery, *Numerical Recipes in Fortran 90 (2nd Ed.): The Art of Parallel Scientific Computing*. New York, NY, USA: Cambridge University Press, 1996.

[213] I. Belopolski, K. Manna, D. S. Sanchez, G. Chang, B. Ernst, J. Yin, S. S. Zhang, T. Cochran, N. Shumiya, H. Zheng, *et al.*, "Discovery of topological weyl fermion lines and drumhead surface states in a room temperature magnet," *Science*, vol. 365, no. 6459, pp. 1278–1281, 2019.